AN ABSTRACT OF THE THESIS OF

Bradford A. Cleary for the degree of Master of Science in Electrical and Computer Engineering

presented on November 10, 1998.

Title: Alternating-Current Thin-Film Electroluminescent Device Optical Excitation Experiments

Abstract approved: Redacted for Privacy

Thomas K. Plant

This thesis investigates two methods of optical excitation of alternating-current thin-film electroluminescent (ACTFEL) devices. The two experimental methods investigated in this thesis are the photo-induced charge (PIQ) and luminescence (PIL), and the subthreshold-voltage induced transferred charge (VIQ) techniques. PIQ/PIL experiments utilize an above-bandgap laser pulse to investigate the transport properties of photo-injected electrons and holes within the phosphor layer of the ACTFEL device. VIQ experiments use a broadband xenon lamp pulse to optically reset traps which are ionized by subthreshold bipolar voltage pulses. Both experiments characterize traps within the phosphor layer.

PIQ/PIL experiments are performed on evaporated ZnS:Mn ACTFEL devices possessing phosphor layers with thicknesses of 950, 700, and 300 nm. From the PIQ/PIL experiment, an impact excitation threshold electric field for evaporated ZnS:Mn is found to be ~1 MV/cm. Evidence of hole-trapping is also obtained from the PIQ experiment. The holes in evaporated ZnS:Mn ACTFEL devices are found to possess a drift length of ~180 ± 70 nm, a hole lifetime of ~2 ps, and a capture cross-section of ~7 x 10^{-13} cm^2. It is speculated that the trap responsible for hole capture is a zinc vacancy or zinc vacancy complex.

VIQ experiments are performed on evaporated, atomic layer epitaxy [ALE] (Cl), and ALE (DEZ) ZnS:Mn ACTFEL devices. Data obtained via VIQ experiments yield evidence for the generation of space charge below the EL conduction threshold, as well

as providing a means of estimating the physical location, energy depth, density, and capture cross-section of traps responsible for VIQ. The depth of the traps responsible for VIQ in evaporated, ALE (Cl), and ALE (DEZ) ZnS:Mn are estimated to be $\sim$1.1, $\sim$0.3, and $\sim$0.8 eV, respectively. It is speculated that the traps responsible for VIQ are due to sulfur vacancies, chlorine, and oxygen, for evaporated, ALE (Cl), and ALE (DEZ), respectively.

Alternating-Current Thin-Film Electroluminescent Device Optical Excitation Experiments

by

Bradford A. Cleary

A THESIS

submitted to

Oregon State University

in partial fulfillment of the

requirements for the degree of

Master of Science

Completed November 10, 1998

Commencement June 1999

Master of Science thesis of Bradford A. Cleary presented on November 10, 1998

APPROVED:

Redacted for Privacy

Major Professor, representing Electrical and Computer Engineering

Redacted for Privacy

Head of Department of Electrical and Computer Engineering

Redacted for Privacy

Dean of Graduate School

I understand that my thesis will become part of the permanent collection of Oregon State University libraries. My signature below authorizes release of my thesis to any reader upon request.

Redacted for Privacy

Bradford A. Cleary, Author

ACKNOWLEDGEMENTS

I would like to thank Dr. Thomas Plant and Dr. John Wager for their considerable help throughout the duration of my work on this thesis. Thanks to Paul Keir for his help, support and advice relating to the writing of this thesis. Thanks to John Hitt whose buoyant attitude always motivated me to do my best. Special thanks to my family and friends.

This work was supported by the U.S. Army Research Office under Contract No. DAAH04-94-G-0324 and by the Defense Advanced Research Projects Agency under the Phosphor Technology Center of Excellence, Grant No. MDA 972-93-1-0030.

TABLE OF CONTENTS

		Page
1	Introduction	1
2	Literature Review of ACTFEL Devices	3
2.1	Device Structure	3
2.2	Experimental Apparatus	5
2.3	Electrical Characterization Techniques	6
2.4	Photo-Induced Charge and Luminescence Measurements	10
2.5	Photo-Depolarization and Aging Experiments	13
3	Photo-Induced Charge and Luminescence Measurements	17
3.1	Introduction	17
3.2	Experimental Procedure	18
3.3	Experimental Results and Discussion	23
3.4	PIQ/PIL Conclusions	35
4	Subthreshold Voltage-Induced Transferred Charge	37
4.1	Introduction to VIQ	37
4.2	Experimental Procedure	39
4.3	Description a of VIQ Curve	41
4.4	Analysis of VIQ Curves	42
4.4.1	Polarity of VIQ Signal	42
4.4.2	Magnitude of VIQ Peak	47
4.4.3	VIQ Peak Voltage	48
4.4.4	The VIQ Threshold Voltage	48
4.5	Experimental Results	52
4.5.1	VIQ of Thermally Evaporated ZnS:Mn ACTFEL Devices	52

TABLE OF CONTENTS (Continued)

Page

4.5.2 Temperature Dependence of VIQ for Evaporated ZnS:Mn ACTFEL Devices 59
4.5.3 VIQ Summary for Evaporated ZnS:Mn ACTFEL Devices 62
4.5.4 VIQ aging of an Atomic Layer Epitaxy (Cl) ZnS:Mn ACTFEL Device 64
4.5.5 Temperature Dependence of VIQ for an ALE (Cl) ZnS:Mn ACTFEL Device 67
4.5.6 VIQ of an Atomic Later Epitaxy (DEZ) ZnS:Mn ACTFEL Device 68
4.5.7 Temperature Dependence of VIQ for an ALE (DEZ) ACTFEL Device 71

4.6 VIQ Summary 73

5 Conclusions and Recommendations for Future Work 78

5.1 Conclusions PIQ/PIL Experiments 78

5.2 Conclusions of VIQ Experiments 78

5.3 Recommendations for Future Work 79

BIBLIOGRAPHY 81

APPENDICES 85

Appendix A.1 Number of Subthreshold Pulses to Steady-State Operation 86
Appendix A.2 Time Response of VIQ 88
Appendix A.3 Spectral Response of VIQ 89
Appendix A.4 VIQ Illuminated from Opposite Interface 90
Appendix A.5 VIQ Measurements using a Buffer Amplifier 91

LIST OF FIGURES

Figure		Page
2.1.	ACTFEL device structure.	4
2.2.	Standard ACTFEL driving waveform.	4
2.3.	Standard ACTFEL experimental apparatus.	5
2.4.	Three capacitor model of an ACTFEL device.	6
2.5.	Example Q-V plots.	7
2.6.	Example C-V plot.	8
2.7.	Example Q-F_p plot.	9
3.1.	Energy bands for a negatively biased PIQ/PIL experiment.	19
3.2.	Energy bands for a positively biased PIQ/PIL experiment.	19
3.3.	Experimental apparatus for PIQ/PIL experiments.	20
3.4.	PIQ/PIL timing diagram. Dashed lines denote data acquired in the absence of the laser pulse.	22
3.5.	PIL of a 950 nm phosphor thickness evaporated ZnS:Mn ACTFEL device.	24
3.6.	PIL of a 700 nm phosphor thickness evaporated ZnS:Mn ACTFEL device.	24
3.7.	PIL of a 300 nm phosphor thickness evaporated ZnS:Mn ACTFEL device.	25
3.8.	PIQ of a 950 nm phosphor thickness evaporated ZnS:Mn ACTFEL device.	26
3.9.	PIQ of a 700 nm phosphor thickness evaporated ZnS:Mn ACTFEL device.	27
3.10.	PIQ of a 300 nm phosphor thickness evaporated ZnS:Mn ACTFEL device.	27
3.11.	Apparent hole PIQ due to electron back injection.	29
3.12.	Lower laser intensity PIQ measurement of a 950 nm ZnS:Mn ACTFEL device.	30

LIST OF FIGURES (Continued)

Figure		Page
3.13.	Lower laser intensity PIQ measurement of a 700 nm ZnS:Mn ACTFEL device.	30
3.14.	Lower laser intensity PIQ measurement of a 300 nm ZnS:Mn ACTFEL device.	31
3.15.	Hole drift length, as estimated by the PIQ hole to electron ratio, as a function of applied phosphor field for three different evaporated ZnS:Mn ACTFEL devices.	32
3.16.	Quantum efficiency of a 950 nm ZnS:Mn ACTFEL device.	34
3.17.	Quantum efficiency of a 700 nm ZnS:Mn ACTFEL device.	34
3.18.	Quantum efficiency of a 300 nm ZnS:Mn ACTFEL device.	35
4.1.	Experimental apparatus for VIQ measurements.	38
4.2.	Timing diagram for a VIQ experiment.	38
4.3.	Example of a VIQ curve.	40
4.4.	VIQ energy band diagram showing negative charge trapped at or near the bottom (ITO) phosphor/insulator interface. For this case, transport of photo-injected electrons generated near the bottom (ITO) interface gives rise to a positive polarity VIQ signal, as sensed from a capacitor connected to the ITO side of the ACTFEL device.	43
4.5.	VIQ energy band diagram showing positive charge trapped at or near the bottom (ITO) phosphor/insulator interface. In this case, transport of photo-injected holes generated near the bottom (ITO) interface gives rise to a negative polarity VIQ signal, as sensed from a capacitor connected to the ITO side of the ACTFEL device.	43

LIST OF FIGURES (Continued)

Figure — Page

4.6. VIQ energy band diagram showing positive bulk space charge. (a) Initially, transport of photo-injected electrons generated near the bottom (ITO) interface gives rise to a positive polarity VIQ signal, as sensed on a capacitor connected to the ITO side of the ACTFEL device. These photo-injected electrons also recombine with ionized traps, yielding the energy band picture shown in (b). (b) After some positive bulk space charge has been annihilated by the initial photo-injected electrons, transport of photo-injected holes gives rise to a negative polarity VIQ signal. 44

4.7. VIQ energy band diagram showing negative bulk space charge. (a) Initially, transport of photo-injected holes generated near the bottom (ITO) interface gives rise to a negative polarity VIQ signal, as sensed on a capacitor connected to the ITO side of the ACTFEL device. These photo-injected holes also recombine with ionized traps, yielding the energy band picture shown in (b). (b) After some negative bulk space charge has been annihilated by the initial photo-injected holes, transport of photo-injected electrons gives rise to a positive polarity VIQ signal. 45

4.8. VIQ aging trend of an evaporated ZnS:Mn ACTFEL device. The five curves shown correspond to 0.5, 6, 30, 50, and 73 hours of aging at 1 kHz. 53

4.9. Positive polarity C-V curves of an evaporated ZnS:Mn ACTFEL device after 0.5, 30 and 73 hours aging at 1 kHz. 54

4.10. Negative polarity C-V curves of an evaporated ZnS:Mn ACTFEL device after 0.5, 30 and 73 hours aging at 1 kHz. 54

4.11. Positive polarity C-V curves of an evaporated ZnS:Mn ACTFEL device acquired after 210 hours aging at 3 kHz. Curves acquired at 20, 40, and 60 V over threshold. Arrow indicates increasing voltage. 55

4.12. Negative polarity C-V curves of an evaporated ZnS:Mn ACTFEL device acquired after 210 hours aging at 3 kHz. Curves acquired at 20, 40, and 60 V over threshold. Arrow indicates increasing voltage. 55

LIST OF FIGURES (Continued)

Figure		Page
4.13.	An idealized VIQ transient curve illustrating a tail which may change as a function of aging and yet not affect the measured VIQ signal magnitude. v_{cs} is the voltage measured across a sense capacitor in series with the ACTFEL device.	59
4.14.	Temperature dependent VIQ curves for an evaporated ZnS:Mn ACTFEL Device. Curves are acquired at 20, 200, 300, 373, and 423 K. The arrow indicates increasing temperature.	60
4.15.	Summary of evaporated ZnS:Mn aging trends. The dashed circles indicate the interface where aging is believed to occur.	63
4.16.	VIQ aging trend for an ALE (Cl) ZnS:Mn ACTFEL device. Aging is for 0, 4, and 87 hours aging at 3 kHz, with arrows indicating increasing aging time.	65
4.17.	Positive polarity C-V curves for an ALE (Cl) ZnS:Mn ACTFEL device at 0, 4, and 87 hours of aging at 3 kHz, with arrows indicating increasing aging time.	65
4.18.	Negative polarity C-V curves of ALE (Cl) ZnS:Mn ACTFEL device at 0, 4, and 87 hours of aging at 3 kHz, with arrows indicating increasing aging time.	66
4.19.	Temperature dependent VIQ curves for an ALE (Cl) ZnS:Mn ACTFEL device. Curves are acquired at 20, 150, 300, and 450 K. The arrows indicate increasing temperature. The asterisks indicate the voltage onset of the pre-threshold glow.	67
4.20.	VIQ aging trend for an ALE (DEZ) ZnS:Mn ACTFEL device. Aging is for 0, 0.6, and 40 hours at 3 kHz, with arrows indicating increasing aging time.	69
4.21.	Positive polarity C-V curves for an ALE (DEZ) ZnS:Mn ACTFEL device at 0, 0.6, and 40 hours of aging at 3 kHz, with arrows indicating increasing aging time.	70
4.22.	Negative polarity C-V curves for an ALE (DEZ) ZnS:Mn ACTFEL device at 0, 0.6, and 40 hours of aging at 3 kHz, with arrows indicating increasing aging time.	70

LIST OF FIGURES (Continued)

Figure — Page

4.23. Temperature dependent VIQ curves for an ALE (DEZ) ZnS:Mn ACTFEL device. Curves are acquired at 173, 300, 375, and 450 K. The arrow indicates increasing temperature. The asterisks indicate the voltage onset of the pre-threshold glow. 72

4.24. Estimated energy depths of possible traps responsible for the VIQ signal. Ionization energies of Zn vacancies [1], ionization energies of sulfur vacancies [2], ionization energy of chlorine [3, 4, 5], ionization energy of oxygen [3]. 75

LIST OF TABLES

Table		Page
1.	Capture cross-section/trap depth combinations which yield threshold emission rate.	58
2.	Temperature dependence of the VIQ threshold field and corresponding simulated trap depth assuming a capture cross-section of 10^{-14} cm^2.	61
3.	Simulated capture cross-section/trap depth pairs. The mean and standard deviation shown for trap depths are obtained by performing simulations at different temperatures.	62
4.	Simulated capture cross-section/trap depth pairs for an ALE (DEZ) ACTFEL Device.	73
5.	Summary of VIQ aging trends for evaporated, ALE (Cl), and ALE (DEZ) ZnS:Mn ACTFEL devices.	74
6.	Ionic radii of Zn, S and possible extrinsic defect candidates giving rise to the VIQ signal. All ionic radii are from Shannon [6], with the exception of C^{-4} which is from Lange [7].	75

Alternating-Current Thin-Film Electroluminescent Device Optical Excitation Experiments

Chapter 1
Introduction

The thin-film electroluminescent device is a promising candidate in the current search for a new type of electronic display. Currently, most electronic displays are either liquid-crystal-displays (LCDs) for smaller applications, or cathode-ray-tubes (CRTs) for larger applications. The need for a more durable, lighter weight, greater viewing angle display has led to the development of flat-panel displays as a possible alternative. The devices investigated in this thesis fall into the category of alternating-current thin-film electroluminescent (ACTFEL) devices. They offer many benefits including light weight, high brightness, wide viewing angle, and the ability to make very small devices used for heads-up displays. These combined factors make ACTFEL devices a flat panel display industrial contender.

ACTFEL devices, as the name suggests, are driven using an alternating current (AC) voltage source. Light is produced in the device by excitation of luminescent impurities by electrons which are accelerated by the applied field. The luminescent impurities are intentionally added to the phosphor. By changing the type of luminescent impurity, the wavelength of light emitted from the device can be changed. Until recently, the lack of an efficient blue phosphor has precluded commercial development of a viable full-color ACTFEL flat panel display.

The purpose of this thesis is to investigate the operation and device physics of ACTFEL devices by means of two optical excitation measurement techniques. The first is an experiment in which ACTFEL devices are excited with an ultra-violet (UV) laser pulse during device operation. UV photons absorbed in the phosphor generate electron-hole pairs which are subject to the external applied voltage. The transport of photo-injected carriers is measured by acquiring the voltage induced on a sense capacitor in series with the device. The photo-induced charge (PIQ) and

the photo-induced luminescence (PIL) which is the light generated by the photo-injected carriers, are measured as a function of the maximum applied voltage. This measurement allows observation of the transport of electrons and holes separately. In addition, PIQ and PIL measurements facilitate decoupling of carrier transport from carrier injection.

The second experiment, subthreshold voltage-induced transferred charge (VIQ), consists of driving the ACTFEL device with a bipolar trapezoidal electrical pulse until the ACTFEL device reaches steady-state and then illuminating the device with broadband radiation from a xenon lamp. The maximum charge induced on a sense capacitor in series with the device during the optical portion of the experiment is related to the maximum applied voltage during the electrical portion of the experiment. VIQ curves demonstrate that ionization of traps, giving rise to space charge within the phosphor, occurs well below the conduction threshold. Different deposition methods yield very different VIQ aging trends due to the quality of the interfaces and possibly the bulk of the crystal. These trends are discussed separately for evaporated, atomic layer epitaxy [ALE] (Cl), and ALE (DEZ) ZnS:Mn ACTFEL devices.

Chapter 2 is an overview of ACTFEL device operation and standard electrical measurements as well as a review of literature relevant to the subject of optical excitation of ACTFEL devices. Chapters 3 and 4 are detailed accounts of the two different experiments, PIQ/PIL and VIQ. Each of these chapters includes: an introduction, experimental apparatus, experimental procedure, theoretical basis and expected results, experimental results, and conclusions. Conclusions and recommendations for future work are offered in Chapter 5.

Chapter 2
Literature Review of ACTFEL Devices

Basic device structure and operation are presented in this chapter, as well as a review of literature pertinent to the investigation of optical excitation experiments of ACTFEL devices. Specifically, the work of Corlatan et al., and work from the Heinrich-Hertz Institute (HHI) are reviewed as the basis of the PIQ/PIL work performed for this thesis. Also, the research of Vlasenko et al., on photo-depolarization (PDP) is discussed since their experimental results are quite similar to those presented in this thesis via the VIQ method, as discussed in Chapter 4.

2.1 Device Structure

The structure of a standard ACTFEL device, as shown in Fig. 2.1, is a sandwich of phosphor between two insulating layers, with contacts on either side. The device is normally grown on a glass substrate. The first layer to be deposited is a transparent conductor, indium tin oxide (ITO). Next, a transparent insulator, aluminum titanium oxide (ATO) or barium tantalum oxide (BTO) is deposited onto the stack. The phosphor is then deposited by sputtering, thermal evaporation, or atomic-layer epitaxy (ALE), followed by another insulator, which is then topped off by an aluminum contact.

For experimental purposes, it is most convenient to drive ACTFEL devices with a bipolar trapezoidal waveform. The standard waveform has 5 μs rise and fall times and a 30 μs plateau, at a frequency of 1 kHz, as shown in Fig. 2.2. The letters on the diagram serve as convenient points of reference when investigating the standard electrical measurments. This trapezoidal pulse is employed rather than a sine wave or triangle wave because of the constant applied voltage during the plateau of the pulse. A constant applied voltage has many advantages, as discussed below.

Top Electrode	Al (2000 Å)
Top Insulator	SiON (1100 Å)
Phosphor	ZnS:Mn (3000, 7000, 9500Å)
Bottom Insulator	SiON (1800 Å)
Bottom Electrode	ITO (3000 Å)
Glass Substrate	Corning 7059 Glass (1.1mm)

Figure 2.1. ACTFEL device structure.

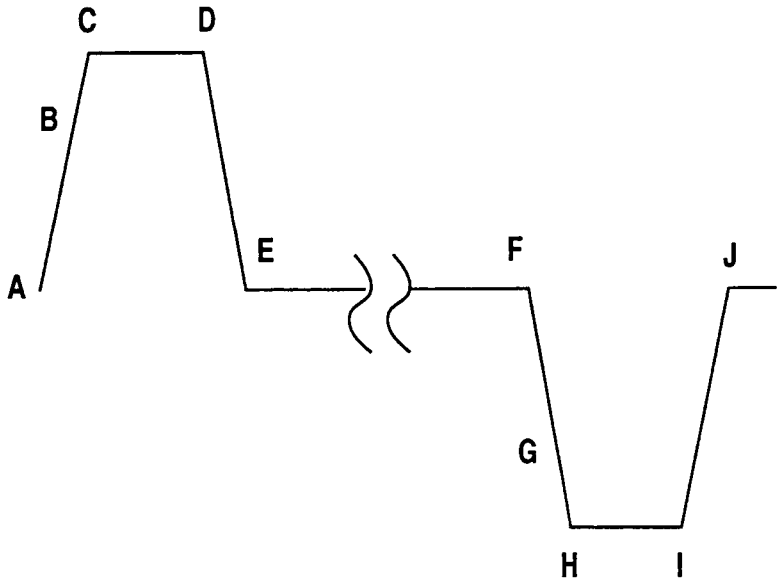

Figure 2.2. Standard ACTFEL driving waveform.

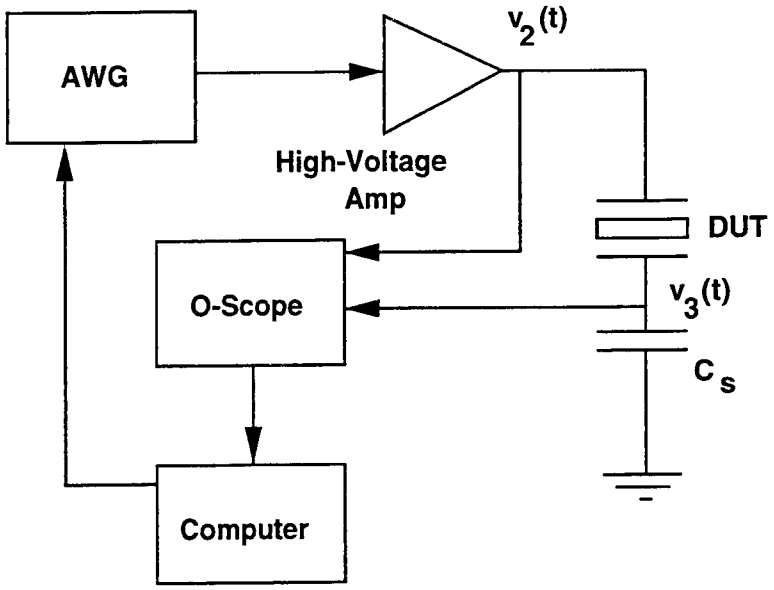

Figure 2.3. Standard ACTFEL experimental apparatus.

2.2 Experimental Apparatus

The standard experimental apparatus employed for ACTFEL characterization consists of an arbitrary waveform generator (Wavetek model 395), a digital oscilloscope (Tektronix model TDS420), a computer (PC 486-66), a 100 nF sense capacitor, and a high voltage amplifier, as shown in Fig. 2.3. The optical measurements necessitate the use of additional equipment, but for standard electrical characterization, this is all that is required. The arbitrary waveform generator is programmed by the computer to output the bipolar waveform. The waveform is then amplified by a custom high voltage amplifier which is used to drive the sample. The sample is connected in series with a sense capacitor to ground. Standard electrical measurements are achieved by measuring the charge on the sense capacitor as a function of the applied voltage. GPIB interfacing of the equipment allows all experiments to be automated, and data acquired by the digital oscilloscope is stored in the computer.

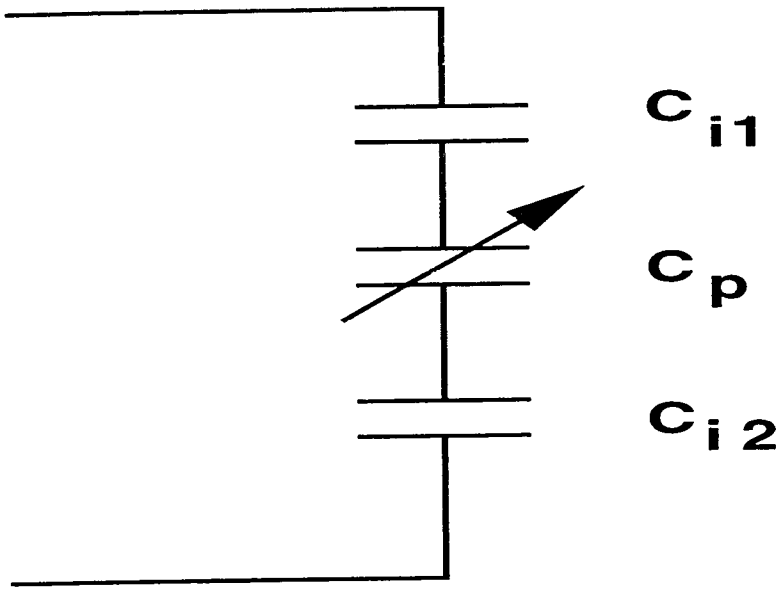

Figure 2.4. Three capacitor model of an ACTFEL device.

2.3 Electrical Characterization Techniques

The standard electrical measurements to be discussed are the capacitance-voltage (C-V), the charge-voltage (Q-V), the internal charge - phosphor field (Q-F_p), and the maximum charge - maximum applied voltage (Q_{max}-V_{max}), also known as the transferred charge measurement.

The charge-voltage (Q-V) experiment is a measurement of the charge measured externally across the sense capacitor as a function of the external voltage applied to the device. The standard ACTFEL device can be most simply modeled as three capacitors in series, as shown in Fig. 2.4, where C_{i1} and C_{i2} refer to the capacitances of the two insulating layers and C_p represents the capacitance of the phosphor layer. The insulators and the phosphor are all modeled as capacitors, with the phosphor modeled as a variable capacitor. As the phosphor breaks down and conduction is achieved, the phosphor capacitance goes to infinity since conduction essentially shunts the phosphor capacitance out of the circuit. Since capacitors in series add reciprocally, the capacitance of the ACTFEL device is expected to increase as conduction occurs. Since capacitance is equal to the partial derivative of the charge with

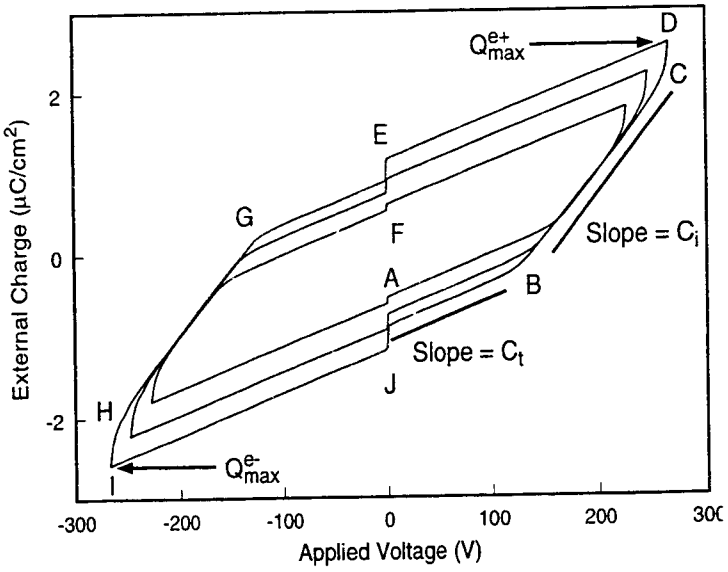

Figure 2.5. Example Q-V plots.

respect to the voltage, the slope of the Q-V curve is the capacitance of the device. A typical Q-V curve shows two distinct regions corresponding to operation below and above the onset of conduction, as shown in Fig. 2.5.

Below the onset of conduction a smaller slope is observed; this corresponds to the reciprocal sum of the phosphor capacitance and the insulator capacitances. A discontinuity in the slope is observed at the turn-on voltage. Above the turn-on voltage, the Q-V slope corresponds to only the reciprocal sum of the two insulators. The best method for determining the total and insulator capacitance (assuming the device is well behaved) is to calculate the slopes of the Q-V plot above and below turn-on, respectively. The slope of the Q-V curve is the C-V curve, discussed below. In all electrical characterization, the ACTFEL device is in series with a sense capacitor; thus, the device under test has the same charge across it as the sense capacitor.

A Q-V curve is traversed in a counter-clockwise sense, starting at point A on the driving waveform. Below turn-on, the Q-V curve is just a line at some angle with respect to the coordinate axis; in this regime, no conduction charge is observed. Normally, Q-V measurements are taken at 20, 40, and 60 V above threshold. Assuming the device contains no space charge (i.e. has either never been operated before, or

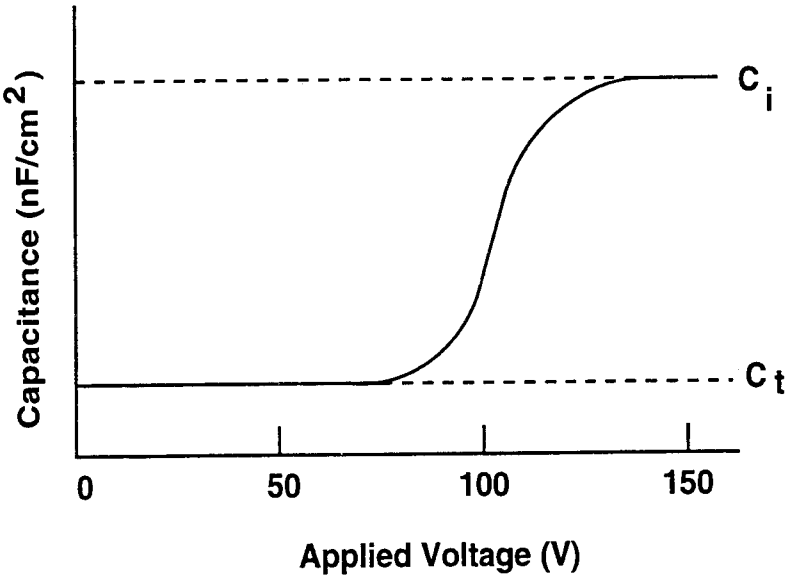

Figure 2.6. Example C-V plot.

has just been optically reset) the charge on the sense capacitor will increase with increasing voltage from point A to point B. From point B to point C on the Q-V curve, the voltage across the device is still increasing and the slope of the Q-V curve is constant. Between C and D, the voltage is constant and a slight increase in the slope is observed, as explained below. From D to E, the voltage decreases and a corresponding decrease in the charge is observed. From E to F, the voltage is zero and the change in charge is referred to as "leakage charge". Points F-J correspond to the negative pulse, with the same regions of operation, only in the opposite sense.

The capacitance-voltage (C-V) measurement is accomplished by acquiring the voltage applied to the ACTFEL device and the voltage induced across the sense capacitor as a function of time. The derivatives of both the applied voltage and the charge induced on the sense capacitor are obtained and used to calculate the capacitance of the device as a function of the applied voltage. Since $i = dq(t)/dt$ and $C = dq(t)/dv(t)$, by taking $dv_{el}(t)/dt$ (the derivative of the voltage dropped across the ACTFEL device with respect to time), $dq(t)/dt$ can be divided by $dv_{el}(t)/dt$ to obtain dq/dv_{el}, the capacitance. An example capacitance-voltage curve is shown in Fig. 2.6.

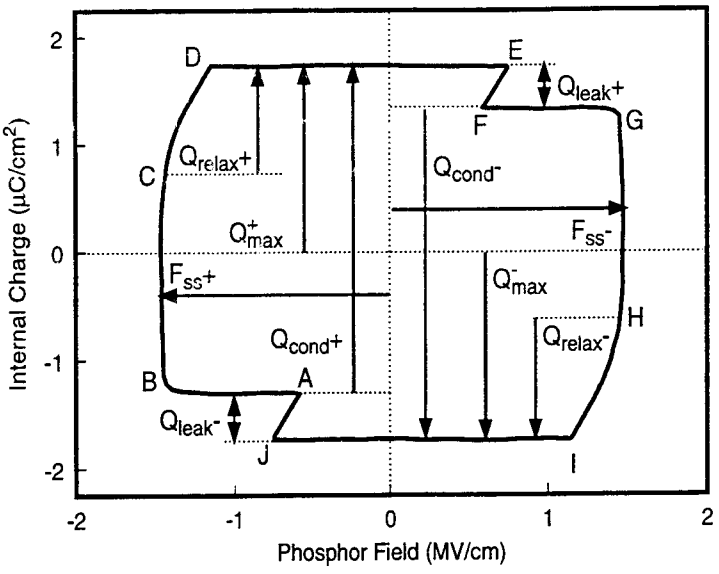

Figure 2.7. Example Q-F_p plot.

The internal charge - phosphor field (Q-F_p) curve is traversed in a clockwise direction, once again starting at point A on the driving waveform. The phosphor field is calculated from

$$f_p(t) = \frac{1}{d_p}\left(\frac{C_s v_3(t)}{C_i} - [v_2(t) - v_3(t)]\right) \tag{2.1}$$

where d_p is the phosphor thickness of the device. This equation allows the phosphor field to be calculated if accurate values for the capacitances and the thickness are known. A typical Q-F_p curve, as shown in Fig. 2.7 is calculated using the insulator capacitance found from the slope of the Q-V curve above turn-on. Point A on the Q-F_p curve is offset from zero by the polarization charge which remains from the previous opposite polarity pulse.

From point A to B the internal field increases, until at point B, ideally, the internal field reaches a value which remains constant until point C. If the B to C phosphor field is constant for applied voltages of 20, 40 and 60 V over threshold the device is said to exhibit "field-clamping". The internal phosphor field is a constant from B to C and the excess external applied voltage is dropped across the insulators. From point C to D, the charge continues to increase, but the field decreases slightly;

this is referred to as "field relaxation". Then from D to E, the falling edge of the electrical pulse, the field decreases linearly with no change in internal charge. From E to F leakage charge is observed. Once again, points F through J correspond to the negative pulse.

Other values of interest, which are labeled in Fig. 2.7, are the conduction charge (Q_{cond}), the polarization charge (shown as Q_{max} in Fig. 2.7), and the relaxation charge (Q_{relax}). The conduction charge is the total charge transferred across the device during one pulse. The polarization charge is the charge which remains from the last opposite polarity pulse. The beginning of the positive pulse is aided by the positive charge remaining from the last negative pulse. The mechanism for relaxation charge is not clear at this time [8], but the effect results in a decrease in the internal field of the phosphor.

The final standard electrical measurement to be discussed is the maximum transferred charge versus maximum applied voltage (Q_{max} - V_{max}), or transferred charge measurement. For this experiment, the maximum charge on the sense capacitor, which occurs at point D, is measured as a function of the maximum applied voltage. A single Q_{max} data point is the result of averaging a number of electrical pulses at the same V_{max}. Following acquisition of a specific Q_{max} at a given V_{max}, the voltage is ramped up to a new V_{max}, the device is allowed to reach steady-state, and the next Q_{max} data point is acquired. Of particular interest is the region where the device first turns on; this is referred to as the threshold voltage. At this point the slope of the Q_{max} - V_{max} curve has a discontinuity resulting from the onset of charge transfer.

2.4 Photo-Induced Charge and Luminescence Measurements

The photo-induced charge (PIQ) and photo-induced luminescence (PIL) measurement techniques were originally developed by Corlatan et al. who analyzed evaporated ZnS:Mn ACTFEL devices with probe layers in which only certain regions of the phosphor were Sm-doped. [9, 10] Initial work on PIQ/PIL was performed by

Corlatan et al. in Belgium, as well as at the Heinrich-Hertz Institute (HHI) in Berlin. To perform PIQ/PIL experiments, a laser is incident on the ACTFEL device while an external voltage is applied to the device. The theoretical basis of PIQ/PIL measurements is that electron-hole pairs are generated within ~40-60 nm [9] of the nearest phosphor surface by an ultraviolet laser pulse. When the aluminum contact (the near-surface electrode) is negatively biased, photo-induced electrons are transported across the phosphor, while holes remain close to the phosphor/insulator interface at which they are created.

The PIQ signal is the charge induced on a sense capacitor in series with the device as a result of the photo-injected carriers. The PIL signal is the measured luminescence that arises from excitation of luminescent impurities as the photo-induced electrons transit the phosphor. When the aluminum contact is positively biased, photo-induced holes traverse the phosphor, giving rise to PIQ and PIL, and electrons remain close to the phosphor/insulator interface at which they are created.

One of the advantages of PIQ/PIL experiments is that electron and hole transport may be studied independently by simply changing the polarity of the DC bias. The short absorbtion length of the phosphor in the UV portion of the electromagnetic spectrum allows the electron and hole transport to be decoupled. If UV light is evenly absorbed across the phosphor, then this experiment could not differentiate hole transport from electron transport. Also, PIQ/PIL experiments allow the study of transport independent of carrier injection; the carriers injected by the UV laser pulse are not emitted from interface states, as in standard electroluminescent device operation, but are generated within the bulk of the semiconductor by band-to-band absorbtion of UV photons.

The PIQ/PIL experiments performed by Corlatan et al. differ from the experiments described in this thesis in a few important ways. Their samples possess probe layers of phosphor selectively doped with luminescent impurities, while the samples tested in this thesis are uniformly doped. Their experiments provide information about the fields within the phosphor at different distances from the interface. By fabricating samples with a doped probe layer, they could establish where the photo-

induced luminance originates. If the electric field is large enough within the doped probe layer for electrons (or holes) to gain enough kinetic energy to impact excite luminescent centers, then light is produced. Conversely, if the field in the probe region is below that needed for impact excitation, then no light is produced. The average phosphor field may be estimated based on the applied voltage, but due to band-bending from space charge, the local fields are not known. If a uniformly distributed space charge is assumed, then a cathode field can be calculated. However, determination of the internal field as a function of distance is difficult.

The use of probe layers excited by UV laser photo-generated carriers is an excellent means of determining internal fields. When the photo-generated carriers transit the phosphor, the only region in which the carriers can create light is the doped region; thus, if photo-induced light is observed, the field in the doped region must be higher than the excitation threshold for luminescent centers.

Another difference between the work performed in this thesis and the work of Corlatan et al. is that they do not perform a difference curve analysis of their data by subtracting a data set in which the laser is not applied, as shown in Fig. 3.4. Therefore, their PIQ/PIL data includes the effects of normal electroluminescence, while the method employed in this thesis attempts to isolate the response to that of only photo-injected carriers.

Corlatan et al. concluded that in ZnS:Mn ACTFEL devices hole transport may give rise to impact excitation-induced electroluminescence, holes are approximately half as efficient as electrons in contributing to the transferred charge, and that the efficiency of hole transport (where efficiency is defined as PIL divided by PIQ) is significantly greater for holes than electrons. Their conclusion that the photo-induced hole efficiency is greater than the photo-induced electron efficiency was very surprising to them. They interpreted this result as arising from differences in the electric field profile in the phosphor for the cases of hole and electron transport.

In contrast, the PIQ/PIL measurement performed by the HHI group [11, 12, 13, 14, 15] differ significantly from that of Corlatan et al. and from that reported in this thesis in that no optical reset pulse is used and the devices are driven continuously

with an electrical pulse. In the HHI method, each set of data is obtained by driving the device electrically with 100 pulses at a given voltage, followed by a measuring pulse which is applied at the same time as the laser pulse. This allows the device to reach steady-state before application of the laser pulse. However, the steady-state condition is different for each voltage, whereas an optical reset pulse allows one to start from the same initial condition before each measuring pulse.

HHI experiments are performed using SrS:Ce ACTFEL devices, as opposed to the experiments presented in this thesis and the work of Corlatan et al., which focus on ZnS:Mn ACTFEL devices. PIQ/PIL measurements performed by HHI using multi-source deposited SrS:Ce ACTFEL devices show no evidence of hole transport. [11, 12, 13, 14, 15] Thus, carrier transport in SrS:Ce ACTFEL devices is dominated by electrons. PIQ/PIL trends point to the important role of dynamic space charge in determining the behavior of SrS:Ce devices. Furthermore, PIQ/PIL measurements provide evidence for electron multiplication in SrS at fields significantly below that of the normal ACTFEL threshold, which is attributed to defect ionization.

2.5 Photo-Depolarization and Aging Experiments

Results of photo-depolarization (PDP) experiments performed by Vlasenko et al. are similar to results in this thesis research obtained by the VIQ technique. [16] The PDP experiments are performed by applying a below-threshold DC voltage to the device and then stimulating the ACTFEL device with a variable wavelength light source. As the device is illuminated, an excitation wavelength-dependent photo-current is measured. The polarity of the applied DC voltage is then reversed and the device is photo-depolarized (i.e. optically reset) once again. The ACTFEL device is not electrically excited during PDP measurements. Following measurement of PDP for both polarities, the device is aged for a period of 10 hours with a 5 kHz sine wave with a tranferred charge of 1 $\mu C/cm^2$. PDP experiments are then performed on the aged sample and this data is then used to determine the aging properties of the phosphor as well as the interfaces.

The most pertinent result of the PDP experiment is the possibility of negative space charge being present in the ZnS:Mn phosphor layer. The traditional understanding of the physics of ZnS:Mn ACTFEL devices has given rise to the supposition that only positive space charge occurs in these devices. The measured PDP curves of ALE deposited ZnS:Mn ACTFEL devices are asymmetrical with respect to the polarity of the charging voltage, which is attributed to electron traps of energy depth $\sim$1.2 eV, which give rise to negative space charge.

Kononets et al. perform PDP experiments on ALE ZnS:Mn ACTFEL devices deposited with two different precursor gases, one containing chlorine, the other containing diethyl zinc (DEZ), an organic compound. [17] The PDP aging trends give very different results for the two different precursor gases. The data suggest that the energy bands are bent differently for each interface. It is thought that the aging process in Cl-deposited ZnS:Mn ACTFEL devices is due to migration of Cl resulting in a shallower source of free electrons; i.e. the Cl atoms diffuse and sit on S sites, becoming shallow donors following aging.

In contrast, the PDP polarity reverses after aging of ALE (DEZ) ACTFEL devices, presumably because the interfaces are depleted of electrons. This effect is observed after only minutes of operation, and is attributed to a thin interlayer with a lower work function which is generated near the interfaces. Electrical, optical (brightness-voltage (B-V)), and PDP aging trends show that the chlorine-deposited phosphor degrades much faster and more dramatically than the DEZ-deposited film.

Vlasenko et al. also perform PDP experiments on evaporated ZnS:Mn ACTFEL devices. [16] PDP spectra are acquired after the ACTFEL devices are aged for 3 h and then again after 10 h using a 5 kHz sine wave. The results of this study show a decrease in the concentration of both acceptor and donor-like traps within the phosphor. The decrease in concentration is attributed to gettering of the defects to grain boundaries during drift. This results in a decrease of the Fermi level within the phosphor.

Vlasenko et al. find evidence from PDP that Cl_s^+ in ALE (Cl) ZnS:Mn ACTFEL devices exists at an energy depth of $\sim$0.3 eV. Vlasenko et al. also find evidence that

oxygen in ALE (DEZ) ZnS:Mn ACTFEL devices exists at an energy depth of ~0.9-1.2 eV. The findings of the VIQ experiment, as well as electrical characterization performed concomitant with the VIQ experiments, support the findings of Vlasenko et al., as discussed in Chapter 4.

Previous work on the aging trends of ZnS:Mn ACTFEL devices is now investigated. The aging trends of ZnS:Mn ACTFEL devices have been studied by several groups. Bossche et al. find that aging with asymmetrical waveforms provides evidence for migration of traps as a possible mechanism for aging of evaporated and ALE ACTFEL devices. [18] Their method shows that shallow donor states generated during aging may be made to migrate by applying a DC field to the ACTFEL device. It is postulated that these traps move from the insulator into the bulk of the ZnS layer.

Soenen et al. investigate the aging behavior of ALE ZnS ACTFEL devices with different precursor gases. [19] Precursors containing Cl and precursors which do not contain Cl are used in the deposition of undoped ZnS. Conclusions drawn from their experiments suggest that Cl is not responsible for the softening characteristics observed in the electrical (C-V) and optical (B-V) aging trends of the ACTFEL devices studied. Also, evidence is found which suggests that donors are initally created near the first grown (bottom ITO)) interface, with subsequent aging generating donors near the last grown (top (Al)) interface.

The main studies which are pertinent to this thesis involve observing changes in C-V curves with aging. C-V curves can shift either positively or negatively (p-shift or n-shift) depending on the deposition method. If the above-turn-on C-V curve deviates from the ideal, i.e. C does not equal C_i (the physical insulator capacitance), two situations are possible. First, the measured capacitance is less than C_i due to inadequate sourcing of carriers. Second, the measured capacitance is greater than C_i due to space charge in the phosphor. [20] The existence of overshoot in a C-V curve is also thought to be evidence of space charge in the phosphor. Softening of the turn-on portion of a C-V curve is indicative of electrons being injected from bulk trap states. [20]

The three ZnS:Mn phosphor layer deposition methods investigated for this thesis are evaporated, ALE(Cl), and ALE(DEZ). Evaporated ZnS:Mn ACTFEL devices tend to exhibit a rigid p-shift of the C-V curve with aging. [21] However, after long aging times (24 hours at 3 KHz), the C-V curve begins to exhibit rigid n-shift which saturates after a very long aging period (a week or so). ALE deposited ZnS:Mn ACTFEL devices tend to show very little change in the C-V curve if a DEZ precursor is used. ALE ZnS:Mn ACTFEL devices deposited with Cl show softening of the C-V curve when the first deposited interface is sourced, and p-shift of the C-V curve when the last deposited interface is sourced. [20]

In summary, the aging trends of importance to this thesis are (i) softening of the C-V curve, (ii) shifting of the turn-on voltage of the C-V curve, and (iii) overall degradation of the brightness of the device. Item (ii) is of particular interest because it can be correlated to the VIQ, as discussed in Chapter 4.

Chapter 3
Photo-Induced Charge and Luminescence Measurements

3.1 Introduction

Photo-induced charge (PIQ) and photo-induced luminescence (PIL) measurements have been employed by several groups for the characterization of ACTFEL devices [9, 10, 11, 12, 13, 14, 15]. PIQ and PIL experiments involve the creation of electron-hole pairs (generated by a short ultraviolet laser pulse) in the phosphor near one of the phosphor/insulator interfaces, transport of this photo-induced charge across the phosphor (aided by the application of a DC voltage across the ACTFEL stack), and measurement of the charge transferred across the phosphor layer or the luminescence emitted from the phosphor layer, respectively, as a function of the magnitude of the applied DC voltage. For a discussion of previous PIQ/PIL work, refer to, Section 2.4.

The purpose of this section is to present a PIQ/PIL study of commercial-quality evaporated ZnS:Mn ACTFEL devices of variable phosphor thickness. The trends found in this study are consistent with the work of Corlatan et al. [9, 10] In agreement with Corlatan et al., the efficiency of elecgtron transport is found to be greater than that of hole transport. In contradiction with Corlatan et al., this is attributed to hole trapping which modifies the electric field profile in the phosphor. Moreover, the data which appears to be due to hole transport is attributed to electrons being injected from the opposite phosphor-insulator interface.

A word of caution is required when comparing PIQ/PIL data of different groups. Of the three groups reporting PIQ/PIL results, all perform these experiments in a different manner. Our procedure is very close, but not identical, to that of Corlatan et al. but is very different from that of the HHI group. Differences between PIQ/PIL procedures are discussed in the following section.

3.2 Experimental Procedure

The samples used in this study are fabricated at Planar America and consist of a standard ACTFEL structure with SiON top and bottom insulators, evaporated ZnS:Mn as the phosphor layer, an indium-tin oxide (ITO) bottom contact, and aluminum top contact. The top and bottom insulator thicknesses are approximately 110 nm and 180 nm, respectively, for all three of the ACTFEL devices used in this study, whose phosphor thicknesses are 300, 700, and 950 nm, as seen in Fig. 2.1. For PIQ/PIL experiments, a ~15 nm thick semi-transparent layer of aluminum is thermally evaporated onto the sample so that a small portion of this layer overlaps neighboring thick aluminum dots, but the majority of the thin contact covers the uncontacted ACTFEL stack. The purpose of this semi-transparent aluminum layer is to allow ultraviolet laser radiation to pass through the thin contact, creating electron-hole pairs in the phosphor, and yet to allow carriers to be collected via the semi-transparent contact.

The theoretical basis of PIQ/PIL measurements is that electron-hole pairs are generated within ~40-60 nm [9] of the nearest phosphor surface by an ultraviolet laser pulse. When the aluminum contact is negatively biased, photo-induced electrons are transported across the phosphor, while holes remain close to the phosphor/insulator interface at which they are created, as seen in Fig. 3.1.

The PIQ signal is the product of the number of photo-generated electrons multiplied by the distance that each electron travels. The PIL signal is the measured luminescence that arises from impact excitation of Mn as these photo-induced electrons transit the phosphor. When the aluminum contact is positively biased, the holes traverse the phosphor, giving rise to PIQ and PIL, and electrons remain close to the phosphor/insulator interface at which they are created, as seen in Fig. 3.2.

The PIQ/PIL experimental apparatus is shown in Fig. 3.3. The ultraviolet radiation is generated by a nitrogen laser at a wavelength of 337 nm which pumps a dye laser tuned to 500 nm, which then passes through a doubling crystal to create 250 nm radiation pulses with intensity of ~1-2 nJ/pulse. Since the band gap of ZnS

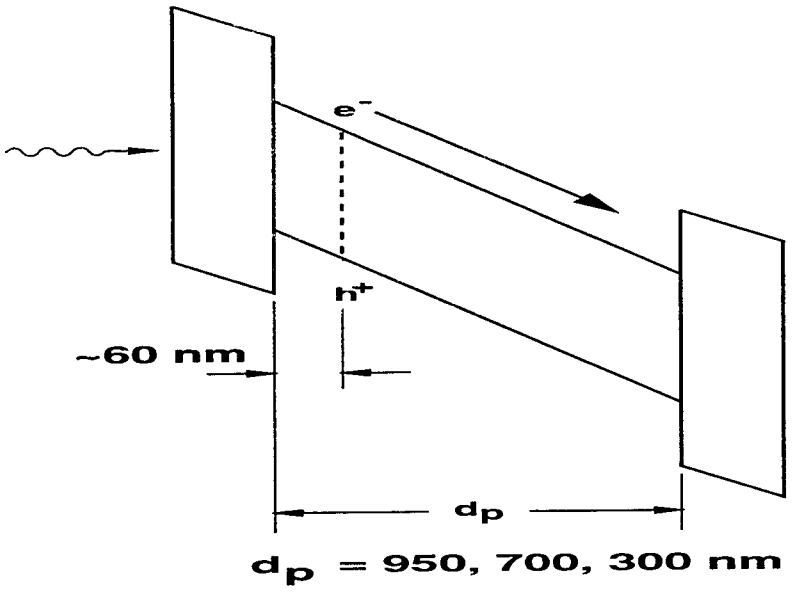

Figure 3.1. Energy bands for a negatively biased PIQ/PIL experiment.

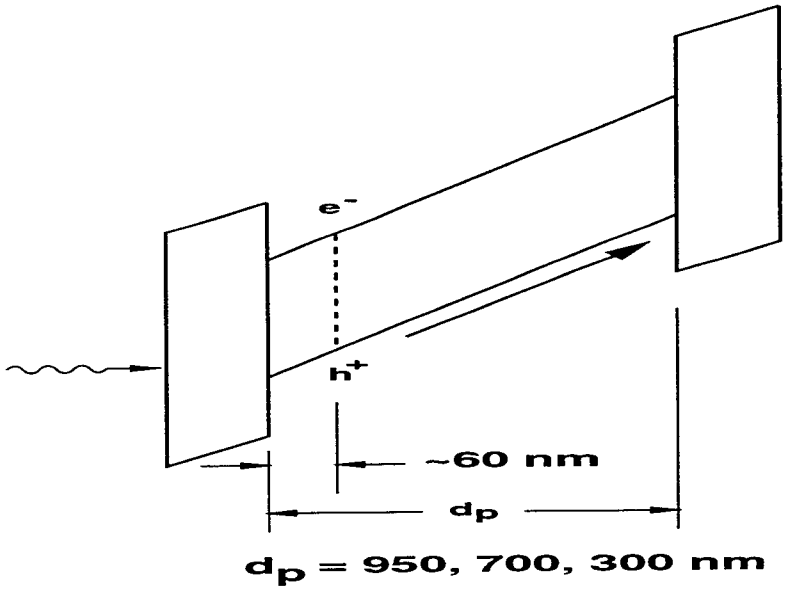

Figure 3.2. Energy bands for a positively biased PIQ/PIL experiment.

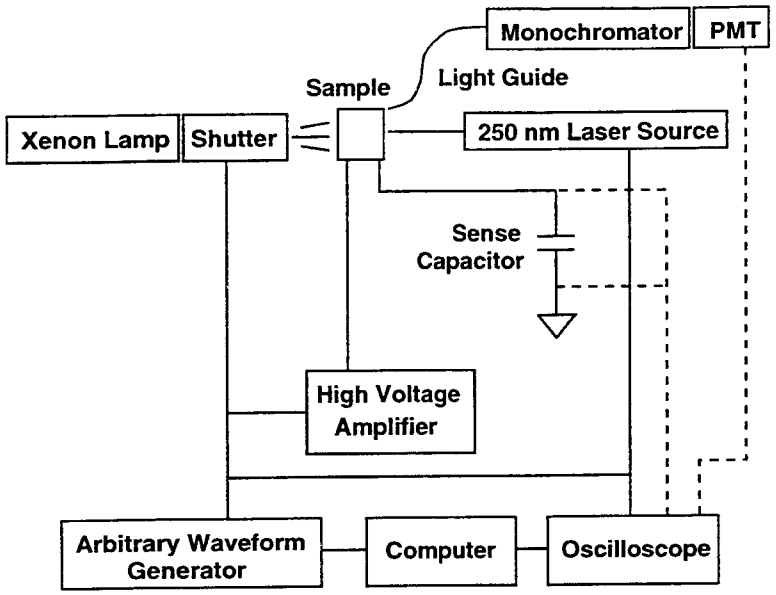

Figure 3.3. Experimental apparatus for PIQ/PIL experiments.

is 3.7 eV (330 nm), this photon energy is sufficiently large to create electron-hole pairs by band-to-band generation. The DC voltage applied to the ACTFEL device is generated by an arbitrary waveform generator (Wavetek model 395) and amplified by a high voltage amplifier. The PIQ signal is measured by means of a 100 nF sense capacitor in series with the ACTFEL device via a digitizing oscilloscope (Tektronix model TDS 420A). The PIL signal is measured by placing a fiber-optic bundle at the edge of the glass substrate and passing the collected light through a monochrometer (Jarrell-Ash model 82-140) to a photo-multiplier tube (Hamamatsu model R928) which is then monitored by the digital oscilloscope.

In a PIQ/PIL experiment, the PIQ and PIL signals are measured as a function of the magnitude of the applied voltage across the ACTFEL device.

Three different methods of obtaining PIQ/PIL were investigated: 1) no optical reset, new voltage each time. 2) electrical clearing pulse. 3) optical reset.

The first method yields preliminary results which look promising, but each laser pulse occurs with the device in a different state, i.e. interface state occupancy differs and bulk states are ionized to varying degrees based on the previous electrical pulses. For this method of accomplishing PIQ, the device is continuously electrically stimu-

lated with a laser pulse occuring every 1000 electrical pulses. Later research showed that 1000 pulses (below threshold) are not sufficient to fully eliminate the effects of the previous laser pulse. If the device is driven continuously with a 50 V pulse, the bands are bent by some amount, due to static space charge, leading to cathode field enhancement which would aid the transport of photo-injected carriers. This effect is even stronger if the device is driven by above-threshold voltage pulses. Also, once the device is driven above-threshold, space charge remains trapped in the device for a very long time. Thus, aging a device at 40 V over threshold and then operating it at low voltages gives misleading results, as the device contains a large amount of static space charge. The possible generation of static space charge below threshold is discussed in detail in the next chapter. The purpose of PIQ/PIL experiments is to optically stimulate the device with the laser while the device is experiencing a known internal field.

The lack of a constant starting point for each new voltage led to attempts to use an electrical clearing pulse, as developed by Hitt for standard electrical measurments [22]. If an ACTFEL device is driven with a constant above-threshold voltage, each new voltage/laser pulse will see the same initial condition. When voltage pulses are applied above threshold, the ACTFEL device reaches steady-state quickly, as opposed to the application of below-threshold pulses, in which case many thousands of voltage pulses are required to reach a steady state.

For electrically reset PIQ/PIL experiments, the ACTFEL device is driven at $\sim$10 - 20 V over theshold throughout the duration of the experiment; the voltage pulse which is applied concomitant with the laser pulse is varied from 0 V to 40 V over threshold. However, since space charge is present in the device due to the electrical reset pulses, all measurements, including those acquired at voltages below the threshold voltage, are influenced strongly by the presence of space charge in the phosphor. When the laser pulse is applied concomitant with a below-threshold voltage pulse, the energy bands are bent due to the space charge generated by the previous electrical clearing pulse. Thus, the results from electrically reset PIQ/PIL experiments were found to be unsatisfactory due to the space charge generated by

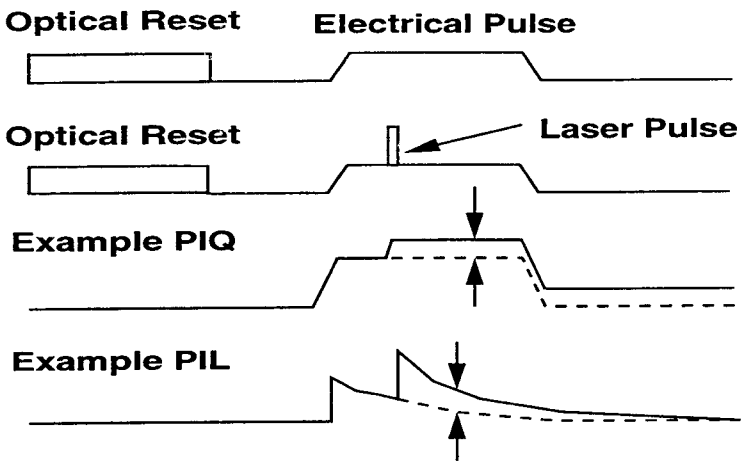

Figure 3.4. PIQ/PIL timing diagram. Dashed lines denote data acquired in the absence of the laser pulse.

the clearing pulses. This led us to the use of an optical reset pulse between each electrical/laser pulse, as described below.

To accomplish optically reset PIQ/PIL measurements, a xenon lamp is used to apply an optical reset pulse between each DC voltage/laser pulse. A timing diagram for the PIQ/PIL measurements is shown in Fig. 3.4. The ACTFEL device is first reset with a 10 s optical reset. Next, a positive voltage pulse with a 5 μs rise and fall time and a 100 μs plateau is applied. 30 μs after the beginning of the electrical pulse, a 3 ns laser pulse is applied. The maximum charge induced on the sense capacitor and the integrated area of the PMT signal (the total light output) generated by the device for that pulse are acquired by the digital oscilloscope and saved by the computer. The ACTFEL device is then optically reset again and a negative voltage pulse is applied. Once again, the maximum charge induced on the sense capacitor and the signal from the PMT is stored.

For each maximum applied voltage, two sets of PIQ/PIL data are acquired. The first set of data is obtained when the voltage pulse is applied in the absence of a laser pulse, shown in Fig. 3.4, while the second set is obtained when both the voltage

pulse and the laser pulse are applied, as seen in Fig. 3.4. These two sets of data are then subtracted from one another in order to isolate the photo-induced PIQ and PIL signals. After aquisition of four sets of data, the two sets described above for both positive and negative applied voltages, the maximum applied voltage of the pulse is increased and the process is repeated. PIQ and PIL data are taken in 5-10 V steps from 0 V to 20-40 V above threshold for three different evaporated ZnS:Mn phosphor thicknesses. Additionally, a PIQ/PIL efficiency is determined by dividing the PIL by the PIQ and is a measure of the efficiency of the photo-induced transferred charge (electrons or holes) at generating luminescence.

3.3 Experimental Results and Discussion

The experimental results of this study are presented in Figs. 3.5-3.10 in which PIL and PIQ are plotted as a function of the DC voltage applied to the ACTFEL device. In all PIL and PIQ plots, the electrons are symbolized as filled circles and the holes as empty circles. The PIL results are discussed first.

A definite PIL threshold is evident for all three ACTFEL devices measured, as seen in Figs. 3.5-3.7. This PIL threshold corresponds to the phosphor field at which the photo-injected carriers are hot enough to excite luminescent impurities. PIL is expressed in arbitrary units; no direct comparison should be made between Figs. 3.5-3.7.

All of the data sets have a base line offset which is due to the photo-luminescence (PL) response of the device. The PL response is the light produced by the laser exciting the phosphor in the absence of an electric field-induced response. Therefore, the PL offset base line can be taken as the origin when calculating the threshold field. The PIL phosphor threshold field is calculated from

$$F_{th} = \frac{C_i V_{th}}{d_p(C_i + C_p)} \tag{3.1}$$

where V_{th} is the voltage intercept of the PIL with the PL offset base line (Figs. 3.5-3.7), d_p is the phosphor thickness, and C_p and C_i are the phosphor and insulator

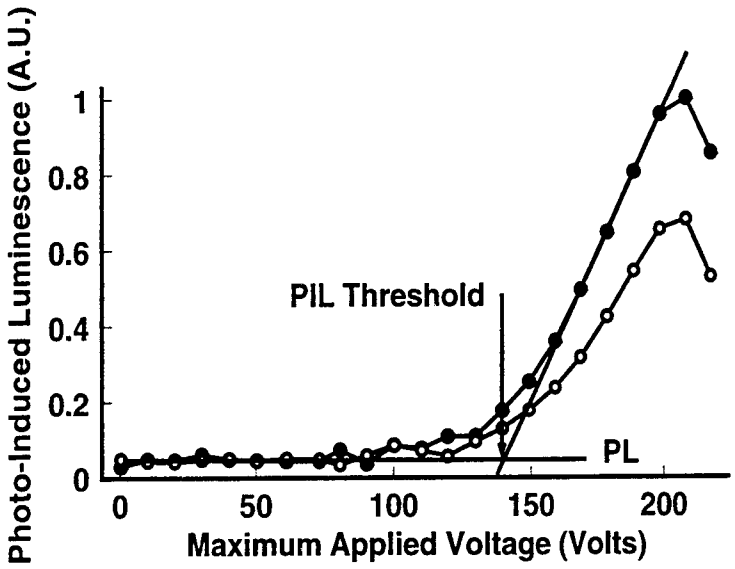

Figure 3.5. PIL of a 950 nm phosphor thickness evaporated ZnS:Mn ACTFEL device.

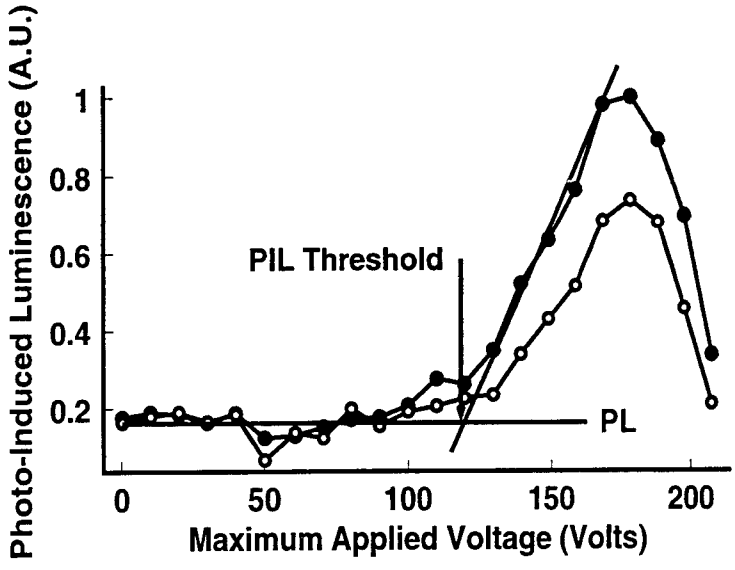

Figure 3.6. PIL of a 700 nm phosphor thickness evaporated ZnS:Mn ACTFEL device.

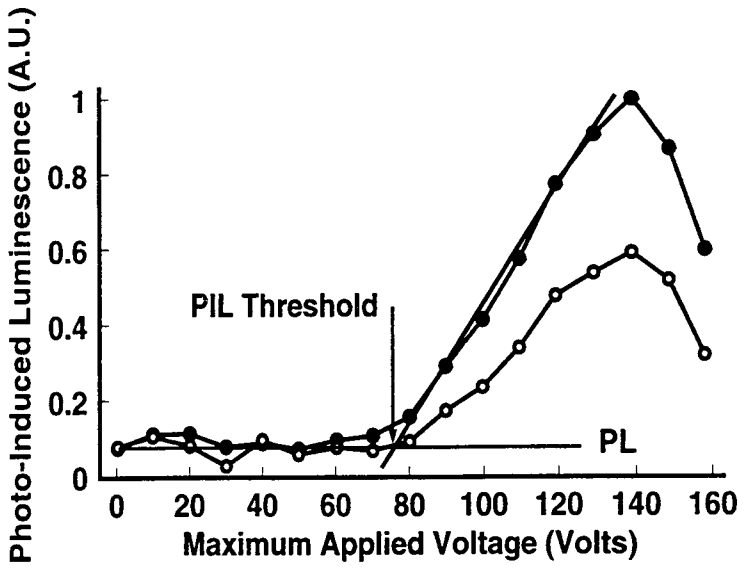

Figure 3.7. PIL of a 300 nm phosphor thickness evaporated ZnS:Mn ACTFEL device.

capacitances, respectively. The calculated phosphor threshold fields are 1.05 MV/cm for the 950 nm sample, 1.04 MV/cm for the 700 nm sample, and 1.03 MV/cm for the 300 nm sample, as obtained from Figs. 3.5-3.7, respectively. The data sets show a PIL threshold for the holes as well, but it is the contention of this thesis that these thresholds actually arise from electron injection from the opposite interface, as discussed below. The reason that the PIL reaches a peak and then decreases is believed to be an artifact arising from the difference curve analysis; the photo-injected carriers contribute a small fraction of the light at higher fields where electroluminescence dominates. Therefore, the data points for voltages greater than the peak voltage are not meaningful and the PIL peak is not significant.

The measured PIL threshold of ~1.04 MV/cm is somewhat larger than the 0.7 MV/cm threshold field for impact excitation calculated via a full-band Monte Carlo simulation, but it is in excellent agreement with the band-to-band impact ionization threshold of 1 MV/cm from the Monte Carlo calculation. [23] Thus, a comparison of the experimental PIL results and the full-band Monte Carlo simulation suggests that the PIL threshold may be associated with the onset of electron multiplication due

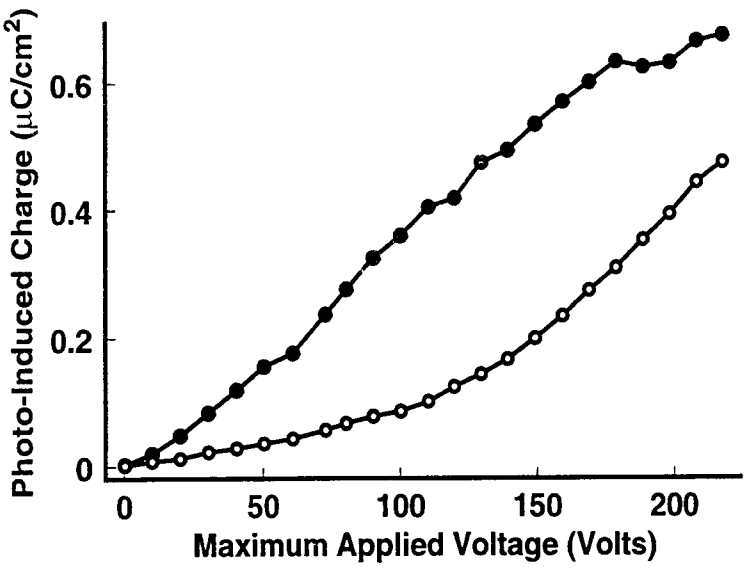

Figure 3.8. PIQ of a 950 nm phosphor thickness evaporated ZnS:Mn ACTFEL device.

to band-to-band impact ionization. This suggests that PIL is not due to only the photo-injected carriers but is also due to carriers created by impact ionization. Alternatively, it is possible that the experimentally deduced 1.04 MV/cm PIL threshold corresponds to the onset of Mn impact excitation and that the disagreement between the measured and Monte Carlo simulated impact excitation thresholds arises because of uncertainties in the the Monte Carlo simulation parameters.

Although this second interpretation is possible, it is preferable to attribute the measured PIL threshold as arising from the band-to-band impact ionization threshold for two reasons. First, in Figs. 3.5-3.7, no evidence for a second threshold corresponding to the onset of band-to-band impact ionization is observed. Second, it is believed that an important condition for efficient ACTFEL operation is that the threshold field for band-to-band impact ionization be less than or equal to the threshold for impact excitation. In an ACTFEL device, this condition leads to electron multiplication of carriers sourced from interface states.

The PIQ curves for the ACTFEL device with a phosphor thickness of 950 nm clearly show a region below 125 V where the holes are not as efficient at traversing

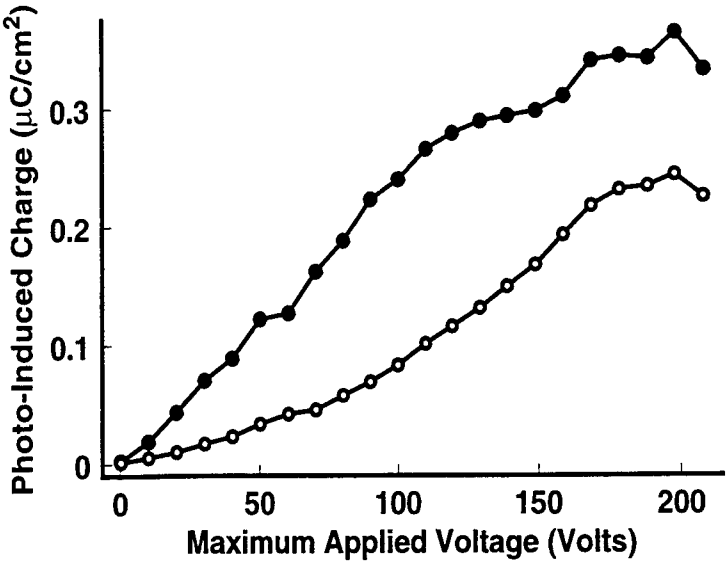

Figure 3.9. PIQ of a 700 nm phosphor thickness evaporated ZnS:Mn ACTFEL device.

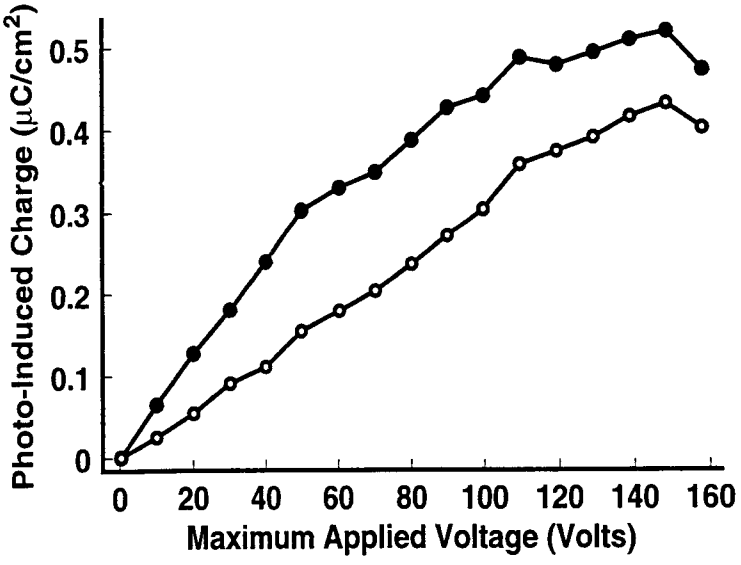

Figure 3.10. PIQ of a 300 nm phosphor thickness evaporated ZnS:Mn ACTFEL device.

the phosphor, as seen in Fig. 3.8. In contrast, above 125 V the electrons and holes have approximately the same PIQ efficiency, since the slope of the PIQ curve above 125 V is the same for both electrons and holes (i.e. the slope of a PIQ curve can be viewed as a PIQ efficiency). The ACTFEL device with a phosphor thickness of 700 nm exhibits a similar trend, with lower hole PIQ efficiency below 75 V, and a similar PIQ efficiency for electrons and holes above 75 V, as seen in Fig. 3.9. The ACTFEL device with a phosphor thickness of 300 nm shows the electron PIQ efficiency to be higher below 50 V and similar PIQ efficiency for electrons and holes above 50 V, as shown in Fig. 3.10. The voltage at which the PIQ efficiency changes corresponds to an internal phosphor field of ~0.8 MV/cm for all three ACTFEL devices. This value is in agreement with the findings of Lee et al. [23], who performed Monte Carlo simulations of high-field electron transport in ZnS and calculate an impact excitation threshold of 0.7 MV/cm. The value of 0.8 MV/cm obtained from the PIQ experiment is an average field across the phosphor, the cathode field is significantly larger if space charge is present, as discussed below.

The interpretation of these PIQ results suggests hole trapping in the phosphor for lower fields; the PIQ efficiency of holes is less than that of the electrons since a significant fraction of the photo-injected holes are trapped in the phosphor, while the electrons transit the phosphor layer with very little trapping. This interpretation of the PIQ data in terms of hole trapping is consistent with the analysis of Corlatan et al. [9, 10].

As mentioned previously, the hole PIQ efficiency seems to be approximately equal to the electron PIQ efficiency above a certain maximum applied voltage (~125, ~75, and ~50 for ACTFEL devices with 950 nm, 700 nm, and 300 nm, respectively). Corlatan el al. [9, 10] interpreted this as evidence that Mn impact excitation can occur via hot holes. In contrast, another explanation of the experimental trends is offered below.

It is more likely that the apparent hole transport is actually due to electron transport in which electrons are injected from the opposite interface (i.e. back injection). As holes are trapped in the phosphor, the energy bands are bent, causing

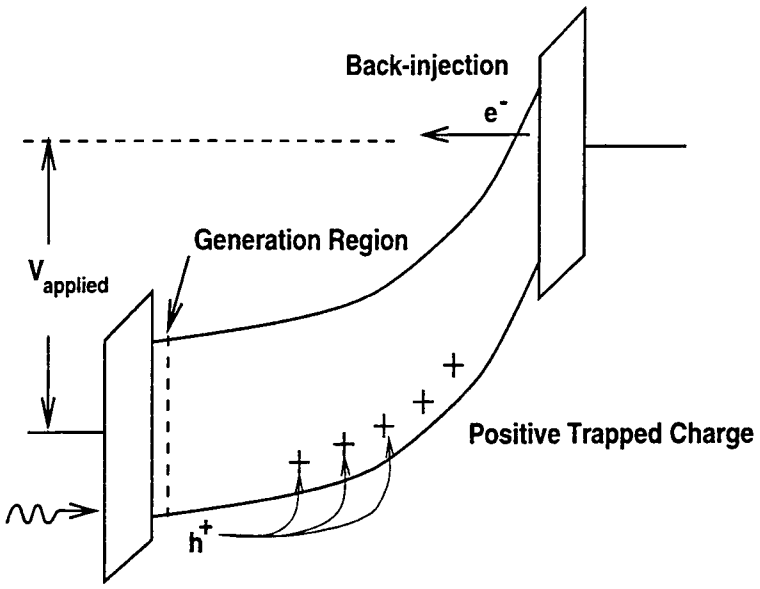

Figure 3.11. Apparent hole PIQ due to electron back injection.

an increase in the backside cathode field which effectively lowers the tunnel injection barrier, as shown in Fig. 3.11. Thus, the apparent increase in the hole PIQ efficiency at maximum applied voltages greater than ~125, ~75, and ~50 in Figs. 3.8-3.10, respectively, would actually correspond to an onset of electron injection from the backside cathode interface. It is impossible to distinguish holes moving away from the interface from electrons moving towards it. However, if back injection of electrons does indeed occur, a shift in the PIQ threshold towards higher voltages with lower laser intensity would be expected, due to less hole trapping and a concomitant reduction in the cathode field enhancement. This hypothesis is tested by aquiring a second set of PIQ experiments using a laser intensity ~100 times less than that used to acquire the first set of data, see Figs. 3.12-3.14.

For all three ACTFEL devices, a shift in the PIQ curve toward higher voltages with reduced laser intensity is observed, consistent with the hypothesis that the apparent transport of holes is actually the transport of electrons injected from the opposite interface.

If hole trapping and backside injection are invoked to explain the observed increase in the hole PIQ efficiency for phosphor fields greater than ~0.8 MV/cm, it

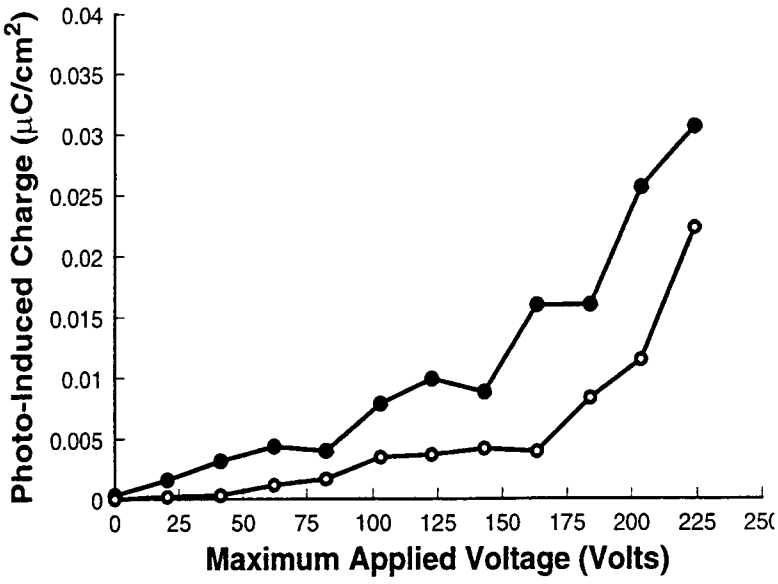

Figure 3.12. Lower laser intensity PIQ measurement of a 950 nm ZnS:Mn ACTFEL device.

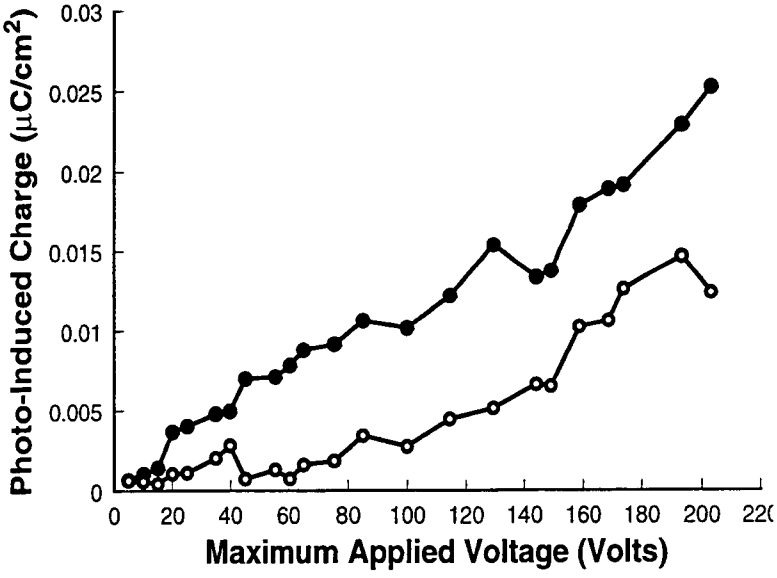

Figure 3.13. Lower laser intensity PIQ measurement of a 700 nm ZnS:Mn ACTFEL device.

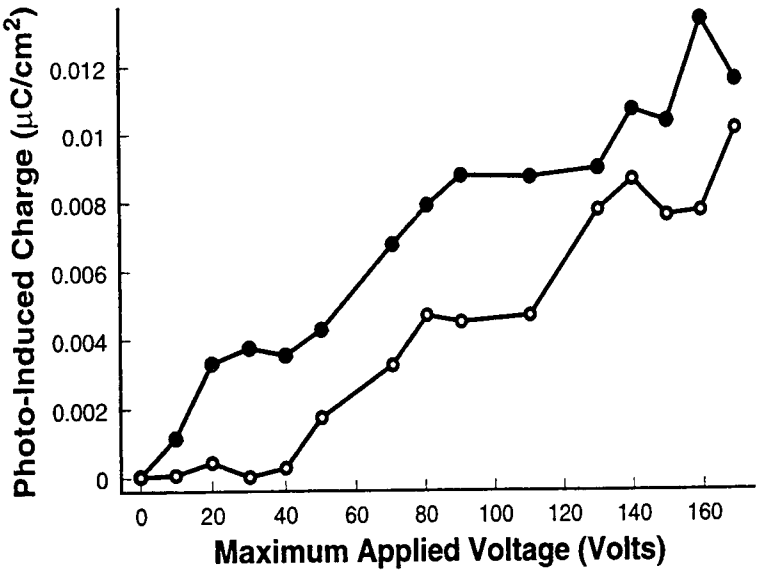

Figure 3.14. Lower laser intensity PIQ measurement of a 300 nm ZnS:Mn ACTFEL device.

is possible to estimate the trapped hole concentration, ρ. This is accomplished by assuming a cathode field of 2.2 MV/cm [24] and using

$$\rho = [F_p^{cathode} - F_p^{measured}]\frac{2\epsilon_p}{d_p} \tag{3.2}$$

which implicitly assumes a uniform distribution of trapped holes. Use of Eq. 3.2 yields an estimated ρ of ~1-5 x 10^{17} cm^{-3} for the three ACTFEL devices tested. These estimates do not seem unreasonable since they are somewhat larger than the 7 x 10^{16} cm^{-3} estimates of the static space charge charge density for evaporated ZnS:Mn ACTFEL devices. [22, 24]

A drift length for holes may be estimated from the PIQ measurement. If the electrons are assumed to transit completely across the phosphor, then at a given voltage, the ratio of the hole PIQ to the electron PIQ multiplied by the phosphor thickness of the device should yield an estimate of the average distance that holes travel prior to being trapped (i.e. the drift length) at that applied voltage. Fig. 3.15 is a plot of the drift length as a function of the internal phosphor field.

Note that the lowest field points plotted in Fig. 3.15 are not reliable because of the PIQ uncertainties. Also, the upward trend in the hole drift length of Fig. 3.15 for

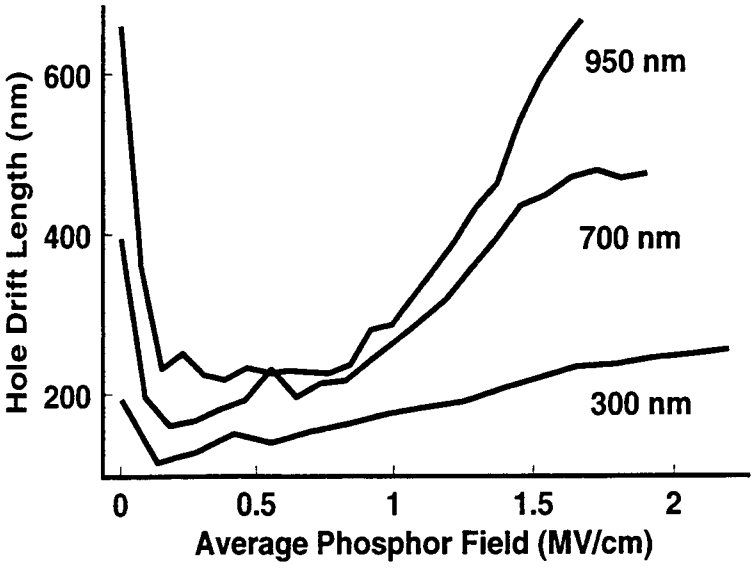

Figure 3.15. Hole drift length, as estimated by the PIQ hole to electron ratio, as a function of applied phosphor field for three different evaporated ZnS:Mn ACTFEL devices.

phosphor fields greater than ~0.8 MV/cm arises from the onset of backside electron injection, not an enhancement in the hole drift length. Thus, taking the relatively constant, low-field portion of Fig. 3.15 as a measure of the drift length, the hole drift length is estimated to be ~180±70 nm. If holes are assumed to travel at a saturated drift velocity of ~10^7 cm/s, then the drift distance can be used to deduce an average hole lifetime of ~2 ps. Furthermore, if the hole trap density is assumed to be 7 x 10^{16} cm^{-3} [22, 24], the hole trap capture cross section can be estimated from

$$\sigma = \frac{1}{\tau v_{sat} N_t} \tag{3.3}$$

where τ is the hole lifetime, v_{sat} is the saturated drift velocity, and N_t is the trap density. Equation 3 yields an estimated capture cross-section of ~7 x 10^{-13} cm^{-2}. This is a relatively large capture cross section. Capture cross-sections of this magnitude correspond to a coulombically attractive interaction between a trap and the carrier to be trapped. [25] Thus, the large magnitude of this capture cross section suggests that the trap is negatively charged prior to hole capture. It is speculated that this hole trap is a zinc vacancy or, more likely, a zinc vacancy complex, since

a zinc vacancy is a double acceptor. More work is required to conclusively identify the physical nature of this hole trap.

Returning to the PIQ curves shown in Figs. 3.8-3.10, it is puzzling that the electron PIQ signal increases monotonically over the entire range of the maximum applied voltage. Since the strength of the PIQ signal is determined by the integral of the product of the number of carriers transported times the distance that they travel before being trapped, the monotonic nature of the electron PIQ signal appears to suggest that either (i) more carriers are transported at larger applied voltages, or (ii) carriers travel further at larger maximum applied voltages before being trapped. Possibility (i) is preferred for explaining the electron PIQ trends shown in Figs. 3.8-3.10. Two possible reasons for carrier enhancement are offered. First, at the higher phosphor fields concomitant with a larger applied voltage there may be an increase in the number of transported carriers due to electron multiplication of the photo-induced carriers as they transit the phosphor. Such electron multiplication could occur via trap-to-band impact ionization, for example. Second, given the large number of photons injected into the phosphor, it is likely that electron-hole pair recombination of photo-injected carriers in the region near the incident interface will be very high in the absence of an applied field. When an external field is applied, more carriers will be extracted from the recombination region before they have a chance to recombine, leading to the lack of saturation of the PIQ curves. If this second mechanism is operative, the PIQ efficiency would be due to the extraction efficiency of the photo-injected carriers as well as to the transport efficiency.

Finally the quantum efficiency, which is defined as the ratio of the PIL to the PIQ, is shown in Figs. 3.16-3.18. These curves could be interpreted as indicating that electrons and holes are equally efficient in exciting luminescent impurities, as reported by Corlatan et al. [9, 10]. A more likely explanation, as mentioned previously, is that the apparent hole transport trends are actually due to electron injection from the opposite interface. This process is more efficient because hole trapping significantly perturbs the electric field profile due to the formation of positive space charge. This is in contradiction with the findings of Corlatan et al. [9, 10] who conclude that the

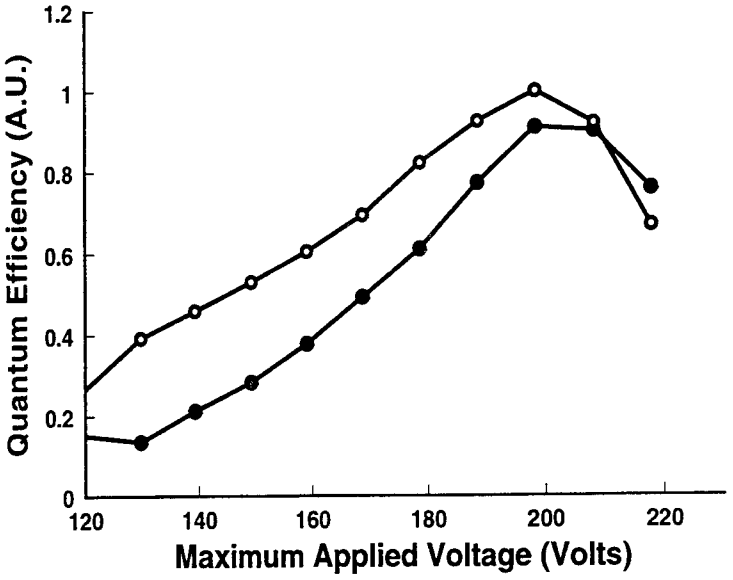

Figure 3.16. Quantum efficiency of a 950 nm ZnS:Mn ACTFEL device.

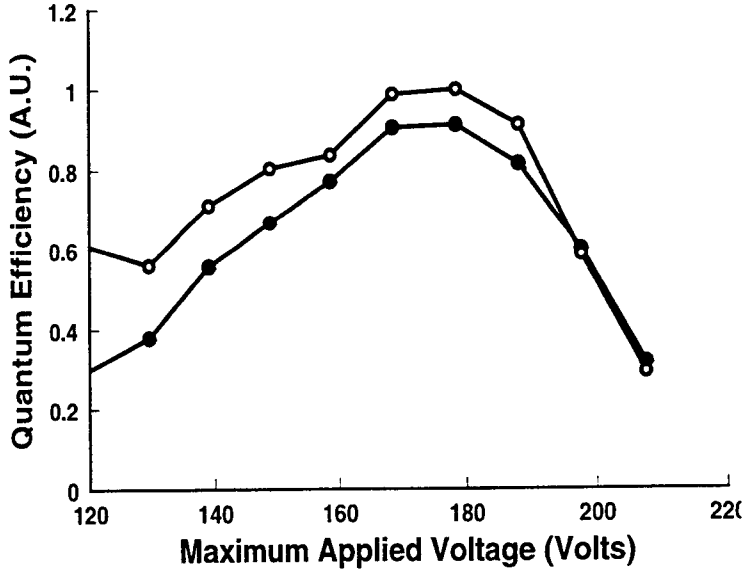

Figure 3.17. Quantum efficiency of a 700 nm ZnS:Mn ACTFEL device.

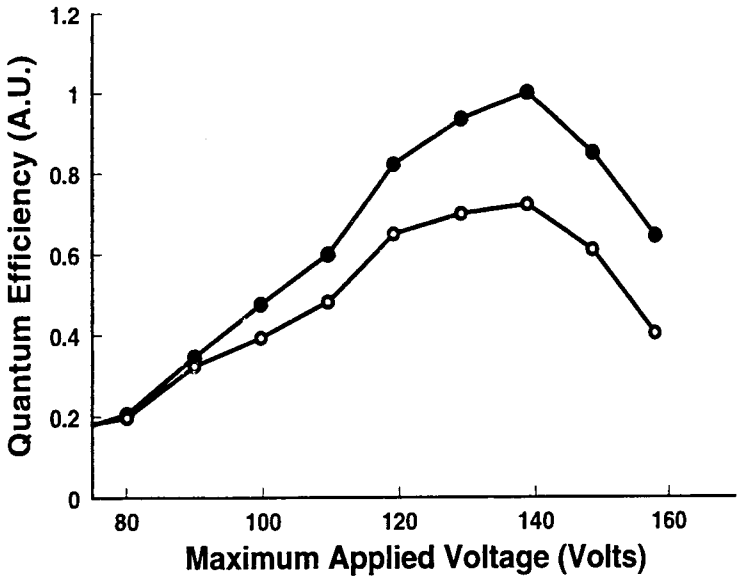

Figure 3.18. Quantum efficiency of a 300 nm ZnS:Mn ACTFEL device.

hole-initiated PIQ/PIL trends are due to holes, and that hole-initiated Mn excitation is more efficient than electron-initiated Mn excitation.

3.4 PIQ/PIL Conclusions

Photo-induced charge (PIQ) and photo-induced luminescence (PIL) measurements of evaporated ZnS:Mn ACTFEL devices with variable phosphor thicknesses provide information related to the transport of electrons and holes in the ZnS phosphor. The PIL threshold field for electron transport is estimated to be ~1.04 MV/cm. It is suspected that this PIL threshold corresponds to the onset of electron-induced band-to-band impact ionization, in agreement with Monte Carlo simulation of high-field transport in ZnS. [23] However, it is possible that this threshold arises from the onset of electron-induced impact excitation of Mn. The hole PIL threshold is found to be an artifact due to electron injection from the interface opposite from which the photo-induced holes are created. Hole PIQ curve trends are dominated by hole trapping. Hole trapping is characterized by a drift length of ~180±70 nm, a hole lifetime of ~2 ps, and a trap capture cross-section of ~7 x 10^{-13} cm^2. This is

a large capture cross section, corresponding to a negatively charged deep level trap whose charge state leads to very efficient hole capture due to the attractive coulombic interaction between the trap and the hole. It is speculated that this hole trap is most likely a defect complex involving a zinc vacancy.

Chapter 4
Subthreshold Voltage-Induced Transferred Charge

4.1 Introduction to VIQ

The ACTFEL device characterization experiment discussed in this chapter is denoted subthreshold voltage-induced transferred charge (VIQ). The apparatus used to accomplish VIQ is very similar to the apparatus used for standard electrical characterization, but differs in that a xenon lamp is used to periodically optically reset the phosphor to a flat-band condition, as shown in Fig. 4.1. The experiment is performed by applying 20,000 trapezoidal bipolar pulses (5 μs rise/fall time and a 30 μs plateau applied at 1 kHz) immediately followed by an optical pulse from a xenon lamp. It is found that ~10,000 bipolar voltage pulses are needed to reach steady-state operation of the ACTFEL device when the voltage pulses are below the EL conduction threshold, as discussed in Appendix A.1. The voltage of the bipolar pulses is varied from zero volts up to the EL conduction threshold. The VIQ signal is the peak voltage induced on a sense capacitor in series with the ACTFEL device immediately following the application of a light pulse from the xenon lamp, as shown in Fig. 4.2.

The operating hypothesis of this investigation is that the VIQ signal arises from a redistribution of charge within the phosphor. Most likely, this charge redistribution is due to applied-voltage-induced-ionization of relatively shallow traps; ionization of traps generates both space charge and free carriers which are subsequently transferred within the phosphor due to the applied voltage. The distinction between space charge and transferred charge is that space charge is localized charge within the phosphor, while transferred charge is due to carrier transport in the phosphor. Transport of the ionization charge (i.e. transferred charge due to ionization of traps within the phosphor) towards one of the interfaces and subsequent trapping of this ionization

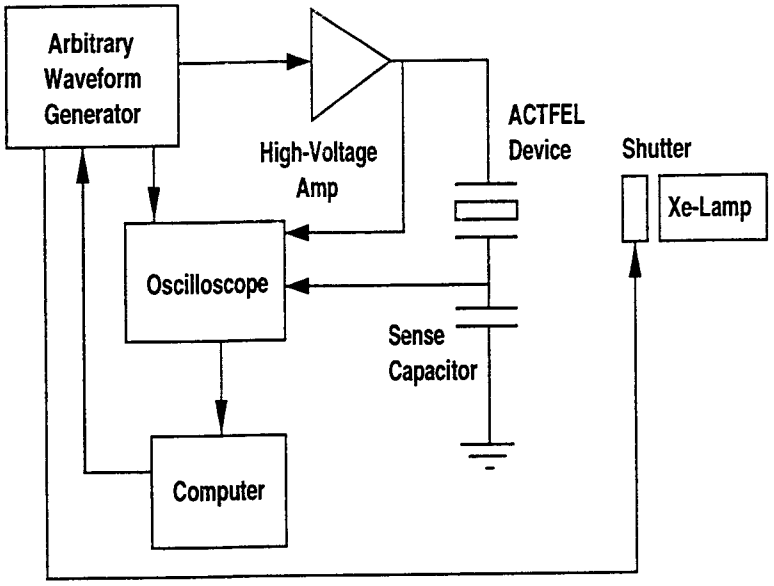

Figure 4.1. Experimental apparatus for VIQ measurements.

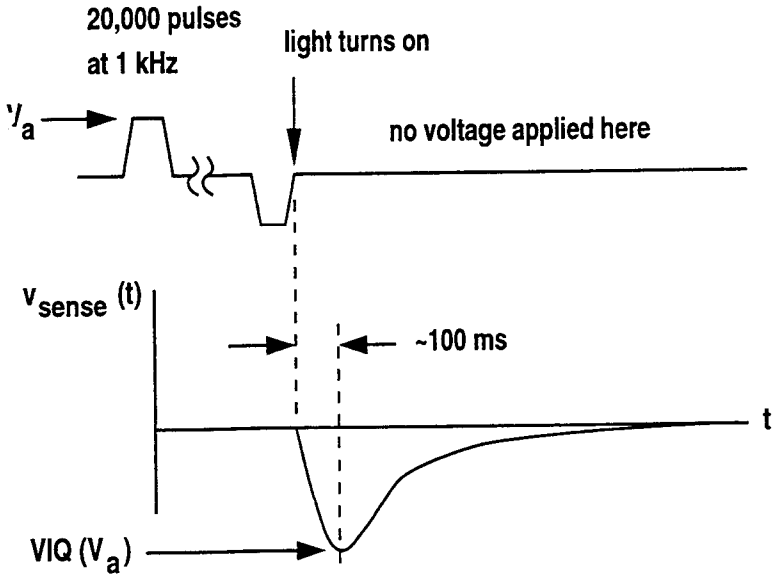

Figure 4.2. Timing diagram for a VIQ experiment.

charge into empty trap states which are presumably deeper than the traps from which the carriers were originally sourced, may give rise to the VIQ signal. Subsequent flooding of the ACTFEL device with electron-hole pairs via optical excitation from the xenon lamp is believed to eliminate (or at least reduce) space charge in the phosphor by resetting traps within the phosphor to charge states consistent with an approximately flat-band situation.

Due to the n-type nature of ZnS, it is assumed that the traps responsible for VIQ are all electron traps. The activity of a hole trap is dependent on the presence of holes in the phosphor. No source of holes is present in an n-type material; therefore, all traps referred to later in this section are assumed to be electron traps.

4.2 Experimental Procedure

VIQ experiments are performed using 20,000 (20 s) bipolar voltage pulses and a 20 second optical reset, as indicated in Fig. 4.2. To accomplish VIQ experiments, an oscilloscope is used to monitor the transient charge across the sense capacitor, $v_{sense}(t)$. As shown in Fig. 4.1, the ACTFEL device is in series with a sense capacitor. The ACTFEL device is illuminated by the xenon lamp during the optical resetting of the device, as shown in Fig. 4.1. The oscilloscope is triggered concomitant with the beginning of the light pulse, as shown in Fig. 4.2. The charge induced on the sense capacitor reaches a peak value $\sim$100 ms after the beginning of the xenon lamp pulse. The peak of the VIQ signal (as shown in Fig. 4.2) is attributed to a relatively constant flow of charge from the ACTFEL device during the application of the light pulse, as discussed in Appendix A.2. The VIQ response subsequently decays to zero within $\sim$5 s, as shown in Fig. 4.2. The duration of this decay is a result of the RC time constant of the system; no charge is redistributed 3 or 4 seconds after the application of the xenon lamp pulse.

A VIQ curve is generated by plotting the peak optically-induced charge on the sense capacitor, denoted VIQ, as a function of the maximum applied voltage, V_a of the 20,000 electrical setting pulses, as shown in Fig. 4.3. The specific trends of the

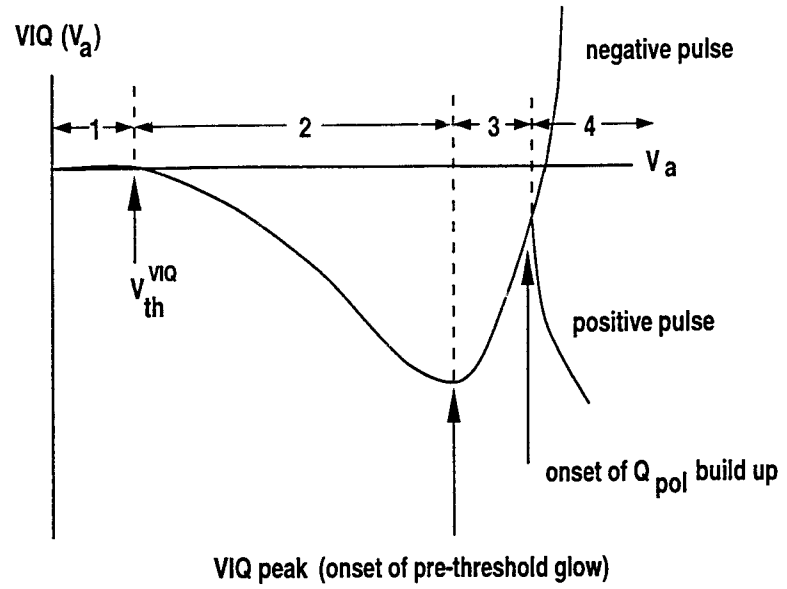

Figure 4.3. Example of a VIQ curve.

VIQ curves are discussed separately for each type of ZnS:Mn ACTFEL device in the experimental results section of this chapter.

It is observed that when the VIQ experiment is performed with single wavelength excitation, the VIQ response peaks at an excitation wavelength of ~325 nm (~3.8 eV), as discussed in Appendix A.3. The VIQ spectral response leads to the conclusion that VIQ is due to electron-hole pairs generated near the phosphor-insulator interface through which the light is incident. It is also observed that the polarity of VIQ is independent of whether the light is incident through the ITO interface or the Al interface, as discussed in Appendix A.4.

VIQ measurements are also performed using a buffer amplifier between the sense capacitor and the oscilloscope such that the sense capacitor voltage does not have a path to ground. This method of performing VIQ is accomplished by optically resetting the ACTFEL device and then measuring the peak charge induced on the sense capacitor immediately following the application of the bipolar electrical pulses. Use of a buffer amplifier for VIQ measurments does not appear to be an optimal means of acquiring data, as discussed in Appendix A.5.

4.3 Description of a VIQ Curve

Four distinct regions are seen on the generic VIQ curve shown in Fig. 4.3:

(i) Region 1 corresponds to below VIQ threshold operation; no charge is redistributed during the electrical pulses and no charge is reset during the optical pulse.

(ii) Region 2 corresponds to operation between the VIQ threshold and the onset of pre-threshold glow. In this region, the magnitude of the VIQ signal increases but no visible light is emitted from the ACTFEL device during application of the bipolar voltage pulses. In this regime, VIQ charge flows in a unidirectional manner from regions in the phosphor which possess the shallowest filled traps to regions with deeper traps. The threshold voltage for the onset of VIQ is denoted V_{th}^{VIQ}, as indicated in Fig. 4.3.

(iii) Region 3 begins with the onset of pre-threshold glow and ends with the onset of significant EL conduction. The onset of pre-threshold glow corresponds to the voltage necessary to cause the ACTFEL device to first emit light. The spectrum of the pre-threshold glow is consistent with impact excitation of Mn luminescent impurities. The VIQ signal is believed to decrease in magnitude above the onset of the pre-threshold glow because there is a competition between unidirectional VIQ charge and bidirectional (i.e. the charge moves in either direction, subject to the polarity of the bipolar electrical pulse) pre-threshold conduction charge. When the amount of pre-threshold conduction charge is approximately as large as the VIQ charge, the unipolar VIQ charge distribution is extinguished by the bidirectional flow of conduction charge. It is observed that the VIQ response for voltages below the EL conduction threshold is independent of the polarity of the last applied bipolar voltage pulse (due to the fact that very little charge is transferred per pulse).

(iv) Region 4 corresponds to operation above the EL conduction threshold. The VIQ response bifurcates with respect to the polarity of the last voltage pulse and grows precipitously when the conduction threshold is reached due to the formation of polarization charge. The magnitude and polarity of the polarization charge depends on

the polarity of the last pulse in the applied bipolar voltage pulse train. Polarization charge is the charge stored within the phosphor following an electrical pulse above the EL conduction threshold. Above the EL conduction threshold, the magnitude of the polarization charge is much greater than the magnitude of the VIQ. Thus, when an optical pulse is applied following electrical pulses above the EL conduction threshold, the redistribution of polarization charge, rather than the redistribution of charge generated by the ionization of traps, is measured.

Three important aspects of VIQ curves, such as the one shown in Fig. 4.3, are established in the following discussion of this section. First, the VIQ threshold voltage, denoted V_{th}^{VIQ}, may be used to estimate the depth of the shallow traps responsible for VIQ, as discussed in Section 4.4. Second, the onset of pre-threshold glow may be accurately assessed from the voltage at which the VIQ reaches a peak. Third, the EL conduction threshold may be precisely determined from the voltage at which the VIQ bifurcates due to the onset of significant polarization charge buildup.

4.4 Analysis of VIQ Curves

Four important features of a VIQ curve are: (i) the polarity of VIQ, (ii) the magnitude of the VIQ peak, (iii) the voltage at which the VIQ peak(s) occur (i.e. the onset of pre-threshold glow), and (iv) the voltage at which VIQ is first observed, denoted V_{th}^{VIQ}, as shown in Fig. 4.3. Prior to discussing each of these topics in detail, an analysis of possible phosphor energy band diagrams which could give rise to VIQ is presented.

4.4.1 Polarity of VIQ Signal

The polarity of the VIQ signal may yield information about the location of the traps responsible for VIQ. VIQ polarity may also yield information about the donor or acceptor-like nature of the traps. Figures 4.4-4.7 show several possible VIQ energy band diagrams during the optical reset portion of the experimental sequence when

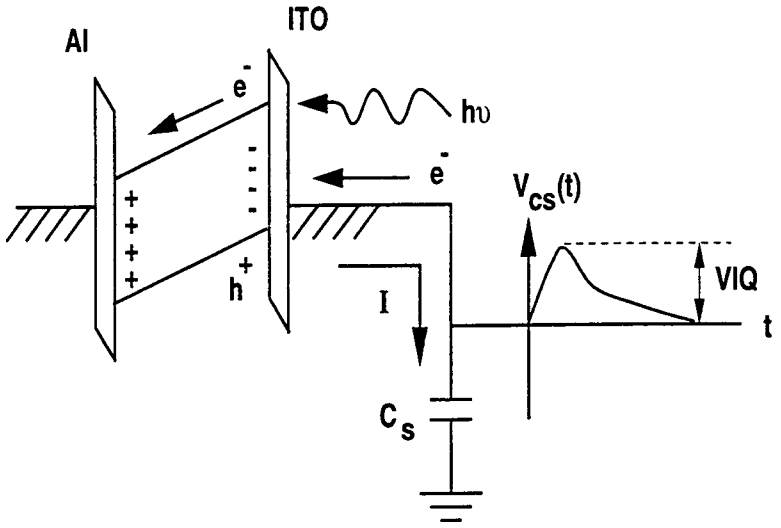

Figure 4.4. VIQ energy band diagram showing negative charge trapped at or near the bottom (ITO) phosphor/insulator interface. For this case, transport of photo-injected electrons generated near the bottom (ITO) interface gives rise to a positive polarity VIQ signal.

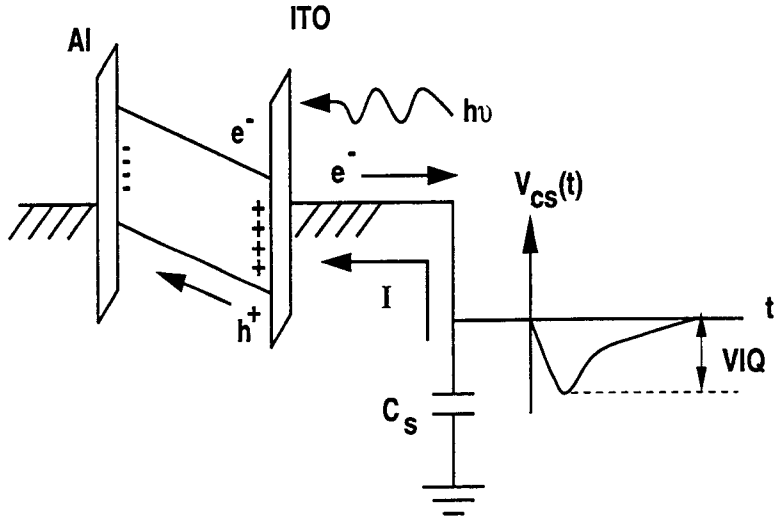

Figure 4.5. VIQ energy band diagram showing positive charge trapped at or near the bottom (ITO) phosphor/insulator interface. In this case, transport of photo-injected holes generated near the bottom (ITO) interface gives rise to a negative polarity VIQ signal.

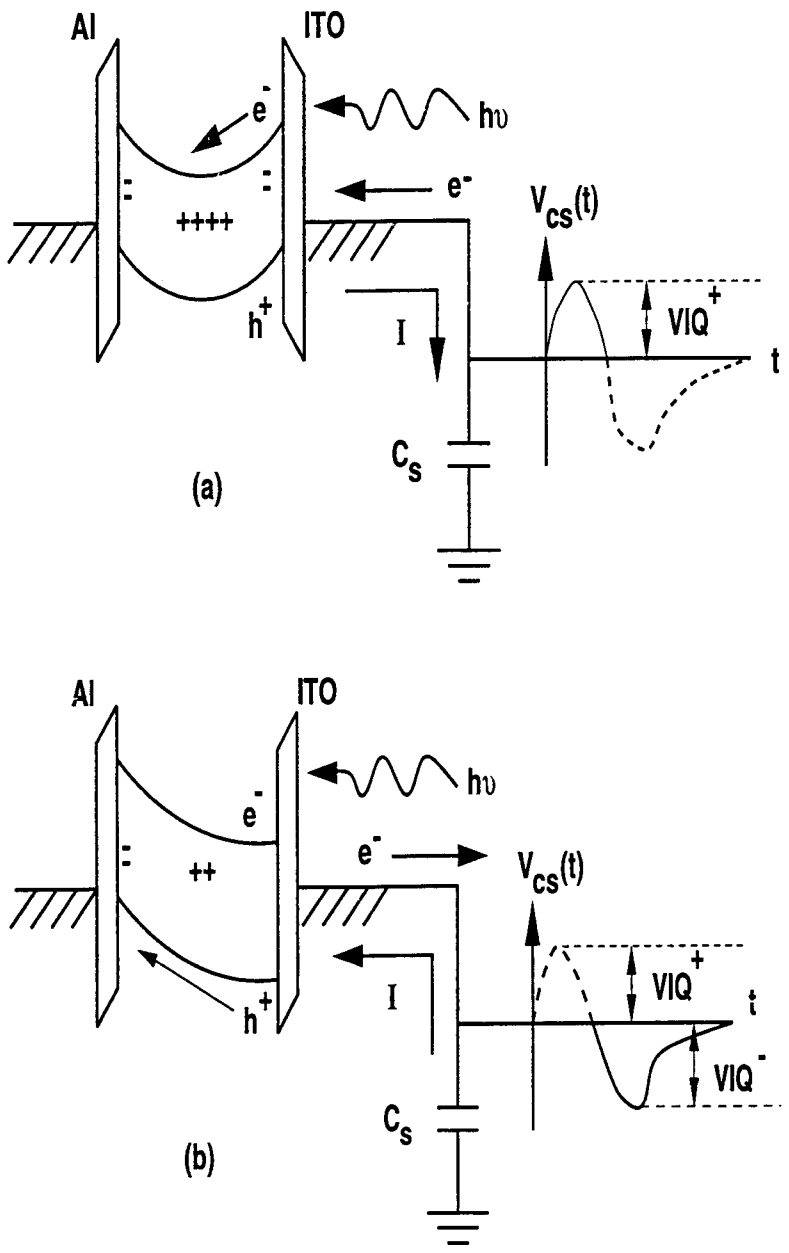

Figure 4.6. VIQ energy band diagram showing positive bulk space charge. (a) Initially, transport of photo-injected electrons generated near the bottom (ITO) interface gives rise to a positive polarity VIQ signal, as sensed on a capacitor connected to the ITO side of the ACTFEL device. These photo-injected electrons also recombine with ionized traps, yielding the energy band picture shown in (b). (b) After some positive bulk space charge has been annihilated by the initial photo-injected electrons, transport of photo-injected holes gives rise to a negative polarity VIQ signal.

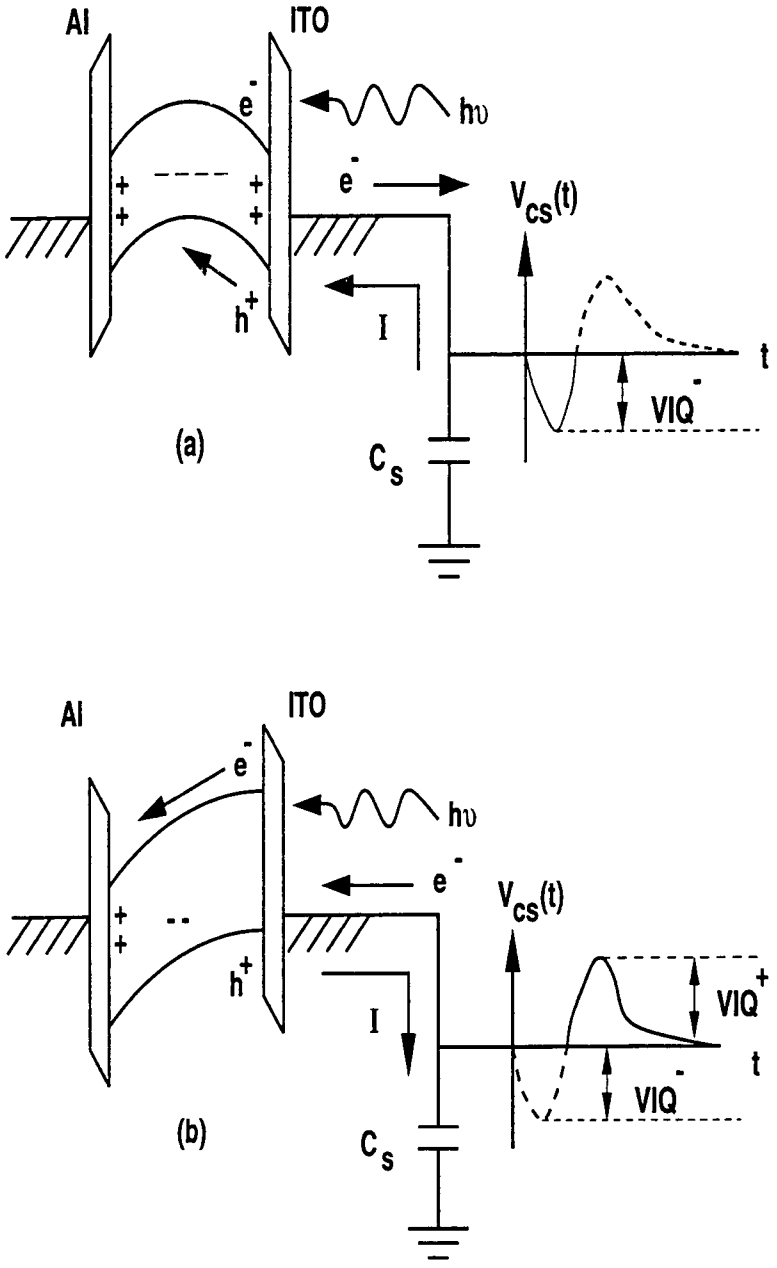

Figure 4.7. VIQ energy band diagram showing negative bulk space charge. (a) Initially, transport of photo-injected holes generated near the bottom (ITO) interface gives rise to a negative polarity VIQ signal, as sensed on a capacitor connected to the ITO side of the ACTFEL device. These photo-injected holes also recombine with ionized traps, yielding the energy band picture shown in (b). (b) After some negative bulk space charge has been annihilated by the initial photo-injected holes, transport of photo-injected electrons gives rise to a positive polarity VIQ signal.

the VIQ signal is monitored as the maximum transient voltage developed across the sense capacitor. Note that the energy band diagrams chosen correspond to the simplest possible space charge distributions. Furthermore, these figures indicate that a given space charge distribution can give rise to VIQ curves with positive or negative polarities. Certain charge distributions, such as those shown in Figs. 4.6-4.7, may give rise to a transient across the sense capacitor in which there is both positive and negative polarity VIQ signal; these are referred to as dual polarity VIQ signals. Dual polarity VIQ is observed in high-temperature measurements of ALE(DEZ) ACTFEL devices, and at room temperature for SrS:Ce ACTFEL devices. Experimental data shown in Sections 4.5.1 and 4.5.6 show that positive, negative, and dual polarity VIQ signals are possible.

The simplest possible VIQ space charge distribution is shown in Fig. 4.4, which shows negative charge near the bottom (ITO) interface and positive charge near the top (Al) interface. The VIQ space charge shown in Fig. 4.5 is identical to that shown in Fig. 4.4 except that the polarities of the charge trapped at the interfaces are reversed. For both of these cases, the unidirectional VIQ charge is assumed to be sourced from traps at one interface and trapped at deeper trap states at the opposite interface. Such an interfacial charge trapping situation yields a simple energy band picture in which the field is uniform across the phosphor. When the device is flooded with above-bandgap energy photons following the application of the bipolar voltage pulses, the photo-injected electron-hole pairs generated in the phosphor are transported subject to the internal phosphor field established by space charge within the ACTFEL device. The VIQ polarity is established by the direction of flow of the photo-generated carriers, as illustrated in Figs. 4.4-4.5. Additionally, the energy band pictures shown in Figs. 4.4 and 4.5 show that the VIQ polarity does not change if the photo-injected carriers are generated by illumination from the opposite interface (i.e. the top (Al) interface).

Experiments show the VIQ polarity to be independent of whether the ACTFEL device is illuminated from the ITO side or the Al side for all ACTFEL devices included in this thesis, as discussed in Appendix A.4. Thus, the energy band diagrams

shown in Figs. 4.4 and 4.5 are consistent with the experimental results reported in Sections 4.5.1-4.5.6.

A slightly more complicated phosphor energy band diagram showing positive bulk space charge is shown in Fig. 4.6 (a). In this case, transport of photo-injected electrons initially yields a positive polarity VIQ signal when illuminated from the ITO side which then becomes a negative polarity VIQ signal due to hole transport, as shown in 4.6 (b). In contrast, when the ACTFEL device is illuminated from the Al side, the energy band diagrams shown in Fig. 4.6 (a) would exhibit a negative polarity VIQ signal followed by a positive polarity VIQ signal.

Figure 4.7 shows an energy band diagram possessing negative bulk space charge. This profile initially yields a negative polarity VIQ signal, due to hole transport, when illuminated from the ITO side followed by a positive polarity VIQ signal, due to transport of photo-injected electrons, as shown in Fig. 4.7 (b). The energy band diagrams shown in Figs. 4.7 (a) and (b) would exhibit a positive polarity VIQ followed by a negative polarity VIQ when illuminated from the Al side.

The energy band diagrams shown in Figs. 4.4-4.7 represent the simplest possible cases of trapped charge distribution. Actual charge distributions in ACTFEL devices investigated are likely to be somewhat more complicated than the generic energy band diagrams shown, as discussed in Sections 4.5.1-4.5.6.

4.4.2 Magnitude of VIQ Peak

The maximum magnitude of the VIQ peak is believed to be related to the density of traps in the phosphor. The VIQ trap density, N_{VIQ}, may be estimated using the simple relation

$$N_{VIQ} = \frac{Q_{VIQ}}{qA}, \tag{4.1}$$

where Q_{VIQ} is the measured VIQ charge, q is the elementary charge, and A is the ACTFEL device cross-sectional area. Q_{VIQ} is evaluated as

$$Q_{VIQ} = C_s V_{VIQ}^{peak}, \tag{4.2}$$

where C_s is the sense capacitor capacitance (100 nF) and V_{VIQ}^{peak} is the maximum magnitude of the VIQ voltage developed across the sense capacitor. Finally, the VIQ trap density may be estimated as

$$N_{VIQ} = \frac{C_s V_{VIQ}^{peak}}{qA}. \tag{4.3}$$

Note that the units of N_{VIQ} are number of traps/cm^2. If the VIQ trap density is assumed to be uniform across the phosphor layer (usually a poor assumption), the number of traps per unit volume may be assessed by dividing N_{VIQ} by the phosphor thickness, d_p.

4.4.3 VIQ Peak Voltage

The applied voltage at which the VIQ signal is a maximum corresponds to the onset of the pre-threshold glow (i.e. the voltage at which light is detectable to the naked eye). It is likely that this peak arises from a competition of the unidirectional VIQ charge with the bidirectional flow of pre-threshold conduction charge, as discussed in Section 4.3 (iii). One of the merits of the VIQ method is the precision with which the onset of the pre-threshold glow may be monitored.

4.4.4 The VIQ Threshold Voltage

At voltages below V_{th}^{VIQ}, no photo-generated current transferred charge is measured during the light pulse following the application of bipolar voltage pulses. At V_{th}^{VIQ}, a measurable photo-generated transferred charge is first detected, leading to the conclusion that at this applied voltage, traps are beginning to ionize. The external applied voltage necessary to initiate VIQ trap ionization may be converted to an internal phosphor field, denoted F_{th}^{VIQ}, via

$$F_{th}^{VIQ} = \frac{C_i V_{th}^{VIQ}}{d_p(C_i + C_p)}, \tag{4.4}$$

where C_i and C_p are the insulator and phosphor capacitances, respectively, and d_p is the thickness of the phosphor layer. F_{th}^{VIQ} is employed later in this subsection to

estimate the trap depth. The VIQ threshold voltage, V_{th}^{VIQ}, is related to the depth of the traps giving rise to the VIQ signal. In the remainder of this subsection, the current density associated with the minimum sensitivity of the VIQ measurement apparatus is equated to a calculated current density in order to estimate the energy depth of the trap responsible for VIQ.

Determination of the minimum sensitivity of the VIQ apparatus can be used to estimate the energy depth of the trap responsible for the VIQ signal. In a VIQ experiment, the voltage induced across a sense capacitor in series with the ACTFEL device during the application of a xenon lamp light pulse is measured. Since the voltage induced on the sense capacitor is due to the flow of photo-generated carriers (i.e. a photo-induced current), the voltage induced on the sense capacitor can be equated to a current density. The minimum detectable voltage, V_{min}, on the sense capacitor can be equated to a minimum measurable current density, denoted J_{VIQ}^{min}, via

$$J_{VIQ}^{min} = \frac{C_s V_{min}}{t_{min} A}, \tag{4.5}$$

where t_{min} is the minimum time measurable during a VIQ voltage transient ($\sim$1.0 ms) and A is the cross-sectional area of the ACTFEL device (0.085 cm^2). Since C_s = 100 nF and $V_{min} = \sim$1 mV, $J_{VIQ}^{min} = \sim 1 \mu A/cm^2$. Note that VIQ trap depth estimates do not depend strongly on J_{VIQ}^{min} so that the accuracy of this estimate is considered adequate.

Assuming that the photo-induced current is associated with the filling of traps which were ionized by the bipolar voltage pulses, J_{VIQ}^{min} may be directly related to the emission of traps during the bipolar voltage pulses. The total ionization charge generated during the electrical pulses is the product of the number of traps ionized multiplied by the emission rate of the traps responsible for VIQ. Thus, J_{VIQ}^{min} can be equated to the total number of traps responsible for the VIQ signal multiplied by the emission rate of each trap. However, note that the voltage measured on the sense capacitor during VIQ corresponds to an external voltage. The external voltage is the voltage dropped across the entire ACTFEL device, while the internal voltage is the actual voltage dropped across the phosphor. In order to equate J_{VIQ}^{min} to the emission

rate, e_n, the internal voltage must be used to calculate the average internal field in the phosphor. This leads to the following equation relating J_{VIQ}^{min} to the emission rate and the number of traps,

$$J_{VIQ}^{min} = (\frac{C_i}{C_i + C_p}) q e_n N_{VIQ}. \tag{4.6}$$

In order to use Eqn. 4.6, an expression for the trap emission rate, e_n, must be developed. The total emission rate, e_n, is due to the sum of thermal emission, ${e_n}^{thermal}$, pure tunneling, ${e_n}^{PT}$, and phonon-assisted tunneling, ${e_n}^{PAT}$ [26]. The following equations are used to obtain e_n as a function of the phosphor field for a given trap depth and trap capture cross-section.

$$e_n(F_{th}^{VIQ}) = e_n^{PT} + e_n^{thermal} + e_n^{PAT}, \tag{4.7}$$

where

$$e_n^{PT}(F_{th}^{VIQ}) = \frac{qF_{th}^{VIQ}}{4(2m^* E_{it})^{1/2}} exp\left[\left(-\frac{4}{3}\frac{(2m^*)^{1/2}E_{it}^{3/2}}{q\hbar F_{th}^{VIQ}}\right)\left(1-\left(\frac{\Delta E_{it}}{E_{it}}\right)^{5/3}\right)\right], \tag{4.8}$$

$$e_n^{thermal}(F_{th}^{VIQ}) = \sigma v_{th} N_c exp\left(-\frac{E_{it}-\Delta E_{it}}{kT}\right), \tag{4.9}$$

$$\begin{aligned} e_n^{PAT}(F_{th}^{VIQ}) &= e_n^{thermal}\int_{\Delta E_{it}/kT}^{E_{it}/kT} exp\left[z - z^{3/2}\left(\frac{4}{3}\frac{(2m^*)^{1/2}(kT)^{3/2}}{q\hbar F_{th}^{VIQ}}\right)\times\cdots\right. \\ &\left.\times\left(1-\left(\frac{\Delta E_{it}}{zkT}\right)^{5/3}\right)\right] dz, \end{aligned} \tag{4.10}$$

where z is the variable of integration in equation 4.10, and where Δ E_{it} is defined as

$$\Delta E_{it} = q\left(\frac{qF_{th}^{VIQ}}{\pi\epsilon_p}\right)^{1/2}. \tag{4.11}$$

In the above equations, E_{it} is the energy of the trap, and m^* is the effective mass of an electron. Values used for constants in the above equations are: the permittivity of the phosphor, $\epsilon_p = 8.3(\epsilon_o)$; the trap density, $N_{VIQ} = 10^{11}$ cm^{-2} or 10^{12} cm^{-2}, as determined in Section 4.2; the thermal capture cross section, σ, is varied as discussed below; the effective mass, $m^* = 0.18(m_o)$ [23]; the effective density of states, $N_c = 2(2\pi m^* kT/h^2)^{3/2}$ cm^{-3}; and the thermal velocity, $v_{th} = (3kT/m^*)^{1/2}$ cm/s.

The VIQ trap depth may now be estimated in the following manner. The VIQ trap density, N_{VIQ}, and the threshold field, F_{th}^{VIQ}, are established from a VIQ measurement. According to Eqn. 4.6, knowing N_{VIQ} specifies e_n. Subsequently, the trap depth, E_{it}, is determined by iteratively solving Eqns. 4.6-4.11 as a function of E_{it} until the appropriate value of E_{it} is found which yields the specified e_n. However to accomplish the iterative solution of Eqns. 4.6-4.11, F_{th}^{VIQ} and the trap capture cross-section, σ, must be known. F_{th}^{VIQ} is determined from the VIQ experiment. In contrast, σ is not known. Therefore, if this procedure is employed, pairs of E_{it} and σ may be estimated together, but there is insufficient information to obtain a unique estimate of E_{it}.

By performing VIQ measurements at different temperatures, the trap depth and capture cross-section may be uniquely determined for ACTFEL devices exhibiting 'well-behaved' VIQ trends (see Sections 4.5.1-4.5.6). Temperature-dependent VIQ measurements presented in Section 4.5.2 show that F_{th}^{VIQ} shifts as a function of temperature. Thus, with changes in temperature, J_{VIQ}^{min} occurs at a different internal phosphor field intensity. Subsequently, an iterative solution of Eqns. 4.6-4.11 is performed at the same temperatures as used in the temperature-dependent VIQ experiments in order to obtain multiple estimates of E_{it} and σ and to use the temperature-dependence of the e_n equations as a means of uniquely determining E_{it} and σ.

In practice, temperature-dependent VIQ measurements do not uniquely determine E_{it} and σ, probably due to uncertainties inherent in the VIQ experiment and theoretical analysis. However, temperature-dependent measurements do appear to specify a possible range of E_{it}'s and σ's. Thus, in Sections 4.5.2-4.5.7 in which results are presented, tables of trap depths paired with capture cross-sections are presented. The capture cross-section is varied in the iterative solution until the standard deviation of the value of trap depth between iterative solutions at different temperatures is minimized. The capture cross-sections which provide the least deviation between trap depths necessary to satisfy Eqn. 4.6 at different temperatures are considered to define the range of the most likely capture cross-section and trap energy depth.

4.5 Experimental Results

The VIQ experiment is performed using ZnS:Mn samples deposited by three different methods: thermal evaporation, atomic layer epitaxy with chlorine as a constituent of the precursor gas [ALE (Cl)], and by atomic layer epitaxy with diethyl zinc as a carrier gas [ALE (DEZ)]. The method of deposition has a strong effect on the electrical characteristics of the ACTFEL device. The VIQ results for these three different samples are discussed separately in the following subsections.

4.5.1 VIQ of Thermally Evaporated ZnS:Mn ACTFEL Devices

The first sample to be discussed is a thermally evaporated ZnS:Mn ACTFEL device. The virgin evaporated ZnS:Mn ACTFEL device tends to be electrically unstable; small regions of virgin evaporated ZnS:Mn ACTFEL devices short out, creating "burn-out spots" in which the top Al layer evaporates, leaving behind a small portion of the ACTFEL device which is open-circuited. Each time a portion of the ACTFEL device shorts out, the voltage on the sense capacitor jumps many volts. Due to this initial "burn-in" behavior, accurate VIQ measurements cannot be obtained for a virgin evaporated ZnS:Mn ACTFEL device. After aging the ACTFEL device for approximately half an hour at 40 V over threshold, the ACTFEL device becomes stable and VIQ measurements may be accurately obtained. It is noted that thermally evaporated ZnS:Mn ACTFEL devices are very sensitive to moisture. Therefore, all measurements and aging of thermally evaporated ACTFEL devices are performed under vacuum at a pressure of approximately 50 microns. All aging is performed using a bipolar trapeziodal voltage pulse whose frequency is either 1 kHz or 3 kHz, as denoted on the appropriate figure.

VIQ and C-V curves for a thermally evaporated ZnS:Mn ACTFEL device with a phosphor thickness of 950 nm are shown in Figs. 4.8-4.10. As shown in Fig. 4.8, a negative polarity VIQ peak occurs for the first few hours of operation for the evaporated ZnS:Mn ACTFEL device. The VIQ response exhibits a VIQ threshold voltage of $\sim$90 V, corresponding to a VIQ threshold field of $\sim$0.7 MV/cm which

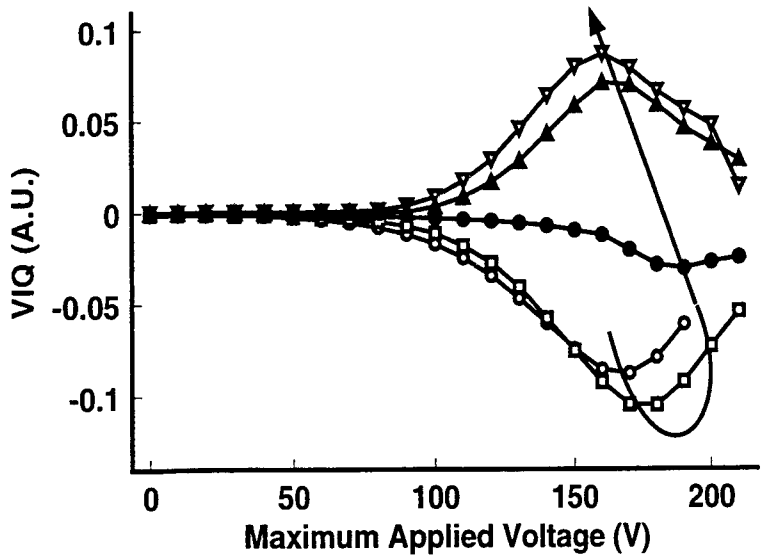

Figure 4.8. VIQ aging trend of an evaporated ZnS:Mn ACTFEL device. The five curves shown correspond to 0.5, 6, 30, 50, and 73 hours of aging at 1 kHz.

remains constant with aging. The negative VIQ peak initially increases in magnitude and then decreases in magnitude as a function of aging, with the location of the voltage peak increasing slightly. After ~40 hours of aging at 1 kHz, the VIQ polarity switches from negative to positive. Note that V_{th}^{VIQ} remains constant as the peak changes from negative to positive polarity. Also, the voltage at which the VIQ peaks gradually decreases for aging periods longer than 40 hours.

Previous work has shown that brightness-voltage (B-V) measurements of evaporated ZnS:Mn ACTFEL devices exhibit p-shift followed by n-shift aging characteristics. [27] The B-V p-shift to n-shift aging trends correlate well with VIQ measurements in which the negative polarity VIQ signal switches to a positive polarity VIQ signal for longer aging periods.

The B-V and VIQ aging results can also be correlated to the C-V aging curves shown in Figs. 4.9 and 4.10. The C-V curves show an initial positive voltage shift (p-shift) for the first ~40 hours of aging followed by a negative voltage shift (n-shift) after ~40 hours. The C-V transition from p-shift to n-shift occurs after the same aging period as the change in the VIQ polarity from negative to positive. C-V aging

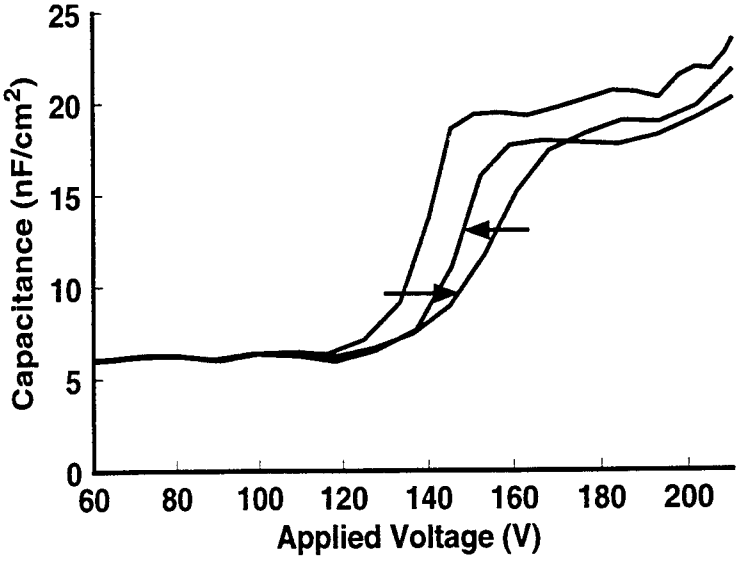

Figure 4.9. Positive polarity C-V curves of an evaporated ZnS:Mn ACTFEL device after 0.5, 30 and 73 hours aging at 1 kHz.

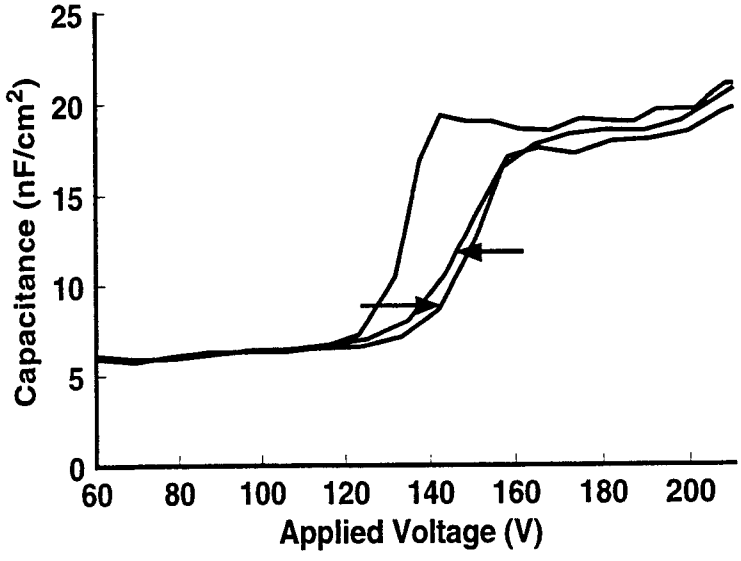

Figure 4.10. Negative polarity C-V curves of an evaporated ZnS:Mn ACTFEL device after 0.5, 30 and 73 hours aging at 1 kHz.

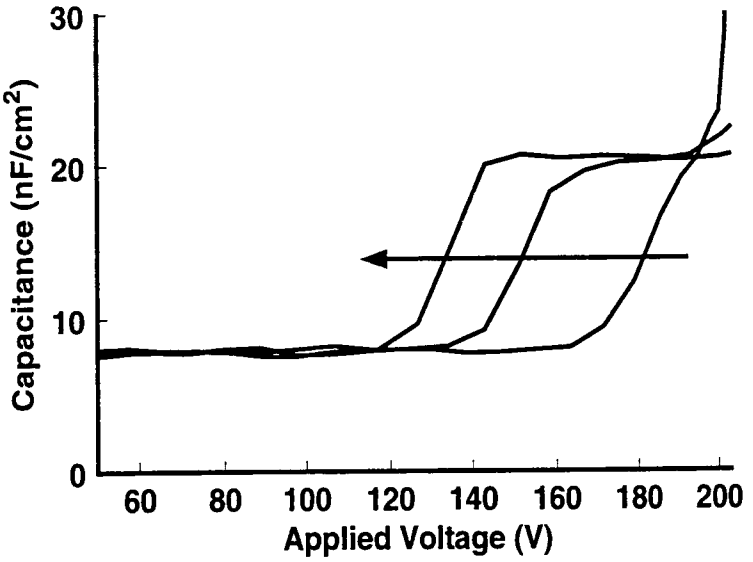

Figure 4.11. Positive polarity C-V curves of an evaporated ZnS:Mn ACTFEL device acquired after 210 hours aging at 3 kHz. Curves acquired at 20, 40, and 60 V over threshold. Arrow indicates increasing voltage.

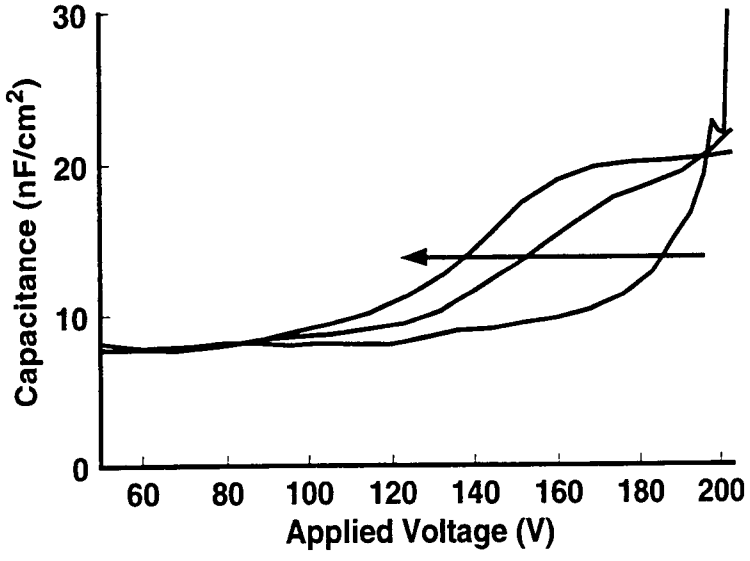

Figure 4.12. Negative polarity C-V curves of an evaporated ZnS:Mn ACTFEL device acquired after 210 hours aging at 3 kHz. Curves acquired at 20, 40, and 60 V over threshold. Arrow indicates increasing voltage.

curves taken for aging periods up to 73 hours show rigid shifting of the C-V curves. C-V curves acquired at 20, 40, and 60 V over threshold at an aging period of 210 hours show softening of the negative polarity C-V curves, and a rigid shifting of the positive C-V curves, as shown in Figs. 4.12 and 4.11, respectively. The VIQ curve acquired after 210 hours is virtually identical to that obtained after 73 hours, indicating a saturation in VIQ; thus the 210 hour data is not shown.

A rigid shift of the C-V curve is attributed to changes in fixed charge density, while softening of the C-V curve is associated with changes in the trap state distribution from which charge is sourced. The fixed charge density does not change as a function of applied field; hence, these fixed charge states are deep traps whose charge state does not change during ACTFEL device operation. [21] Thus, aging up to 73 hours is ascribed to changes in fixed charge density (since only rigid shifting of the C-V is observed), while trends at 210 hours show a change in the interface state density (since softening of the negative polarity C-V is observed) for the top (Al) interface.

The initial p-shift of the C-V curves is attributed to changes near the bottom (ITO) interface, while subsequent n-shift aging of the C-V curves is attributed to changes near the top (Al) interface, as discussed below. The negative polarity VIQ signal which is observed for the first $\sim$ 40 hours of aging is interpreted as evidence that the most shallow VIQ-active states are located near the bottom (ITO) interface; this gives rise to positive charge near the bottom interface, as shown in Fig. 4.4.

In contrast, the positive polarity VIQ signal which is observed after $\sim$40 hours of aging is attributed to localization of the most shallow VIQ-active states near the top (Al) interface, giving rise to positive charge near the top (Al) interface, as shown in Fig. 4.5. Since the C-V and B-V transition from p-shift to n-shift occurs after the same aging period as the change in the VIQ polarity from negative to positive, it is very likely that the same mechanism is responsible for both the switch in the VIQ polarity and the switch from p-shift to n-shift of the C-V and B-V trends.

Several observations suggest that the changes in trap density which result in the observed aging trends occur in the phosphor near one of the phosphor/insulator

interfaces. First, the fact that the VIQ polarity is identical for illumination from either interface is evidence that these aging processes are interfacial effects. Second, softening of the C-V curves is usually attributed to traps distributed near to an interface, but not precisely at the interface. [20]

As discussed in Section 4.4, the magnitude of the VIQ signal is related to the number of traps. In the case of evaporated samples, the decrease and subsequent switch of polarity is attributed to changes in the trap density at or near the interfaces. The initial increase in the maximum VIQ for the first 6 hours of aging is attributed to generation of more traps near the bottom (ITO) interface; the rigid C-V shift and the movement of the VIQ peak to larger voltage suggests that these are deep traps. Aging for periods longer than 6 hours causes generation of traps near the top (Al) interface, resulting in a reduction of the VIQ maximum, and finally leading to a switch in the VIQ polarity.

The VIQ trap density for an evaporated ZnS:Mn ACTFEL device can be estimated from Fig. 4.8 using Eqn. 4.3. The maximum VIQ signal shown in Fig 1.8 is 0.11 V, which corresponds to $\sim 10^{11}$ traps/cm^2. Assuming the traps responsible for VIQ are all within $\sim$100 nm of the interface, this corresponds to a trap density of $\sim 10^{16}$ traps/cm^3. As mentioned in Section 4.2, due to the RC time constant of the measurement system, this is probably a lower estimate of the VIQ trap density.

Note that V_{th}^{VIQ} is constant for the entire duration of this aging experiment, even though the VIQ polarity reverses. This implies that the most shallow VIQ states are identical for both the bottom (ITO) interface (where short-term aging occurs) and the top (Al) interface (where long-term aging occurs). The VIQ polarity reverses when the density of these VIQ traps near the top (Al) interface increases to a density larger than that present at the bottom (ITO) interface. Even though the V_{th}^{VIQ} is constant for the entire aging duration, this does not mean that the same kind of trap is responsible for short and long-term aging since the short-term aging is associated with a deep level, fixed charge state which is not related to V_{th}^{VIQ}.

The VIQ threshold field occurs at $\sim$0.7 MV/cm. Use of Eqns. 4.6-4.11, and assuming a trap density of 10^{11} cm^{-2}, yields the trap depth/capture cross-section

Table 1. Capture cross-section/trap depth combinations which yield threshold emission rate.

Capture cross-section (σ)	Trap Depth
10^{-12} cm^2	1.19 eV
10^{-13} cm^2	1.12 eV
10^{-14} cm^2	1.07 eV
10^{-15} cm^2	1.01 eV

pairs shown in Table 1. Better estimates of the trap depth and capture cross-section are obtained from temperature-dependent VIQ measurements, as discussed in Subsection 4.5.2.

One of the puzzling aspects of this evaporated ZnS:Mn ACTFEL device aging study is that for aging times between 73 and 210 hours the VIQ signal and the positive polarity C-V curves saturate, whereas the negative polarity C-V curves exhibit continued softening. Why saturation occurs for two of these measured aging trends while the other trend exhibits continued softening is unclear. The observed saturation in VIQ is especially puzzling since it is thought that the VIQ measurement is sensitive to changes in trap density across the entire phosphor. Thus, any changes in C-V curves are expected to be reflected in VIQ trends. Tentatively, this apparent discrepancy is attributed to the temporal character of the VIQ signal, as follows.

An idealized VIQ transient is illustrated in Fig. 4.13. Note that, as discussed previously, VIQ is taken to be the peak value of the sense capacitor transient, $v_{cs}(t)$. However, also note from Fig. 4.13 that there is always a tail in the v_{cs} transient and that the intensity of this tail may change even when VIQ is relatively constant. Moreover, it is observed that the time at which the v_{cs} transient maximizes, denoted as t_{peak} in Fig. 4.13, is not constant during aging. Thus, it is proposed that the puzzling aging trends discussed above may be associated with the more complex nature of the v_{cs} transient than what is assessed in the simple VIQ experiment.

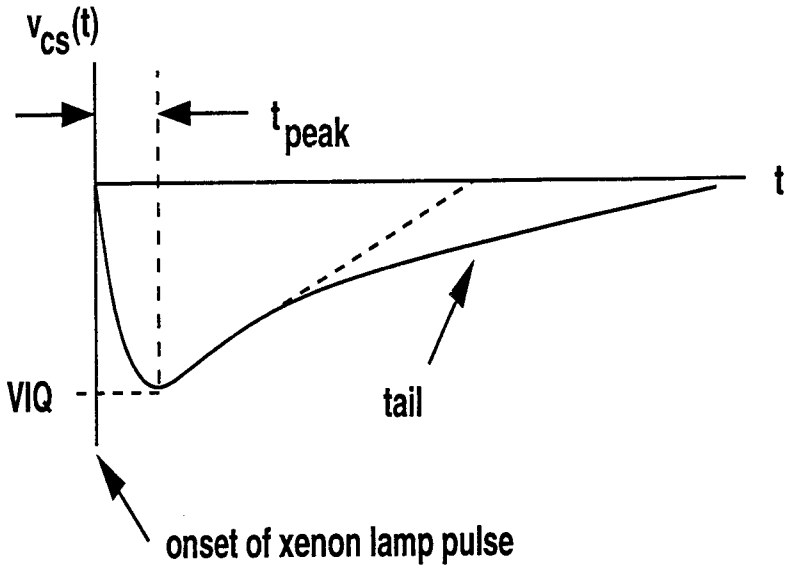

Figure 4.13. An idealized VIQ transient curve illustrating a tail which may change as a function of aging and yet not affect the measured VIQ signal magnitude. v_{cs} is the voltage measured across a sense capacitor in series with the ACTFEL device.

4.5.2 Temperature Dependence of VIQ for Evaporated ZnS:Mn ACTFEL Devices

The temperature-dependent VIQ experiment is accomplished by obtaining VIQ curves at five different temperatures (20, 200, 300, 373, and 423 K) using an evaporated ZnS:Mn ACTFEL device, as shown in Fig. 4.14. This data shows a monotonic shift of the VIQ peak and the VIQ threshold field to smaller values with increasing temperature. Additionally, the VIQ curves broaden significantly with increasing temperature. For evaporated ZnS:Mn ACTFEL devices, the onset of the pre-threshold glow is found to occur at the VIQ peak for each temperature. Thus, the onset voltage of the pre-threshold glow decreases with increasing temperature. Finally, the EL threshold voltage, V_{th}^{EL}, is relatively independent of temperature.

Four of the temperature-dependent trends evident from Fig. 4.14 (i.e. the decrease in the VIQ threshold, broadening of the VIQ peak, VIQ peak voltage, and the onset of pre-threshold glow decreasing with increasing temperature) suggest that the VIQ and the pre-threshold glow involve physical mechanisms that are thermally activated. Most likely, this thermally activated process is associated

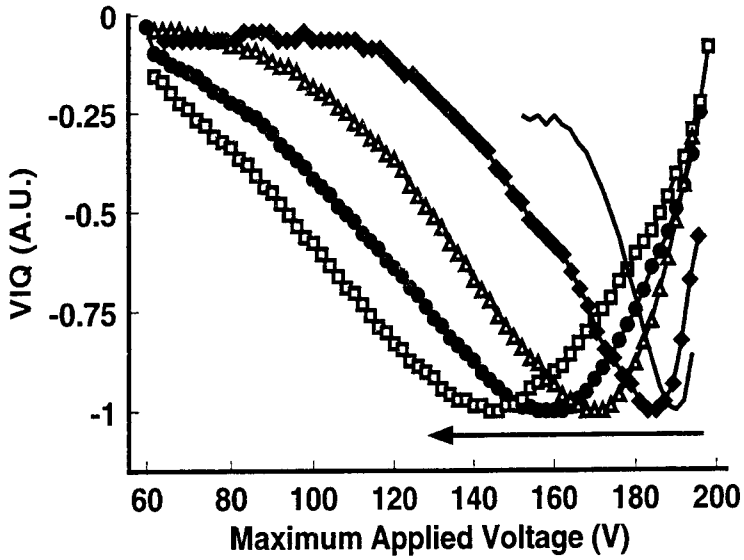

Figure 4.14. Temperature dependent VIQ curves for an evaporated ZnS:Mn ACTFEL Device. Curves are acquired at 20, 200, 300, 373, and 423 K. The arrow indicates increasing temperature.

with phonon-assisted tunneling or thermionic emission of electrons from trap states to the conduction band. Note that pure tunnel emission alone cannot account for these VIQ and pre-threshold glow trends since pure tunnel emission is known to be temperature-independent. In contrast, since V_{th}^{EL} is determined to be relatively temperature-independent, this indicates that pure tunnel emission is the dominant physical process responsible for establishing the EL threshold, in agreement with conclusions of previous researchers. [28]

The thermally-activated nature of the pre-threshold glow leads to the conclusion that it is an injection-limited process, rather than a transport-limited process. The justification for this assertion is as follows. Note that it is observed that the spectrum of the pre-threshold glow is identical to the spectrum of normal ACTFEL operation. This leads to the conclusion that pre-threshold glow is due to impact excitation of Mn luminescent centers. This impact excitation is most likely caused by the transferred charge which is generated by ionization of the traps responsible for VIQ. When the electrons emitted from the traps become hot enough to impact excite Mn lumi-

Table 2. Temperature dependence of the VIQ threshold field and corresponding simulated trap depth assuming a capture cross-section of 10^{-14} cm^2.

T(K)	F_{th}^{VIQ} (MV/cm)	E_t (eV)
20	1.16	1.11
200	0.88	1.15
300	0.69	1.07
373	0.46	1.09
423	0.36	1.12
Mean	N.A.	1.11
St.Dev.	N.A.	0.03

nescent centers, a faint glow is observed. If the onset voltage of pre-threshold glow were to increase with increasing temperature, then the pre-threshold glow would be attributed to an increase in phonon scattering resulting in a decrease in the transport efficiency. However, since the onset voltage of the pre-threshold glow decreases with increasing temperature, the mechanism for this shift cannot be attributed to phonon scattering, but must be ascribed to a thermally-activated process.

One of the primary motivations for performing temperature-dependent VIQ experiments is to obtain a better estimate of the trap depth and capture cross-section of the VIQ traps. This is accomplished as follows. First, for a given capture cross-section, the computer simulation discussed in Subsection 4.4.4 is performed to estimate the trap depth at the five different measurement temperatures. For example, Table 2 summarizes the estimated trap depths for each measurement temperature when the capture cross-section is assumed to be 10^{-14} cm^2. Next, for each capture cross-section, the mean trap depth and its standard deviation are compared, as shown in Table 3, and the trap depth/capture cross-section pairs which have the minimal trap depth standard deviation are considered to be the best-fit. This analysis suggests that the trap responsible for VIQ in evaporated ZnS:Mn ACTFEL devices

Table 3. Simulated capture cross-section/trap depth pairs. The mean and standard deviation shown for trap depths are obtained by performing simulations at different temperatures.

σ (cm^2)	E_t [mean] (eV)
10^{-11}	1.27 ± 0.10
10^{-12}	1.22 ± 0.07
10^{-13}	1.16 ± 0.04
10^{-14}	1.11 ± 0.03
10^{-15}	1.05 ± 0.05
10^{-16}	1.00 ± 0.08

is characterized by an energy depth of ~1.0-1.2 eV and a capture cross-section of ~10^{-13}-10^{-15} cm^2. A capture cross-section value of ~10^{-13}-10^{-15} cm^2 corresponds to a neutral to coulombically repulsive trap. [25]

4.5.3 VIQ Summary for Evaporated ZnS:Mn ACTFEL Devices

A summary of the aging trends observed in ZnS:Mn ACTFEL devices is given in Fig. 4.15. Short-term aging (i.e. 0-40 hours at 1 kHz) is characterized by a p-shift in the B-V and C-V curves and negative polarity VIQ curves. Short-term aging appears to be associated with changes in the physical properties of the phosphor near the bottom (ITO) interface, as evident from the VIQ polarity. Long-term aging (i.e. greater than 40 hours at 1 kHz) is characterized by an n-shift in the B-V and C-V curves and positive polarity VIQ curves. Long-term aging seems to be correlated with changes in the physical properties of the phosphor near the top (Al) interface, as evident from softening of the negative polarity C-V curves and the VIQ polarity. Furthermore, the temperature dependence of the V_{th}^{VIQ} leads to estimates of the VIQ trap energy depth and capture cross-section of ~1.0-1.2 eV and ~10^{-13}-10^{-15} cm^2, respectively. Additionally, the VIQ trap density is estimated to be ~10^{16} cm^{-3}.

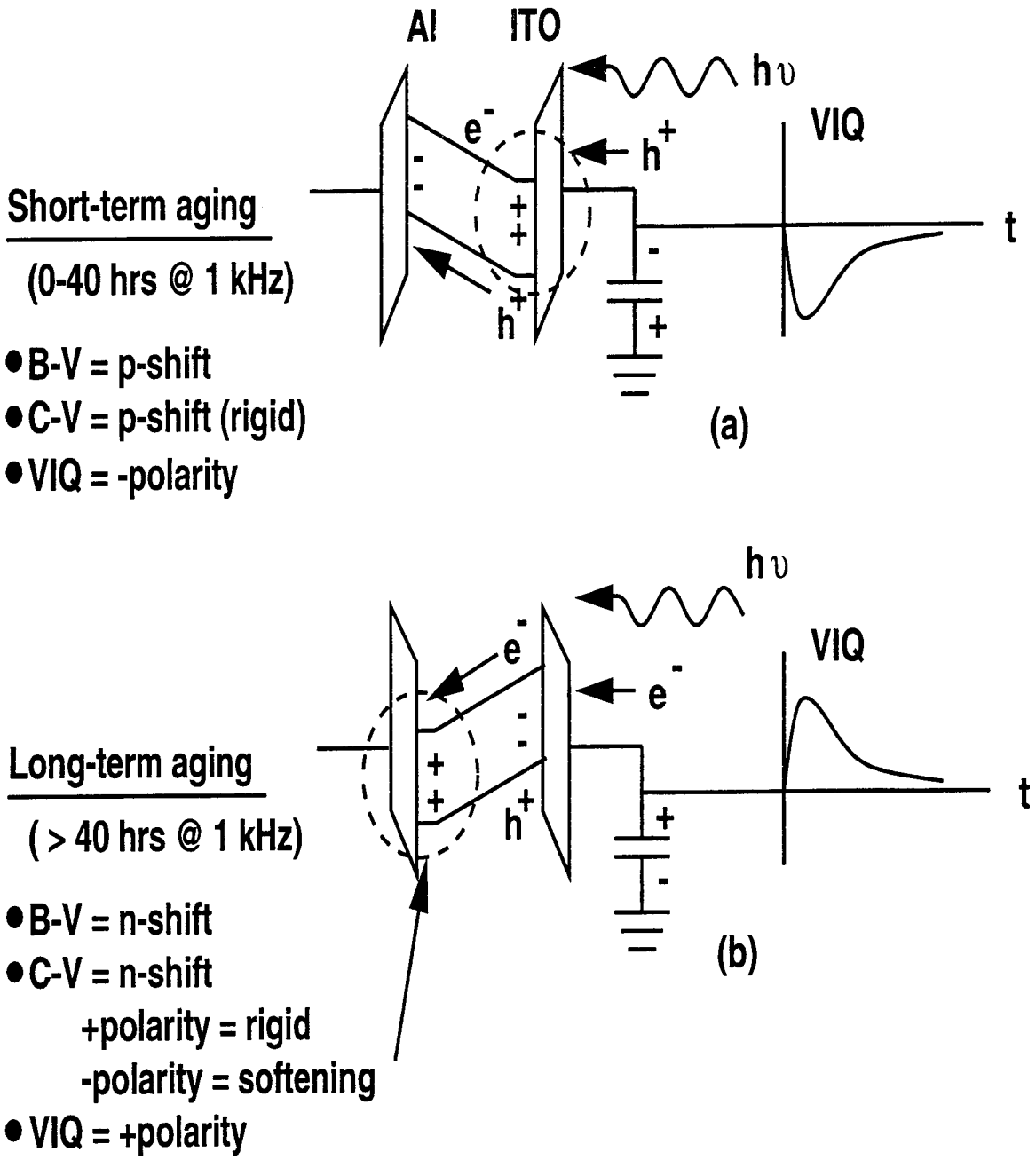

Figure 4.15. Summary of evaporated ZnS:Mn aging trends. The dashed circles indicate the interface where aging is believed to occur.

Speculation regarding the physical nature of the traps responsible for the aging of evaporated ZnS:Mn ACTFEL devices is postponed until Section 4.6.

Two other important results of this subsection should be highlighted. First, the temperature-independence of the EL threshold is supportive evidence that the EL threshold is dominated by tunnel injection from interface states. Second, the decrease in the onset voltage of the pre-threshold glow with increasing temperature, and the fact that the spectrum of the pre-threshold glow is consistent with Mn radiative recombination, establishes that evaporated ZnS:Mn ACTFEL devices are injection-limited, not transport-limited.

4.5.4 VIQ aging of an Atomic Layer Epitaxy (Cl) ZnS:Mn ACTFEL Device

VIQ aging curves for an ALE (Cl) ZnS:Mn ACTFEL device are shown in Fig. 4.16. Corresponding C-V aging curves are shown for positive and negative voltage polarities in Figs. 4.17 and 4.18, respectively. The unaged ALE (Cl) samples posess a single small negative VIQ peak but develop two negative peaks with aging. A negative polarity VIQ signal is consistent with the energy band diagram shown in Fig. 4.5, in which the most shallow VIQ trap states are present at or near the bottom (ITO) interface. The lower voltage peak, Peak 1, becomes larger with aging and the peak remains at the same voltage. Note that the trap responsible for Peak 1 must be very shallow since $V_{th}^{VIQ} = 0$ V for this VIQ feature. The higher voltage peak, Peak 2, becomes larger and the peak shifts to a lower voltage with aging. Peak 2 is attributed to a deeper trap. VIQ aging does not appear to stabilize, although the growth of both VIQ peaks changes more slowly after the ACTFEL device has been aged for a long time. For long-term aging (not shown) Peak 1 saturates, but Peak 2 continues to grow slightly in magnitude and to decrease in peak voltage.

The C-V curves show asymmetrical aging characteristics. The positive polarity C-V curve shows extreme softening with aging, as shown in Fig. 4.17. The negative polarity C-V curve exhibits a reduction in C-V overshoot and a broadening of the C-V overshoot peak with aging, as shown in Fig. 4.18. Additionally, the negative polarity

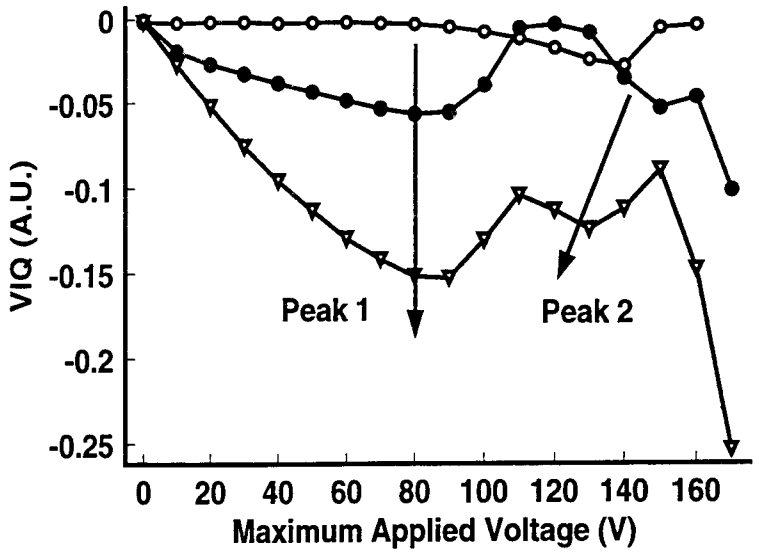

Figure 4.16. VIQ aging trend for an ALE (Cl) ZnS:Mn ACTFEL device. Aging is for 0, 4, and 87 hours aging at 3 kHz, with arrows indicating increasing aging time.

C-V curves undergo a rigid n-shift with aging. The increase in the magnitude of Peak 1 in the VIQ aging curves and the softening of the positive polarity C-V curves are attributed to the generation of shallow traps at the bottom (ITO) interface. As discussed in Subsection 4.5.5, Peak 1 appears to be associated with Cl. The physical nature of Peak 2 is less clear and is discussed more fully in Section 4.6. Finally, note that C-V overshoot and the abrupt C-V transition observed in the negative polarity C-V curves shown in Fig. 4.18 are evidence for dynamic space charge creation occuring near the top (Al) interface. Previously, these C-V trends (overshoot and an abrupt C-V transition) have been attributed to impact ionization of Zn vacancies present near the top (Al) interface. [20, 29]

Using Eqn. 4.3, the maximum magnitude of the peak VIQ of 0.15 V corresponds to $\sim 10^{12}$ traps/cm^2. Assuming the traps responsible for VIQ are within $\sim$100 nm of the interface, this corresponds to $\sim 10^{17}$ traps/cm^3. This is an order of magnitude larger than the estimated trap density for an evaporated ZnS:Mn ACTFEL device. As stated in Section 4.2, this is a lower estimate of the trap density due to the RC time constant of the system.

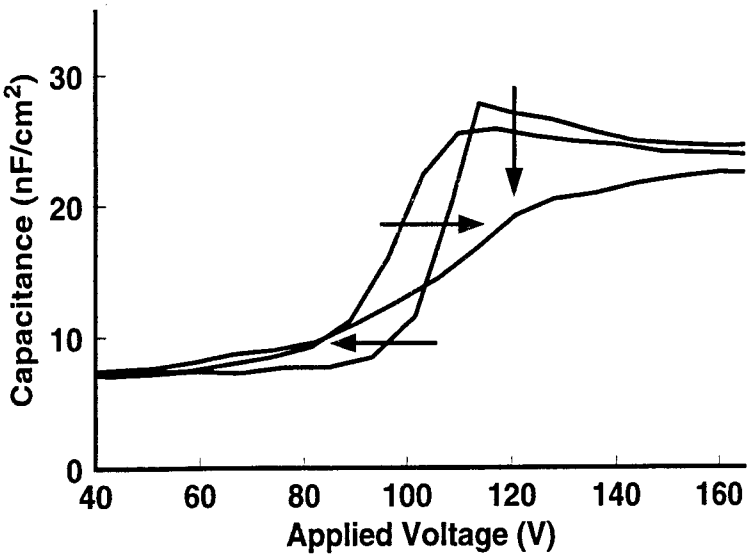

Figure 4.17. Positive polarity C-V curves for an ALE (Cl) ZnS:Mn ACTFEL device at 0, 4, and 87 hours of aging at 3 kHz, with arrows indicating increasing aging time.

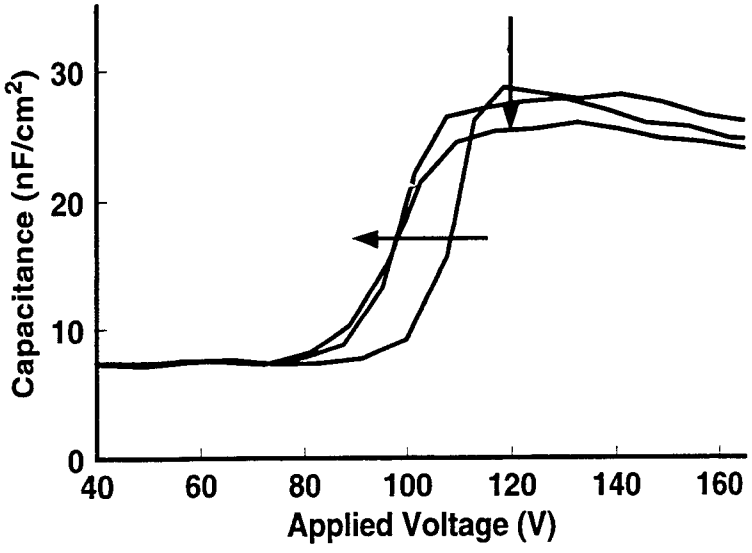

Figure 4.18. Negative polarity C-V curves of ALE (Cl) ZnS:Mn ACTFEL device at 0, 4, and 87 hours of aging at 3 kHz, with arrows indicating increasing aging time.

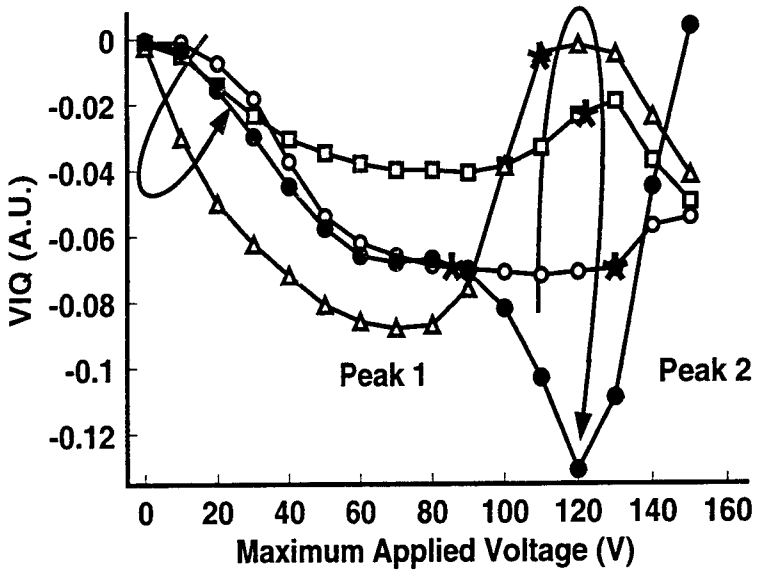

Figure 4.19. Temperature dependent VIQ curves for an ALE (Cl) ZnS:Mn ACTFEL device. Curves are acquired at 20, 150, 300, and 450 K. The arrows indicate increasing temperature. The asterisks indicate the voltage onset of the pre-threshold glow.

4.5.5 Temperature Dependence of VIQ for an ALE (Cl) ZnS:Mn ACTFEL Device

The temperature dependence of VIQ for an ALE (Cl) ZnS:Mn ACTFEL device is shown in Fig. 4.19. Figure 4.19 shows that Peak 1 is not strongly affected by changes in temperature. At 20 K, a V_{th}^{VIQ} of 10 V is observed, whereas $V_{th}^{VIQ} = 0$ V for all other temperatures measured. The magnitude of Peak 2 initially decreases with temperature and then increases dramatically at 450 K.

The most important feature of the temperature dependence of VIQ for an ALE (Cl) ZnS:Mn ACTFEL device is that the non-zero V_{th}^{VIQ} at 20 K allows the trap depth of Peak 1 to be estimated. At a temperature this low, the emission rate of the trap responsible for VIQ depends only on pure tunneling. Thus, performing the simulation described in Section 4.4.4 and assuming that the emission occurs exclusively by pure tunneling yields an estimated trap depth of 0.27 eV. Previous work has established the energy depth of Cl in ZnS by means of thermoluminescence to be from 0.2 to 0.3 eV. [3, 4, 5] Thus, it is very likely that Peak 1 of the VIQ

for the ALE (Cl) ZnS:Mn ACTFEL device measured is due to Cl. A V_{th}^{VIQ} and a corresponding trap depth for the Peak 2 cannot be established due to the presence of the first peak. However, Peak 2 obviously arises from a deeper trap than that associated with Peak 1.

The voltage onset of the pre-threshold glow is indicated by asterisks in Fig. 4.19. Note that the voltage onset of the pre-threshold glow decreases monotonically with increasing temperature (i.e. 130, 125, 110, and 85 V for 20, 150, 300, and 450 K, respectively). Thus the onset of pre-threshold glow is seen to occur at lower voltages for higher temperatures. As stated in Section 4.5.1, this trend leads to the conclusion that the onset of pre-threshold glow in ALE (Cl) ZnS:Mn ACTFEL devices is due to an injection-limited process rather than a transport-limited process.

It is unclear why the pre-threshold glow does not occur at the VIQ voltage peak as is the case for the evaporated ZnS:Mn ACTFEL devices studied. In the case of ALE (Cl) ZnS:Mn ACTFEL devices, the onset of the pre-threshold glow occurs near a discontinuity in the slope of the VIQ curve at each temperature (see Fig. 4.19, but does not appear to correspond to any consistent feature of the curve (i.e. always at the peak, always at the upward turning point, etc.). It is speculated that this lack of a consistent pattern in the pre-threshold glow is a consequence of the more complex nature of the aging of ALE (Cl) ZnS:Mn ACTFEL devices.

4.5.6 VIQ of an Atomic Later Epitaxy (DEZ) ZnS:Mn ACTFEL Device

The VIQ curves of an ALE (DEZ) ZnS:Mn ACTFEL device are shown in Fig. 4.20. Corresponding positive and negative polarity C-V curves are shown in Figs. 4.21 and 4.22, respectively. Previous work has shown that the electrical (Q-V, C-V, Q-F_p) and optical (B-V) characteristics of ALE (DEZ) ACTFEL devices do not change significantly with aging compared to ALE (Cl) ZnS:Mn ACTFEL devices. [20, 17] The VIQ curves for ALE (DEZ) ZnS:Mn ACTFEL devices show a single positive polarity VIQ peak which initally increases in magnitude and then decreases in magnitude.

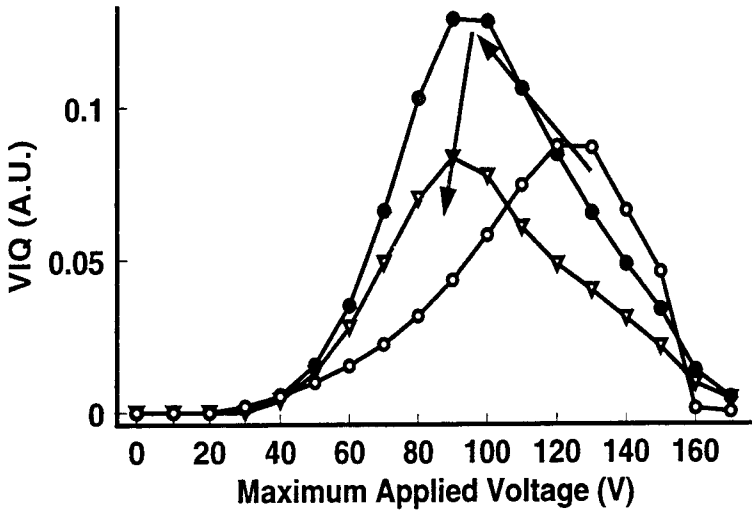

Figure 4.20. VIQ aging trend for an ALE (DEZ) ZnS:Mn ACTFEL device. Aging is for 0, 0.6, and 40 hours at 3 kHz, with arrows indicating increasing aging time.

A positive polarity VIQ curve is consistent with the energy band diagram shown in Fig. 4.4 in which the most shallow VIQ traps are present at or near the top (Al) interface. The initial increase in the VIQ magnitude is likely due to an increase in the number of traps responsible for VIQ near the top (Al) interface. The subsequent decrease in VIQ magnitude and concomitant shift in the peak to a lower voltage after 4 hours of aging is possibly due to generation of traps at the bottom (ITO) interface. Further evidence for the presence of a VIQ trap at the bottom (ITO) interface is presented in Subsection 4.5.7.

Both positive and negative polarity capacitance-voltage curves show a p-shift with aging, as seen in Figs. 4.21 and 4.22. Note that the positive polarity C-V curve possesses a steeper C-V transition region (implying an abrupt interface state density or electron multiplication), whereas the negative polarity C-V curve is soft (i.e. has a rather washed out turn-on) and the C-V transition is gradual (consistent with a non-abrupt density of states or, more likely, phosphor traps which are distributed within the phosphor near the top (Al) interface instead of being located precisely at the interface).

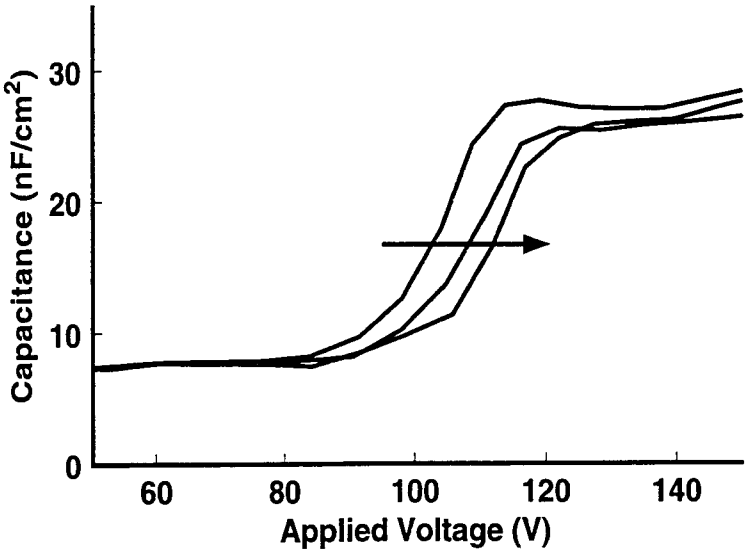

Figure 4.21. Positive polarity C-V curves for an ALE (DEZ) ZnS:Mn ACTFEL device at 0, 0.6, and 40 hours of aging at 3 kHz, with arrows indicating increasing aging time.

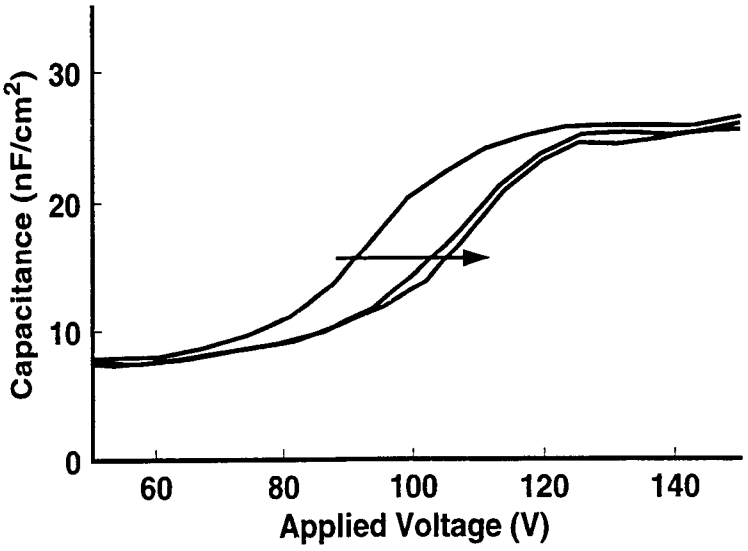

Figure 4.22. Negative polarity C-V curves for an ALE (DEZ) ZnS:Mn ACTFEL device at 0, 0.6, and 40 hours of aging at 3 kHz, with arrows indicating increasing aging time.

In this ACTFEL device, the VIQ threshold field is ~0.3 MV/cm., which using Eqns. 4.6-4.11 and assuming a capture cross-section of 10^{-15} cm^2 (see Subsection 4.5.7) leads to an estimated trap depth of ~0.8 eV. The maximum VIQ signal in Fig. 4.20 of ~0.15 V leads to an estimated trap density of $\sim 10^{12}$ traps/cm^2. Assuming the traps responsible for VIQ are all within ~100 nm of the interface, this corresponds to $\sim 10^{17}$ traps/cm^3. This is equal to the estimated trap density for an ALE (Cl) ZnS:Mn ACTFEL device.

4.5.7 Temperature Dependence of VIQ for an ALE (DEZ) ACTFEL Device

The temperature dependence of VIQ for an ALE (DEZ) ZnS:Mn ACTFEL device is investigated by performing VIQ measurements at 173, 300, 375, and 450 K, as shown in Fig. 4.23. The temperature-dependent VIQ curves initially shift to a lower voltage with increasing temperature, then decrease in magnitude significantly at 375 K, and finally switch polarity with a concomitant decrease in the voltage at which the VIQ signal peaks. V_{th}^{VIQ} occurs at ~60 V at a temperature of 173 K, and at ~30 V at a temperature of 300K. A V_{th}^{VIQ} is not observed at 375 or 450 K.

As shown in Fig. 4.23, the onset of pre-threshold glow occurs at ~100 V for temperatures of 173, 300, and 375 K, but occurs at 70 V for 450 K. (The onset of pre-threshold glow is denoted by asterisks in Fig. 4.23.) The fact that the onset voltage of the pre-threshold glow does not significantly shift with temperature until above 375 K means that nothing can be determined with regard to whether the pre-threshold glow is transport or injection-limited. This temperature independence is in contrast to the trends found for evaporated and ALE (Cl) ZnS:Mn ACTFEL devices, whose pre-threshold glow characteristics are established to be injection-limited.

The VIQ curves acquired at 173 and 300 K are "well-behaved" in that a distinct V_{th}^{VIQ} is observed and the pre-threshold glow occurs at or very near the VIQ peak. However, the VIQ curve acquired at 375 K shows a drastic decrease in magnitude, and the VIQ curve acquired at 450 K switches to a negative polarity. This positive-to-negative switch in VIQ polarity with increasing temperature is ascribed to VIQ

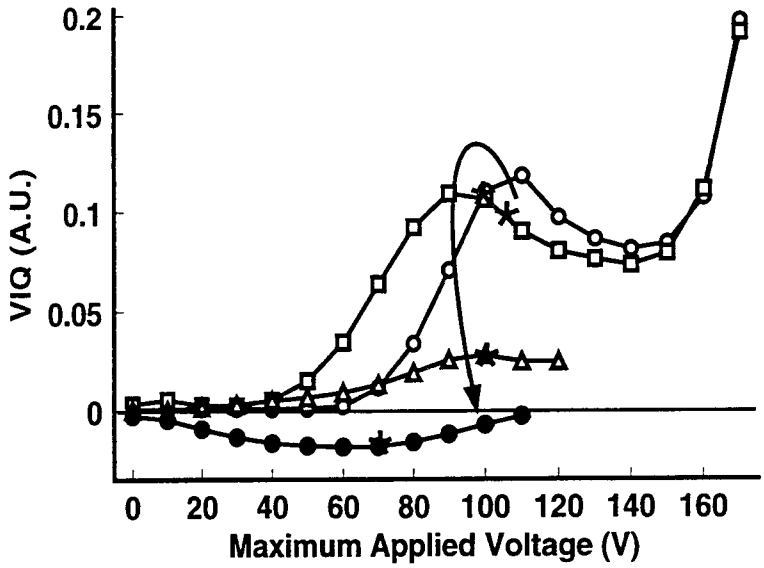

Figure 4.23. Temperature dependent VIQ curves for an ALE (DEZ) ZnS:Mn ACTFEL device. Curves are acquired at 173, 300, 375, and 450 K. The arrow indicates increasing temperature. The asterisks indicate the voltage onset of the pre-threshold glow.

trap emission from opposite interfaces. The low temperature positive polarity VIQ curves are attributed to VIQ traps near the top (Al) interface. In contrast, the high temperature, negative polarity VIQ curves are believed to arise from VIQ traps near the bottom (ITO) interface. Presumably, the role of temperature is to establish the energy depth of the traps which determine the polarity of the measured VIQ signal. The fact that a reversal of the VIQ polarity is observed for this ALE (DEZ) ACTFEL device suggests that there is an interfacial asymmetry in the VIQ trap densities as a function of trap depth.

A temperature dependent simulation of the trap depth/capture cross-section pairs is performed using the two VIQ data sets obtained at 173 and 300 K. The simulations are performed as described in Subsection 4.4.4 and the results are summarized in Table 4. The temperature-dependent VIQ results for an ALE (DEZ) ACTFEL device suggest that the trap depth is in the range of ~0.7-0.8 eV with a capture cross-section of $\sim 10^{-14}$-10^{-16} cm^2. This corresponds to a coulombically neutral trap. [25] The physical nature of this trap is discussed in Section 4.6

Table 4. Simulated capture cross-section/trap depth pairs for an ALE (DEZ) ACTFEL Device.

σ (cm^2)	E_t (300 K) (eV)	E_t (173 K) (eV)
10^{-11}	1.01	0.92
10^{-12}	0.95	0.88
10^{-13}	0.89	0.85
10^{-14}	0.83	0.81
10^{-15}	0.78	0.78
10^{-16}	0.71	0.74
10^{-17}	0.64	0.71

4.6 VIQ Summary

VIQ aging experiments provide information about the traps giving rise to aging. The VIQ polarity is related to the location of these traps within the phosphor. The VIQ peak magnitude is proportional to the total number of VIQ traps in the phosphor. The VIQ threshold field allows an estimate of the trap depth to be obtained. Three traps are determined from the VIQ method at energy depths of ~1.1, 0.8, and 0.3 eV for evaporated, ALE (DEZ), and ALE (Cl) ZnS:Mn ACTFEL devices, respectively.

A summary of the VIQ and C-V aging trends for the three types of ZnS:Mn ACTFEL devices investigated in this thesis are presented in Table 5. From Table 5 it is found that the VIQ polarity of the evaporated ZnS:Mn ACTFEL device investigated switches with aging, while the ALE (Cl) and ALE (DEZ) ZnS:Mn ACTFEL devices investigated possess the same VIQ polarity throughout the aging process. The switch in the polarity of the evaporated sample is attributed to the assumption that short-term aging is due to changes at the bottom (ITO) interface, while long-term aging is due to changes at the top (Al) interface. Conversely, all aging in

Table 5. Summary of VIQ aging trends for evaporated, ALE (Cl), and ALE (DEZ) ZnS:Mn ACTFEL devices.

	Evaporated	Evaporated	ALE (Cl)	ALE (DEZ)
	Short-term	Long-term		
C-V (+)	p-shift	n-shift	n-shift(soft)	p-shift(rigid)
C-V (-)	p-shift	n-shift (soft)	n-shift(rigid)	p-shift(soft)
VIQ polarity	-	+	- (2 peaks)	+
Aging region	bottom (ITO)	top (Al)	bottom (ITO)	top (Al)
Trap depth (eV)	1.1	1.1	0.3 + deeper	0.8
σ (cm^2)	10^{-14}	10^{-14}	Unknown	10^{-15}
Density (cm^{-3})	10^{16}	10^{16}	10^{17}	10^{17}

ALE ACTFEL devices investigated occurs at a single interface. The density of traps shown in Table 5 is a rough estimate due to the RC time constant of the system, as well as the uncertainty of the thickness of the "trapping layer". It is assumed that all traps lie within 100 nm of the interface, but this estimate may be off by an order of magnitude.

The physical nature of the traps responsible for VIQ aging is now explored. Traps may be either intrinsic or extrinsic. The three possible kinds of intrinsic defects in a binary compound such as ZnS are i) vacancies, ii) interstitials, iii) antisites. The extremely large energy of formation of self-interstitials and antisites suggests that only vacancies are likely to exist in the ZnS crystal. [30] A zinc vacancy is a double acceptor. The first and second ionization energies of a zinc vacancy in ZnS have been crudely estimated as ~0.5 and ~1.5 eV, with respect to the valence band maximum. [1] A sulfur vacancy is a double donor. The first and second ionization energies of a sulfur vacancy in ZnS have been estimated as ~1.2 and ~1.4 eV. [2] The estimated energy depth and defect charge states of these intrinsic and several extrinsic defects are shown in Fig. 4.24.

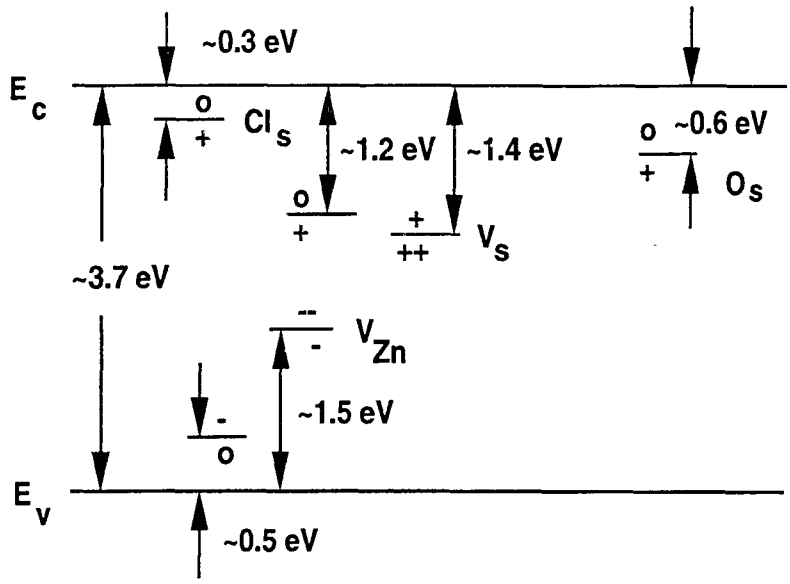

Figure 4.24. Estimated energy depths of possible traps responsible for the VIQ signal. Ionization energies of Zn vacancies [1], ionization energies of sulfur vacancies [2], ionization energy of chlorine [3, 4, 5], ionization energy of oxygen [3].

Table 6. Ionic radii of Zn, S and possible extrinsic defect candidates giving rise to the VIQ signal. All ionic radii are from Shannon [6], with the exception of C^{-4} which is from Lange [7].

Ion	ionic radii (pm)
Zn^{+2}	74
S^{-2}	170
O^{-2}	124
C^{+4}	29
C^{-4}	260
H^{+1}	10^{-5}
OH^{-1}	121
Cl^{-1}	167

Possible extrinsic defects are now considered. The energy depth of Cl in ZnS is ~0.2-0.3 eV. [3, 4, 5] Thus, it is very likely that the VIQ Peak 1 in the ALE (Cl) ZnS:Mn ACTFEL device is due to Cl. Other possible extrinsic defects are hydrogen, oxygen and carbon. The extremely small size of hydrogen (see Table 6) makes it highly unlikely that hydrogen would sit on a substitutional site in ZnS. However, hydrogen could be incorporated as a complex with other intrinsic or extrinsic defects, or may form an OH^{-1} group, which would act as a donor. The energy depth of oxygen in ZnS has been estimated as ~0.29-0.85 eV. [3, 31, 32] Although oxygen is not a carrier gas for either of the ALE processes investigated, a significant amount of oxygen (residual from deposition of ATO, or as a result of an impure purge gas) may still be present in the reactor. The size mismatch and valence of carbon sitting on a zinc or a sulfur site is so large that substitution is not likely (see Table 6).

Oxygen on a sulfur site is an isoelectronic trap [33]. Oxygen and sulfur are in the same column of the periodic table. Thus, oxygen and sulfur have the same number of valence electrons. However, since the electronegativity of oxygen (3.5) is larger than sulfur (2.5), the resultant O_s trap will be an acceptor-like site. [33] If an OH^{-1} group sits on a sulfur site it will create a donor-like trap. Information about the energy depth of OH^{-1} is not available, but the ionic radius and the single donor nature of the OH^{-1} group makes it a possible candidate as a deep donor in ZnS. Further work is required to ascertain whether OH^{-1} is a viable candidate.

The capture cross-section of a trap yields insight into the charge state of the trap. Traps with a capture cross-section greater than $\sim 10^{-14}$ are attractive, traps with a capture cross-section of $\sim 10^{-14}$-10^{-18} are neutral, and traps with a capture cross-section less than $\sim 10^{-18}$ are coulombically repulsive. [25]

The capture cross-section of the trap responsible for VIQ is important in the determination of the physical nature of the trap. The capture cross-sections determined from the temperature-dependent VIQ method are estimates whose accuracy is approximately an order of magnitude. Both of the trap capture cross-sections lie on the border between coulombically neutral and attractive. The 10^{-14} cm^2 estimated capture cross-section of the 1.1 eV trap for the evaporated ZnS:Mn ACTFEL device

suggests that the trap is slightly coulombically attractive; the first ionization state of a sulfur vacancy is a likely candidate. The 10^{-15} cm^2 estimated capture cross-section of the 0.8 eV trap for the ALE (DEZ) ZnS:Mn ACTFEL device suggests that the trap responsible for VIQ aging is coulombically neutral, which is consistent with oxygen sitting on a sulfur site as an isoelectronic trap.

The capture cross-sections for Peak 1 and Peak 2 of the ALE (Cl) ZnS:Mn ACTFEL devices could not be determined, which makes identication of these traps more difficult. However, the ~0.3 eV energy depth of Peak 1 suggests Cl_s as a strong possibility. Tentatively, Peak 2 is ascribed to oxygen sitting on a sulfur site as an isovalent trap since the VIQ Peak 2 trends shown in Fig. 4.16 are somewhat similar to the VIQ trends for the ALE (DEZ) ACTFEL device shown in Fig. 4.20. However, Peak 2 could also be attributed to the first ionization energy of a sulfur vacancy. The PDP method performed by Vlasenko et al. reaches similar conclusions regarding the physical nature of the traps responsible for aging in ALE ZnS:Mn ACTFEL devices. Specifically, Vlasenko et al. identify a trap at an energy depth of ~0.3 eV attributed to Cl, and a trap at an energy depth of ~0.9-1.2 eV attributed to O. [16]

In summary, possible atomic identifications of VIQ traps responsible for aging are as follows:

(i) Evaporated ZnS:Mn $\rightarrow$ 1.1 eV, 10^{-14} cm^2 $\rightarrow$ $V_s^{0/+}$

(ii) ALE (Cl) ZnS:Mn $\rightarrow$ 0.3 eV (Peak 1) $\rightarrow$ $Cl_s^{0/+}$

ALE (Cl) ZnS:Mn $\rightarrow$ (Peak 2) $\rightarrow$ $O_s^{-/0}$ (or $V_s^{0/+}$)

(iii) ALE (DEZ) ZnS:Mn $\rightarrow$ 0.8 eV, 10^{-15} cm^2 $\rightarrow$ $O_s^{-/0}$

Chapter 5
Conclusions and Recommendations for Future Work

Two optical excitation experiments are presented in this thesis. The first, photo-induced charge/photo-induced luminescence (PIQ/PIL), gives evidence of hole trapping in evaporated ZnS:Mn ACTFEL devices as well as allows for detemination of a threshold field for impact excitation of Mn luminescent centers. The second experiment, sub-threshold voltage induced charge (VIQ), yields trap depths and capture cross-sections for traps within the ZnS:Mn crystal as well as supportive evidence related to which interface(s) gives rise to the aging behavior of evaporated, ALE (Cl), and ALE (DEZ) ZnS:Mn ACTFEL devices.

5.1 Conclusions PIQ/PIL Experiments

PIL measurements of evaporated ZnS:Mn ACTFEL devices show a PIL threshold of $\sim$1 MV/cm. This threshold field is independent of the thickness of the phosphor. This leads to the conclusion that the threshold field necessary for impact excitation of Mn luminescent centers is $\sim$1 MV/cm.

PIQ measurements of evaporated ZnS:Mn ACTFEL devices show evidence for hole trapping in the phosphor layer. Hole trapping is characterized by a drift length of $\sim 180 \pm 70$ nm, a hole lifetime of $\sim$2 ps, and a trap capture cross-section of $\sim 7 \times 10^{-13}$ cm^2. It is speculated that this hole trap is most likely a zinc vacancy or a zinc vacancy complex.

5.2 Conclusions of VIQ Experiments

VIQ measurements yield estimates of the energy depth, capture cross-section, and density of traps in the evaporated, ALE (Cl), and ALE (DEZ) ZnS:Mn ACTFEL devices investigated. VIQ results in conjunction with C-V measurements provide a

consistent picture of the physical nature of ACTFEL device aging. It appears that aging occurs due to changes in the density of traps at or near the phosphor/insulator interfaces. Initial aging of evaporated ZnS:Mn ACTFEL devices occurs at the bottom (ITO) interface; long-term aging occurs at the top (Al) interface. Aging of ALE (Cl) ZnS:Mn ACTFEL devices occurs at the bottom (ITO) interface. Aging of ALE (DEZ) ZnS:Mn ACTFEL devices occurs at the top (Al) interface.

The energy depth of the trap responsible for VIQ in evaporated ZnS:Mn ACTFEL devices is $\sim$1.1 eV with a capture cross-section of $\sim 10^{-14}$ cm^2. The energy depth of the trap responsible for VIQ in ALE (Cl) ZnS:Mn ACTFEL devices is $\sim$0.3 eV with a capture cross-section of $\sim 10^{-15}$ cm^2. A second VIQ peak for ALE (Cl) ZnS:Mn ACTFEL devices is attributed to the same trap as that found in ALE (DEZ) ZnS:Mn ACTFEL devices. The energy depth of the trap responsible for VIQ in ALE (DEZ) is $\sim$0.8 eV with a capture cross-section of $\sim 10^{-15}$. Assuming that all traps lie within 100 nm of the interface, the trap density is estimated to be $\sim 10^{16}$ cm^{-3} for evaporated ZnS:Mn ACTFEL devices and $\sim 10^{17}$ cm^{-3} for ALE (Cl) and ALE (DEZ) ZnS:Mn ACTFEL devices.

Atomic identifications possibilities for VIQ traps in ZnS:Mn ACTFEL devices are as follows. The trap responsible for the VIQ signal in evaporated ZnS:Mn ACTFEL devices is attributed to a sulfur vacancy. The trap responsible for the VIQ signal in ALE (DEZ) ZnS:Mn ACTFEL devices is attributed to oxygen on a sulfur site. Peak 1 in the ALE (Cl) ZnS:Mn ACTFEL devices is attributed to chlorine and Peak 2 is attributed to oxygen on a sulfur site (or possibly a sulfur vacancy). The physical nature of these traps is in agreement with the results of PDP experiments performed by Vlasenko et al. [16]

5.3 Recommendations for Future Work

PIQ/PIL experiments should be performed on different materials. A thickness-dependent study of ALE (Cl) and ALE (DEZ) ZnS:Mn ACTFEL devices would facilitate the determination of whether PIQ/PIL trends in evaporated ZnS:Mn ACTFEL

devices is due to the ZnS:Mn lattice itself, or is due to the deposition method. If PIQ/PIL trends for the above mentioned ACTFEL devices are identical to evaporated PIQ/PIL trends, it would strengthen to the conclusions made about evaporated ZnS:Mn ACTFEL devices.

PIQ/PIL experiments should also be performed using ALE and sputtered SrS:Ce and ALE SrS:Cu in order to investigate the properties of these materials compared to ZnS:Mn.

The VIQ method may be expanded by performing VIQ with a few modifications. VIQ should be performed using ACTFEL devices with different phosphor thicknesses to determine whether trapped charge exists in the bulk of the phosphor, or is mostly in the region near the interfaces. Performing VIQ with single wavelength excitation may yield information about the energy depth of traps responsible for VIQ. Performing VIQ with a single voltage pulse followed by an optical reset would facilitate determination of the amount of space charge present in the PIQ/PIL experiment. The transient of the VIQ signal should be investigated to ascertain whether the tail of the VIQ response contains any useful information. It is observed that the time constants of the VIQ transient change with temperature and aging, as well as for different phosphor types (SrS:Ce, ZnS:Mn). It may be that a detrapping time constant can be determined from an investigation of the VIQ transient.

In order to more clearly establish the nature of the trap responsible for VIQ in the ALE samples investigated, oxygen-rich samples should be fabricated. By performing VIQ on samples which are identical other than oxygen concentration, the nature of Peak 2 in the ALE (Cl) and the peak in the ALE (DEZ) ZnS:Mn ACTFEL devices tested can be more accurately determined. If the VIQ peaks do not change in magnitude with intentional oxygen doping, then these peaks are most likely due to sulfur vacancies.

BIBLIOGRAPHY

[1] F. A. Kroger, *The Chemistry of Imperfect Crystals.* Amsterdam:North Holland, 1974.

[2] S. H. Sohn and Y. Hamakawa *Jp. J. Appl. Phys.*, vol. 31, p. 3901, Apr. 1992.

[3] W. Hoogstraten *Philips Res. Repts.*, vol. 13, p. 515, 1958.

[4] C. S. Kang, P. B. P. Phipps, and R. H. Bube *Phys. Rev.*, vol. 156, p. 998, 1967.

[5] H. Arbell and A. Halperin *Phys. Rev.*, vol. 117, p. 45, 1960.

[6] R. D. Shannon, "Revised effective ionic radii and systematic studies of interatomic distances in halides and chalcogenides," *Acta Crystallogr.*, vol. A32, pp. 751–67, 1976.

[7] N. A. Lange, *Lange's Handbook of Chemistry.* McGraw-Hill, Inc., 1978.

[8] J. B. Peery, "State space charge modeling of alternating-current thin-film electroluminescent devices," Master's thesis, Oregon State University, 1997.

[9] D. Corlatan, K. Neyts, P. D. Visschere, and J. V. den Bossche, "UV induced activator excitation in ZnS:Mn thin film electroluminescent devices with probe layers," in *Proceedings of 1994 International Workshop on Electroluminescence*, p. 211, Science Press, Beijing, 1994.

[10] D. Corlatan, K. A. Neyts, and P. D. Visschere, "The influence of space charge and electric field on the excitation efficiency in thin film electroluminescent devices," *J. Appl. Phys.*, vol. 78, pp. 7259 – 64, Dec. 1996.

[11] U. Troppenz, B. Huttl, K. O. Velthaus, and R. H. Mauch, "Carrier sourcing in SrS:Ce, Cl thin film EL-devices," in *Proceedings of 1994 International Workshop on Electroluminescence* (X. Xu, ed.), p. 162, Science Press, Beijing, Dec. 1994.

[12] U. Troppenz, B. Huttl, K. O. Velthaus, and R. H. Mauch, "Trailing egde phenomena in SrS:Ce, Cl thin film electrolumnescent devices," *Journal of Crystal Growth*, vol. 138, pp. 1017 – 22, Dec. 1994.

[13] B. Huttl, U. Troppenz, K. O. Velthaus, C. R. Rhonda, and R. H. Mauch, "Luminescence properties of SrS:Ce 3+," *J. Appl. Phys.*, vol. 78, no. 12, pp. 7282 – 8, 1996.

[14] B. Huttl, P. Kratzert, K. Lite, B. Reinsperger, T. K. Plant, and R. H. Mauch, "Study of carrier transport in SrS:Ce, Mn, Cl electroluminescent devices by optical method," *Inorganic and Organic Electroluminescence*, p. 73, 1996.

[15] U. Troppenz, T. K. Plant, B. Huttl, K. O. Velthaus, and R. H. Mauch, "Electrical properties of SrS:Ce EL devices," in *Proceedings of 1996 International Workshop on Electroluminescence*, no. 293 in 1, p. 293, Dec. 1996.

[16] N. A. Vlasenko, A. I. Beltskii, Z. L. Denisova, Y. F. Kononets, and L. I. Veligura, "On causes of instability in beginning of aging of evaporated ZnS:Mn ACTFEL devices," *Inorganic and Organic Electroluminescence*, pp. 267 – 270, 1996.

[17] Y. F. Kononets, R. Tornqvist, and N. A. Vlasenko, "On physical model of aging behaviour of atomic layer epitaxy ZnS:Mn AC TFEL devices," *Inorganic and Organic Electroluminescence*, pp. 259 – 262, 1996.

[18] J. V. den Bossche, B. Soenen, K. Neyts, P. D. Visschere, and D. Corlatan, "Aging of evaporated and ALE AC thin-film electroluminescent devices," in *Proceedings of 8th International Workshop on Inorganic and Organic Electroluminescence*, Aug. 1996.

[19] B. Soenen, J. Ihanus, G. Stuyven, P. D. Visschere, M. Ritala, and M. Leskela, "Aging of electroluminescent devices based on ZnS deposited with atomic layer epitaxy from various precursors," in *Third International Conference on the Science and Technology of Display Phosphors*, Nov. 1997.

[20] A. Abu-Dayah and J. F. Wager, "Aging of atomic layer epitaxy ZnS:Mn alternating-current thin-film electroluminescent devices," *J. Appl. Phys.*, vol. 75, pp. 3593 – 3598, Apr. 1994.

[21] J. D. Davidson, J. F. Wager, and S. Kobayashi, "Aging studies of evaporated ZnS:Mn alternating-current thin-film electroluminescent devices," *J. Appl. Phys.*, vol. 71, pp. 4040 – 4047, Apr. 1992.

[22] J. C. Hitt, P. D. Keir, J. F. Wager, and S. S. Sun, "Static space charge in evaporated ZnS:Mn alternating-current thin-film electroluminescent devices," *J. Appl. Phys.*, vol. 83, p. 1141, Jan. 1998.

[23] I. Lee, S. Pennathur, K. Streicher, T. K. Plant, J. F. Wager, P. Vogl, and S. M. Goodnick, "High-field electron transport of the ZnS phosphor in AC thin-film electroluminescent devices," *Inst. Phys. Conf. Ser. No.*, p. 1229, Dec. 1996.

[24] K. Ohmi, K. Ishitani, Y. Kashio, Y. Fujimoto, S. Tanaka, and H. Kobayashi, "Dynamic space charge in SrS:Ce thin-film electroluminescent devices studied by polarization charge erasing pulse technique," in *Second International Conference on the Science and Technology of Display Phosphors*, Nov. 1996.

[25] B. Balland and G. Barbottin, "Trapping and detrapping kinetics impact on C(V) and I(V) curves," *Instabilities in Silicon Devices*, pp. 7 – 81, 1989.

[26] P. D. Keir, "Modeling of space charge in alternating-current thin-film electroluminescent devices," Master's thesis, Oregon State University, 1995.

[27] A. Mikami, K. Terada, K. Okibayashi, K. Tanaka, M. Yoshida, and S. Nakajima, "Aging characteristics of ZnS:Mn electroluminescent films grown by a chemical vapor deposition technique," *J. Appl. Phys.*, vol. 72, pp. 773–782, July 1992.

[28] K. W. Yang, S. J. T. Owen, and D. H. Smith, "Studies of temperature effects in AC thin-film el devices," *Electro-optics*, vol. 28, pp. 703–708, 1981.

[29] J. F. Wager, "A comparison of ZnS:Mn ACTFEL devices prepared by evaporation and atomic layer epitaxy," in *Proceedings of the 1994 International Workshop on Electroluminescence* (B. Xurong Xu (Science Press, ed.), p. 49, 1994.

[30] J. F. Wager, "Electroluminescent phosphors: Point defects," *Inorganic and Organic Electroluminescence*, pp. 33–38, 1996.

[31] A. L. Gurskii, E. V. Lutsenko, N. K. Morozova, and G. P. Yablonskii, "Impurity luminescence of ZnS:O single crystals at high levels of optical and streamer excitation," *Soviet Physics - Solid State*, vol. 34, pp. 1890–3, Nov. 1992.

[32] J. S. Kang, S. H. Park, S. G. Lee, and S. H. Sohn, "Electrooptical properties of II-VI semiconducting thin-films doped with isoelectronic impurities," *Journal of the Korean Physical Society*, vol. 30, no. 3, pp. 600–607, 1997.

[33] K. Akimoto, H. Okuyama, M. Ikeda, and Y. Mori, "Aging characteristics of ZnS:Mn electroluminescent films grown by a chemical vapor deposition technique," *J. Appl. Phys.*, vol. 72, pp. 773–782, July 1992.

[34] S. M. Sze, *Physics of Semiconductor Devices.* Wiley Interscience, 1981.

APPENDICES

Appendix A.1
Number of Subthreshold Pulses to Steady-State Operation

The VIQ effect was first observed while attempting to duplicate PIQ/PIL experiments of Neyts et al., in which a xenon lamp is used to reset the phosphor to a flat-band condition between each electrical pulse. [10] The duration of the light pulse needed to fully reset the phosphor was uncertain, so experiments were performed to determine the necessary reset time. To accomplish this, the ACTFEL device was driven electrically above threshold for a few seconds and then turned off. Subsequently, a xenon lamp was turned on and a transient change of the charge on the sense capacitor was observed during these experiments to determine the required reset time duration. While monitoring the xenon lamp-induced sense capacitor charge transient, it was noted that a charge transient was observed even when a subthreshold voltage pulse sequence was employed. These observations led to the development of the VIQ measurement technique.

In their discussion of PIQ/PIL measurements, Neyts et al. mention that for optical resetting, the ACTFEL device must be grounded during the application of the light pulse in order for the charge released to have a means of dissipating. [10] It is not clear how this is accomplished in Neyts et al. experimental apparatus, but in the experiments performed for this thesis the ACTFEL device is kept connected to the measuring system while the xenon lamp pulse is applied. Maintaining electrical connection of the ACTFEL device to the measurement system ensures that the optically-induced charge is drained through the 1 MΩ impedence of the oscilloscope. The importance of maintaining the electrical connection of the ACTFEL device and the measurement system was recognized later in the research project when an alternative implementation of the VIQ experiment was attempted using a buffer amplifier between the sense capacitor and the oscilloscope, as presented in Appendix A.5.

Thus, if the VIQ signal is to be measured, the ACTFEL device must remain electrically connected to the measuring apparatus during the optical reset. It is

possible that VIQ was not previously observed by Neyts et al., particularly if they removed the ACTFEL device from the measurement apparatus in order to ground it during the optical reset. If the device was disconnected and manually shorted, measurements could not be obtained during application of the light pulse and, thus, VIQ would not be observed.

While performing experiments to determine the length of the optical reset pulse needed for the PIQ/PIL experiment, it was observed that the magnitude of the DC offset induced on the sense capacitor immediately following the optical reset pulse changed as a function of the maximum applied voltage of the bipolar pulse sequence. The number of subthreshold bipolar electical pulses needed to achieve steady-state operation is uncertain. The length of time required to reach steady-state could possibly be due to the time constant of the system; however, the following experiment seems to refute this. The ACTFEL device is optically reset and then bursts of 500 standard bipolar electrical pulses are applied. The first electrical burst of 500 pulses produces a large DC offset on the sense capacitor, which is allowed to decay to zero. The next burst of 500 pulses produces a smaller DC offset, and so on. It is found that the ACTFEL device does not reach steady-state (i.e. no DC offset is induced on the sense capacitor) until about 10 bursts of 500 pulses are applied. It is hypothesized that if 500 pulses is sufficient to ionize all of the traps, and create all of the space charge in the ACTFEL device, then the second burst should have no effect; the ACTFEL device would already be at steady-state. This leads to the conclusion that below threshold, many thousands of pulses are required to reach steady-state, as opposed to only a few when the ACTFEL device is driven above threshold.

VIQ experiments are performed using 20,000 (20 s) bipolar voltage pulses and a 20 second optical reset. Experiments were also performed using a 45 second optical reset and 30,000 (30 s) bipolar voltage pulses to be certain that the ACTFEL device reached steady-state. The results of both experiments were identical, leading to the use of 20,000 electrical pulses followed by a 20 second optical reset for all measurements discussed herein.

Appendix A.2
Time response of VIQ

The 1 MΩ input impedence of the oscilloscope and the 100 nF capacitance of the sense capacitor yield a time constant of 100 ms for the VIQ measurement system. Thus, the VIQ peak is only an estimate of the actual charge transferred during the optical pulse since the VIQ transient is established by both optically-induced charge rearrangement and by RC discharge through the oscilloscope.

As with any RC system, the response to a unit step of voltage is an increase in the voltage across the sense capacitor which saturates once V = Q/C. When the voltage is removed, the voltage across the sense capacitor decays to zero at a rate determined by the time response of the system. In the case of VIQ measurements, the time response curve suggests that VIQ is due to a relatively constant current from the device upon application of the light pulse, i.e. a step input to the RC measurement system. However, the constant current step is not long enough for the voltage across the the sense capacitor to saturate. Therefore, the VIQ maximum voltage which is measured is less than the actual maximum voltage that would be sensed if the time response of the system were faster. Because of this, all VIQ curves consititute a lower estimate of the actual xenon lamp-induced transferred charge.

Appendix A.3
Spectral Response of VIQ

It should be noted that the xenon lamp is incident on the phosphor through the glass substrate as well as the ITO layer. Thus, much of the incident UV light from the xenon lamp is absorbed by the glass. In order to determine which wavelengths of light are responsible for the VIQ effect, the VIQ experiment is performed by passing the incident light through a monochromator. The wavelength of excitation is scanned from 250 to 400 nm. For below-bandgap photon energies less than ~3.35 eV (~370 nm), no VIQ effect is detectable. Also, for above bandgap photon energies greater than ~4 eV (~310 nm), no VIQ effect is observed. The VIQ effect peaks at ~3.8 eV (~325 nm). In semiconductor and dielectric materials, light is exponentially absorbed as a function of distance into the material.

$$I(d) = I_o e^{-\alpha d} \tag{5.1}$$

where I_o is the incident intensity, d is the distance into the semiconductor, and α is the absorption coefficient, which is dependent on the material and the wavelength of the incident intensity.

Since α increases rapidly for increasing photon energies near that of the bandgap, this relation shows that absorption within the phosphor is more uniform for longer wavelengths, while for shorter wavelengths the light is absorbed closer to the incident interface. The absorption coefficient for ZnS:Mn at 325 nm is ~10^5 cm^{-1}. [34] Thus, the fact that the VIQ signal peaks near the bandgap energy of ~3.8 eV leads to the conclusion that the VIQ signal monitored during the optical reset is associated with electron-hole pairs generated near the incident phosphor/insulator interface. If the VIQ signal peaked at lower energies, this would be evidence that the VIQ signal is due to electron-hole pairs generated uniformly across the phosphor.

Finally, when the VIQ experiment is performed with single wavelength excitation of ~3.8 eV, the experimental trends are identical to those obtained using broadband radiation. Therefore, broadband radiation is used for all future experiments as a larger signal-to-noise ratio is achieved with the higher intensity broadband light.

Appendix A.4
VIQ Illuminated from the Opposite Interface

In an attempt to test the hypothesis that VIQ is due to electron-hole pair generation near the incident interface, rather than in the bulk of the phosphor, the ACTFEL device is illuminated from the opposite side, hereafter referred to as the aluminum side.

On the aluminum side of the sample, aluminum dots used to electrically contact the ACTFEL device cover the active area, so the light must be incident at an angle. When illuminated from the aluminum side, the VIQ signal is the same polarity as when illuminated from the ITO side. In addition, the spectral response of the VIQ signal is identical when illuminated from the aluminum side, with radiation outside of ~3.35-4 eV having no effect, and a peak response found at ~3.8 eV. Illumination from the aluminum side also shows that the VIQ spectral response is a real experimental trend, rather than an artifact due to attenuation of UV light in the glass substrate.

To be certain that the VIQ signal is the same when illuminated from either side, the construction of samples with ITO contacts on both sides is needed. Use of an ITO instead of an aluminum top contact would allow the xenon lamp to be normally incident onto the phosphor. Use of these samples would facilitate optical excitation from both sides of the phosphor much better than the current method of exciting the phosphor at an angle when illuminating from the aluminum side.

Appendix A.5
VIQ Measurements using a Buffer Amplifier

It is observed that when the ACTFEL device is first driven electrically with bipolar pulses following the application of an optical reset, the charge on the sense capacitor experiences a DC shift for a few seconds before returning to zero, as shown in Fig. A.1. This occurs well below threshold, and is thought to be linked to the ionization of traps within the phosphor giving rise to space charge in the ACTFEL device. When the ACTFEL device is turned off and on again without the optical reset, the charge on the sense capacitor does not experience a DC shift.

Standard VIQ is acquired by measuring the maximum charge on the sense capacitor following the application of the optical pulse. In this section, VIQ data is acquired by optically resetting the ACTFEL device and then measuring the peak charge induced on the sense capacitor immediately following the application of the bipolar electrical pulses. In this case, the peak due to the electrical pulses is measured, as opposed to the peak due to the optical pulse, the latter being the standard VIQ method. The VIQ trends when measuring the peak charge on the sense capacitor following application of the electrical pulses are identical to the results obtained by the standard VIQ method, but are opposite in polarity. This observation lends support to the belief that charge is redistributed during the electrical phase of the experiment, and then reset by the optical pulse.

The input impedence of the oscilloscope has a strong effect on the VIQ response since charge is dissipated from the sense capacitor through this load. Therefore, a buffer amplifier is implemented for the acquisition of VIQ. The buffer amplifier has a very high input impedence and is placed between the oscilloscope probe and the sense capacitor. Thus, the sense capacitor has no means of discharging. VIQ measurements with the buffer amplifier are performed using the method shown in Fig. A.1, i.e. application of an optical reset followed by measurement of the maximum voltage induced on the sense capacitor following application of electrical pulses. With the buffer amplifier in place, the voltage on the sense capacitor is zero during the

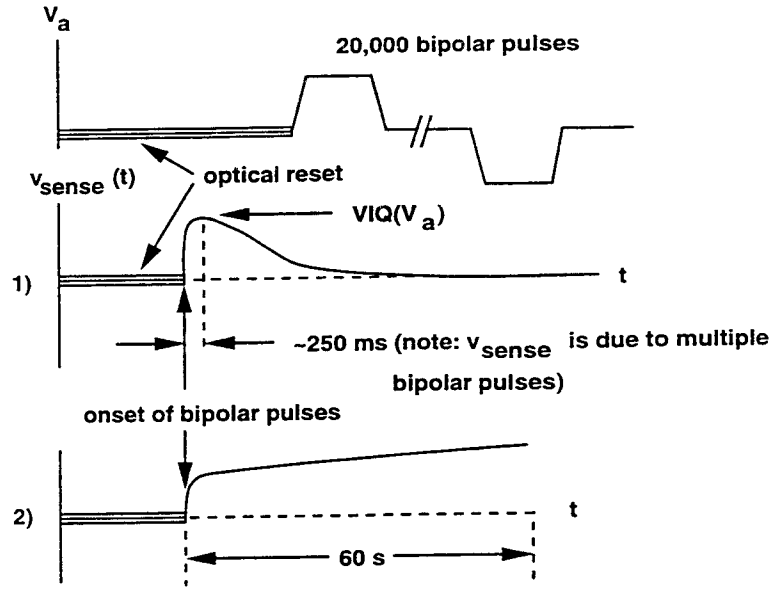

Figure A.1. VIQ acquired by measuring the maximum voltage induced on the sense capacitor immediately following application of bipolar electrical pulses. The v_{sense} curve 1 is the response of the system in the absence of a buffer amplifier. The v_{sense} curve 2 is the response of the system with a buffer amplifier.

optical reset, and then jumps to some value when the electrical pulses are applied, presumably due to the ionization of traps within the phosphor. It is hypothesized that the voltage on the sense capacitor following application of the electrical pulses should saturate at some maximum value.

Once all of the traps are ionized, the signal should reach a steady-state and application of subsequent pulses should have no effect. However, this is not observed. The voltage on the sense capacitor jumps to some value, but then continues to slowly increase and never saturates. As many as 60,000 bipolar pulses are applied, but saturation is still not observed, as shown in Fig. A.1 curve 2.

It is unclear why the non-saturating behavior of the VIQ trend occurs when measurements are performed with the buffer amplifier. It is possible that the amplifier voltage is slightly larger for one polarity, resulting in continued build up of charge on one interface. It is also possible that the initial jump is due to ionization of electron traps, and the slow non-saturating portion is due to ionization of hole traps or perhaps deeper electron traps. Thus, the non-saturating nature of the VIQ

signal when a buffer amplifier is employed is not understood and makes it difficult to interpret VIQ data.

Another problem with the use of the buffer amplifier is that when the ACTFEL device experiences 'burn-outs', i.e. shorting of small regions of the ACTFEL device, the charge on the sense capacitor becomes very large and has no means of dissipating, making aquisition of data impossible until the voltage on the ACTFEL device is returned to zero by manually shorting the sense capacitor. During standard VIQ operation in the absence of the buffer amplifier, 'burn-outs' cause the voltage on the sense capacitor to jump, but the charge is dissipated within a few seconds through the input impedence of the oscilloscope, so this is not a problem during normal (i.e. no buffer amplifier) VIQ operation.

Use of the buffer amplifier and measurement of the electrical maximum when acquiring VIQ data does not appear to be the best method for performing VIQ. Although use of the buffer amplifier seems like a clear and elegant method for accomplishing VIQ measurements, the non-saturating behavior of the VIQ signal, coupled with the 'burn-out' problem stated above, makes it very difficult to obtain meaningful VIQ data with the buffer amplifier at this time.